

19970425 048

Naval Research Laboratory

Stennis Space Center, MS 39529-5004



NRL/MR/7243--97-8040

Three-Dimensional Optical Fields Derived from Aircraft Remote Sensing Imagery: Results from the Hamlet's Cove Experiment, Eglin AFB, FL, August 1994

RICHARD W. GOULD, JR.
ROBERT A. ARNONE

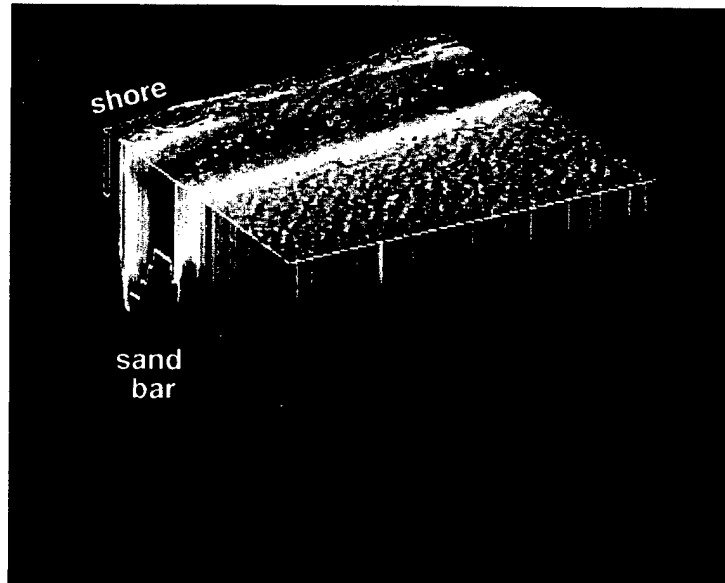
*Remote Sensing Applications Branch
Remote Sensing Division*

PAUL M. MARTINOLICH

*Neptune Sciences, Inc.
Slidell, LA*

TODD E. BOWERS

*Planning Systems Incorporated
Slidell, LA*



March 21, 1997

DTIC QUALITY

Approved for public release; distribution unlimited.

REPORT DOCUMENTATION PAGE

Form Approved
OMB No. 0704-0188

Public reporting burden for this collection of information is estimated to average 1 hour per response, including the time for reviewing instructions, searching existing data sources, gathering and maintaining the data needed, and completing and reviewing the collection of information. Send comments regarding this burden or any other aspect of this collection of information, including suggestions for reducing this burden, to Washington Headquarters Services, Directorate for Information Operations and Reports, 1215 Jefferson Davis Highway, Suite 1204, Arlington, VA 22202-4302, and to the Office of Management and Budget, Paperwork Reduction Project (0704-0188), Washington, DC 20503.

1. AGENCY USE ONLY (Leave blank)	2. REPORT DATE	3. REPORT TYPE AND DATES COVERED	
	March 21, 1997	Final	
4. TITLE AND SUBTITLE			5. FUNDING NUMBERS
Three-Dimensional Optical Fields Derived from Aircraft Remote Sensing Imagery: Results from the Hamlet's Cove Experiment, Eglin AFB, FL, August 1994			Job Order No. 572-5939-A7 Program Element No. 0601153N Project No. Task No. BE031 03 4G Accession No.
6. AUTHOR(S)			
Richard W. Gould, Jr., Robert A. Arnone, Paul M. Martinolich*, and Todd E. Bowers†			
7. PERFORMING ORGANIZATION NAME(S) AND ADDRESS(ES)			8. PERFORMING ORGANIZATION REPORT NUMBER
Naval Research Laboratory Remote Sensing Division Stennis Space Center, MS 39529-5004			NRL/MR/7243--97-8040
9. SPONSORING/MONITORING AGENCY NAME(S) AND ADDRESS(ES)			10. SPONSORING/MONITORING AGENCY REPORT NUMBER
Office of Naval Research 800 North Quincy Street Arlington, VA 22217-5000			
11. SUPPLEMENTARY NOTES			
<p>*Neptune Sciences, Inc., 150 Cleveland Ave., Slidell, LA 70458 †Planning Systems Incorporated, 115 Christian Lane, Slidell, LA 70458</p>			
12a. DISTRIBUTION/AVAILABILITY STATEMENT		12b. DISTRIBUTION CODE	
Approved for public release; distribution unlimited.			
13. ABSTRACT (Maximum 200 words)			
<p>Three-dimensional distributions of inherent optical properties (absorption, a, scattering, b, and single-scattering albedo, ω_0) at six SeaWiFS wavelengths were defined for a coastal region by coupling surface ocean color imagery and models of vertical optical profiles. Aircraft measurements of water-leaving radiance collected over a nearshore environment in the northeastern Gulf of Mexico were incorporated into a modified SeaWiFS algorithm after atmospheric correction and removal of the bottom reflectance component, to provide surface estimates of a, b, and ω_0.</p> <p>To estimate subsurface distribution patterns, <i>a priori</i> knowledge of the depth distributions of the optical properties is required at several locations in the image. During the aircraft overflights, concurrent in situ depth profiles of absorption and scattering were collected at five stations along an offshore transect. The depth profiles for each station and wavelength were modeled using a sigmoidal or a bimodal Gaussian distribution. The individual modeled depth profile shapes were subsequently applied across the image by assigning the curve shapes to pixels with expected similar hydrographic properties. In this shallow coastal environment, the distribution patterns appeared related to coastal run-off and river discharge (and therefore bathymetry, indirectly), so profile shapes were assigned to pixels based on the water depth at each location. Thus, all pixels that fell within specified depth ranges were initially assigned the same profile shape.</p> <p>The modeled profiles of the optical properties were integrated over depth (weighted by the diffuse attenuation coefficient calculated from the corresponding a and b values) to provide a "remote-sensing" estimate comparable to what the aircraft sensor would see. At each pixel in the image, the initial optical depth profiles were iteratively adjusted by "sliding" the profile up or down the x axis to increase or decrease the integrated values until they agreed to within $\pm 5\%$ of the surface aircraft estimates. The depth</p>			
14. SUBJECT TERMS			15. NUMBER OF PAGES
remote sensing, optical properties, three-dimensional modeling			72
			16. PRICE CODE
17. SECURITY CLASSIFICATION OF REPORT	18. SECURITY CLASSIFICATION OF THIS PAGE	19. SECURITY CLASSIFICATION OF ABSTRACT	20. LIMITATION OF ABSTRACT
Unclassified	Unclassified	Unclassified	SAR

and magnitude of the gradient were adjusted slightly as well to smoothly transition between profile shapes. When convergence was obtained, the depth distributions were defined from the corresponding profile.

Cool, low-salinity water with high absorption and scattering values was uniformly mixed over the sand bar and shoreward and extended offshore in a narrowing lens. The sharp thermo/halocline shoaled to a depth of 1–2 meters at a distance of about 400 meters offshore. Scattering and absorption coefficients were reduced by factors of three and two, respectively, in the warm, saline subsurface layer, relative to the surface layer.

Three-Dimensional Optical Fields Derived from Aircraft Remote Sensing Imagery:
Results from the Hamlet's Cove Experiment, Eglin AFB, Florida, August 1994

Richard W. Gould, Jr. and R.A. Arnone
Naval Research Laboratory, Code 7243
Stennis Space Center, MS 39529

Paul M. Martinolich
Neptune Sciences, 150 Cleveland Ave.
Slidell, LA 70458

Todd E. Bowers
Planning Systems, Inc., 115 Christian Lane
Slidell, LA 70458

ABSTRACT

Three-dimensional distributions of inherent optical properties (absorption, a , scattering, b , and single-scattering albedo, ω_0) at six SeaWiFS wavelengths were defined for a coastal region by coupling surface ocean color imagery and models of vertical optical profiles. Aircraft measurements of water-leaving radiance collected over a nearshore environment in the northeastern Gulf of Mexico were incorporated into a modified SeaWiFS algorithm after atmospheric correction and removal of the bottom reflectance component, to provide surface estimates of a , b , and ω_0 .

To estimate subsurface distribution patterns, *a priori* knowledge of the depth distributions of the optical properties is required at several locations in the image. During the aircraft overflights, concurrent *in situ* depth profiles of absorption and scattering were collected at five stations along an offshore transect. The depth profiles for each station and wavelength were modeled using a sigmoidal or a bimodal Gaussian distribution. The individual modeled depth profile shapes were subsequently applied across the image by assigning the curve shapes to pixels with expected similar hydrographic properties. In this shallow coastal environment, the distribution patterns appeared related to coastal run-off and river discharge (and therefore bathymetry, indirectly), so profile shapes were assigned to pixels based on the water depth at each location. Thus, all pixels that fell within specified depth ranges were initially assigned the same profile shape.

The modeled profiles of the optical properties were integrated over depth (weighted by the diffuse attenuation coefficient calculated from the corresponding a and b values) to provide a "remote-sensing" estimate comparable to what the aircraft sensor would see. At each pixel in the image, the initial optical depth profiles were iteratively adjusted by "sliding" the profile up or down the x axis to increase or decrease the integrated values until they agreed to within $\pm 5\%$ of the surface aircraft estimates. The depth and magnitude of the gradient were adjusted slightly as well to smoothly transition between profile shapes. When convergence was obtained, the depth distributions were defined from the corresponding profile.

Cool, low-salinity water with high absorption and scattering values was uniformly mixed over the sand bar and shoreward and extended offshore in a narrowing lens. The sharp thermo/halocline shoaled to a depth of 1-2 meters at a distance of about 400 meters offshore. Scattering and absorption coefficients were reduced by factors of three and two, respectively, in the warm, saline subsurface layer, relative to the surface layer.

INTRODUCTION

Satellite and aircraft imagery has been used routinely by oceanographers to synoptically map surface distributions of geophysical parameters such as sea surface temperature, pigment concentration, diffuse attenuation coefficient, current speed and direction, wave heights, winds, coastal plumes and fronts, internal waves, and upwelling characteristics. More recently, attempts to estimate inherent optical properties of the water have met with some success. Previously, we incorporated Compact Airborne Spectral Imager (CASI) measurements of water-leaving radiance into a modified SeaWiFS bio-optical algorithm (after atmospheric correction and removal of the bottom reflectance component) to provide surface estimates of a and b (Gould and Arnone, in press). Here, we extend that work in an attempt to push the aircraft-derived surface estimates to depth using modeled profiles to obtain three-dimensional data volumes of a , b , and ω_0 for a coastal area.

Over a one week period in August 1994, an experiment was conducted off Eglin Air Force Base near Fort Walton Beach, Florida (Figure 1), to assess the physical and optical regime of the nearshore area, with measurements extending out to a water depth of approximately 10 meters. In the study area, a narrow sand bar about 2 m below the surface is located approximately 100 m off the east/west oriented coastline. The region off Eglin Air Force Base, Ft. Walton Beach, FL, was selected as the test site for the Hamlet's Cove experiment because of the quiescent nature of the coastal regime and the highly reflective white sand bottom conducive to bottom reflectance measurements. Event driven processes introduce a dynamic variability over short time and space scales. In Figure 1, a Landsat TM image from 10 August, 1994, the experimental area is enclosed by a red box in the upper zoomed image.

Our objectives are to: 1) model sparse depth profile measurements to extend the point measurements to every pixel across an image, 2) calculate integrated "remote sensing" estimates of how a remote sensor would see the modeled optical depth profiles, 3) adjust the depth model parameters at each point in the image to force the integrated estimate to agree with the CASI estimate, and 4) compute 3-D data volumes of a , b , and ω_0 and describe the optical environment in a coastal region.

BACKGROUND

In previous work (Gould and Arnone, in press), high resolution aircraft remote sensing imagery and *in situ* optical data were coupled to characterize the spatial and temporal variability of the inherent optical properties in the near-surf zone at this study site. Upwelling radiance measurements at SeaWiFS wavelengths were collected over a uniform, highly reflective white sand bottom at a ground resolution of 2.5 meters using the CASI sensor (Compact Airborne

Spectral Imager). Following atmospheric correction, the total remote sensing reflectance signal was partitioned into bottom and water volume reflectance components, using measurements of bottom albedo, water depth, and the diffuse attenuation coefficient at the time of the overflight. The water components were entered in the SeaWiFS bio-optical model to derive spectral absorption and scattering coefficients. After applying minor algorithm and coefficient adjustments, model results compared favorably with *in situ* measurements.

The bio-optical model was subsequently applied to the aircraft imagery to describe the surface spatial distribution of absorption and scattering. Elevated absorption and particle scattering were observed over the sand bar and shoreward ($a555 = 0.19 \text{ m}^{-1}$, $b555 = 0.7 \text{ m}^{-1}$). The temporal variability of the inherent optical properties over a one week period was similar to the spatial variability along a 500 m offshore transect.

In this study we examine small-scale, depth-dependent, spatial variability of optical properties in a nearshore environment using airborne remote-sensing imagery. Because ocean color remote sensors receive and record visible light not from a surface but from a layer of varying thickness, we can not typically extract depth-dependent information from the data. The thickness of the layer is referred to as the penetration depth of the sensor and represents the depth above which 90% of the diffusely reflected irradiance originates (Gordon and McCluney, 1975). The penetration depth corresponds to one attenuation length (the inverse of the diffuse attenuation coefficient, $1/k$), varies by wavelength, and depends on the absorbing and scattering properties of the water. Thus, the sensor in effect records an integrated, "remote sensing" surface layer estimate because the reflectance is not from a surface *per se*, but from a layer, the thickness of which depends on the water clarity.

If the optical properties of the water column are not vertically homogeneous within the layer defined by the penetration depth, the remote sensing surface layer estimate actually represents a weighted integral of the depth distribution of the optical parameter (Gordon and Clark, 1980; Sathyendranath and Platt, 1989). The weighting factor reflects the exponential attenuation of light with depth, so that values near the surface are weighted more heavily than values at depth. The remote sensor effectively "integrates" the stratified distribution to yield an apparent surface concentration, a value equivalent to a uniform depth distribution. Thus the depth distribution of the parameter is not retrievable from the satellite/aircraft estimate, unless some prior knowledge of the depth profile is available, as we will demonstrate

If *in situ* measurements of the optical depth profiles are available from the time of the sensor overpass or are known from previous studies of an area, we can model the distributions and extract depth distribution information from the remote sensing imagery. Lewis et al. (1983), Platt et al. (1988), and Platt et al. (1991) applied a unimodal Gaussian distribution superimposed on a constant background to model chlorophyll biomass depth distributions. In this study, we employ a similar approach to model absorption and scattering depth profiles, but either a bimodal Gaussian or a sigmoidal model was required (depending on pixel location) to adequately represent the measured profiles.

Because depth profiles measurements were available at only a very limited number of locations (five stations), we needed a way to extend these point measurements to every pixel in the image. A blotch field approach coupled with an iterative adjustment technique was developed for this purpose. First, all pixels were classified into one of five blotch fields based on water

depth. Initially, every pixel in a given blotch field was assigned the same absorption and scattering depth profiles (however, these curves were subsequently adjusted at each pixel to yield unique curves). Next, integrated, "remote sensing" estimates of the modeled depth profiles were calculated; these values represent how the stratified surface layer would appear as a uniform layer to the sensor. Finally, the depth model parameters were iteratively adjusted until the integrated values (which were recalculated after each parameter adjustment) agreed to within 5% of the CASI-derived surface layer estimates. This technique essentially "slid" the curves along the axis to force agreement with the remotely sensed estimates. The curve shape was generally maintained except for minor adjustments to accommodate cases where low CASI values would have resulted in negative absorption or scattering coefficients at depth if adjustments were not made.

DATA AND METHODS

Depth profiles of beam attenuation (c) and absorption were collected with a WetLabs AC9 meter at 412, 456, 488, 532, 560, 650, 660, 676, and 715 nm at the time of the air-craft overflight. Scattering was calculated as the difference between c and a . Postprocessing of the data included removal of negative values, a temperature correction for $a715$ and $c715$, scattering corrections for all absorption wavelengths based on absorption at 715 nm, binning to one-foot depth intervals, addition of water absorption values (to yield total absorption coefficients), and linear interpolation to SeaWiFS wavelengths. Single scattering albedo is the ratio of scattering to total beam attenuation ($\omega_0 = b/c$) and provides an indication of whether the environment is dominated by absorption or scattering processes.

Remote sensing imagery collected with the CASI provided spatial coverage of the area resampled to a 2.5 m ground pixel resolution. The spectral bandset contained eleven channels set to coincide with the eight SeaWiFS wavelengths (412, 443, 490, 510, 555, 670, 765, 865 nm), plus three additional bands at 530, 585, and 595 nm. The CASI scans 512 pixels across the flight line within a 35° field of view (17° each side of nadir). The flight line analyzed here was collected at 1153 local time on 10 August, 1994, along a heading into the sun to reduce sun glint, at an altitude of 4000 feet. A 500 m² image sub-section extending from the shore seaward over the sand bar was selected for analysis.

The atmospheric correction routine applied to the CASI imagery and the theory related to remote sensing reflectance measurements are described in Gould and Arnone (In Press). The sequence of processing steps to produce 3-D volumetric optical fields from aircraft radiance imagery are summarized in Figure 2.

RESULTS

Depth profiles of a and b were measured concurrently with the aircraft overflight using an AC9 meter at five stations along an offshore transect. In Figures 3 and 4, the measured profiles are represented by the solid lines at six SeaWiFS wavelengths. For each wavelength and station, the measured profiles were approximated using the models described in Figures 5 and 6. The simulated depth profiles (model results) are represented by the dotted lines in Figures 3 and 4. A uniform depth profile was assumed for the measured straight line profiles. In all cases, the

simulated profiles closely approximate the measured profiles. The modeled curves and associated parameters represent the "initial guess" for the iteration process described in Figure 8.

The measured a and b profiles were simulated using a sigmoidal model, or, in the case of scattering at station 1, a bimodal Gaussian model superimposed on a constant back-ground. At that station inside the sand bar (see Figure 7), resuspension of bottom sediment apparently resulted in a highly scattering nepheloid layer. The model equations and the graphical significance of the parameters are shown in the idealized profiles depicted in Figures 5 and 6. Nonlinear least-squares curve fitting was used to find the parameters of the specified models by minimizing the chi-square values.

The bathymetry grid corresponding to the aircraft-derived surface a and b fields is shown in Figure 7. Depth estimates at each pixel were derived from the CASI water-leaving radiance measurements in the 510 nm channel and corresponding laser bathymetry measurements (radiance/depth relationship given in Figure 8). The shallow sand bar is depicted by the dark purple band in the upper third of the grid. The locations of the five AC9 stations are also shown.

The individual modeled depth profile shapes were subsequently applied to each pixel in the image by assigning the same curve shapes to pixels with expected similar hydrographic properties. In this shallow coastal environment, the distribution patterns appeared related to coastal run-off and river discharge (and therefore bathymetry, indirectly), so profile shapes were assigned to pixels based on the water depth at each location. All pixels in the 0-2.5 m depth range were initially assigned station 2 depth profile shapes (the red blotch field in Figure 7); all pixels inside the sand bar and deeper than 2.5 m were assigned station 1 profile shapes (the blue blotch field in Figure 4); etc.

The curve shapes were ultimately adjusted during the iteration procedure described in Figure 8. Table 1 lists the general absorption and scattering depth models applied at each station and wavelength. The bimodal Gaussian model was only applied for the scattering profile at station 1; a high-scattering resuspension layer was forced to follow 0.4 m above the bottom at all pixels in blotch area 1. Tables 2 and 3 list the nonlinear least squares regression results for the absorption and scattering model parameters.

An iterative method was developed to estimate the absorption and scattering depth profiles at each pixel in the image. Figure 8 outlines the steps involved and the equations used. The modeled depth profiles from Figures 3 and 4 represent the "initial guess" profiles which are subsequently adjusted to force the integrated values to match the aircraft-derived estimates. After looping over all pixels and wavelengths, we obtain horizontal image slices at 0.5 m increments from the surface to a depth of 7.0 m (the depth and increment can vary, as desired). The 15 image slices form a 3-D data volume for each wavelength.

In Figures 9-18, AC9-measured absorption and scattering profiles from the five stations are compared with model (CASI) results, for the six SeaWiFS wavelengths. The model results were extracted from the 3-D data volumes at the pixel location corresponding to the geographic locations of the AC9 stations. In general, the magnitudes and shapes of the modeled curves agree closely with the measured values, at all wavelengths for both absorption and scattering (the AC9 absorption at 555 nm is erroneously high due to an instrument filter problem). Larger deviations between measured and modeled absorption values at the blue-green wavelengths (400-510 nm wavelength range) are evident at the offshore stations 4 and 5.

Table 1. Absorption and Scattering Depth Models by Station and Wavelength.

Station	λ	Absorption Model	Scattering Model
1	412	Uniform	Bimodal Gaussian
	443	Uniform	Bimodal Gaussian
	490	Uniform	Bimodal Gaussian
	510	Uniform	Bimodal Gaussian
	555	Uniform	Bimodal Gaussian
	670	Uniform	Bimodal Gaussian
2	412	Uniform	Uniform
	443	Uniform	Uniform
	490	Uniform	Uniform
	510	Uniform	Uniform
	555	Uniform	Uniform
	670	Uniform	Uniform
3	412	Sigmoidal	Sigmoidal
	443	Sigmoidal	Sigmoidal
	490	Sigmoidal	Sigmoidal
	510	Sigmoidal	Sigmoidal
	555	Sigmoidal	Sigmoidal
	670	Uniform	Sigmoidal
4	412	Sigmoidal	Sigmoidal
	443	Sigmoidal	Sigmoidal
	490	Sigmoidal	Sigmoidal
	510	Sigmoidal	Sigmoidal
	555	Sigmoidal	Sigmoidal
	670	Uniform	Sigmoidal
5	412	Sigmoidal	Sigmoidal
	443	Sigmoidal	Sigmoidal
	490	Sigmoidal	Sigmoidal
	510	Sigmoidal	Sigmoidal
	555	Sigmoidal	Sigmoidal
	670	Uniform	Sigmoidal

Table 2. Absorption Depth Model Parameter Values by Station and Wavelength.

Station	λ	A_1	A_2	Z_0	dZ
1	412
	443
	490
	510
	555
	670
2	412
	443
	490
	510
	555
	670
3	412	0.91848	0.52841	2.08767	0.34509
	443	0.65462	0.39466	2.09158	0.34302
	490	0.37526	0.24343	2.08349	0.35215
	510	0.30758	0.20875	2.09334	0.33933
	555	0.30551	0.24304	2.15120	0.25444
	670
4	412	0.93237	0.51503	2.44046	0.34587
	443	0.66397	0.38190	2.43632	0.34624
	490	0.37927	0.23578	2.44239	0.33957
	510	0.31081	0.20208	2.46390	0.32991
	555	0.31413	0.23605	2.46495	0.33640
	670
5	412	0.91877	0.48912	1.43572	0.21651
	443	0.65259	0.36598	1.42872	0.21194
	490	0.37183	0.22753	1.42294	0.20299
	510	0.30516	0.19684	1.42716	0.19678
	555	0.31013	0.23660	1.39946	0.18978
	670

Table 3. Scattering Depth Model Parameter Values by Station and Wavelength.

Station	λ	$A_1 (B_0)$	$A_2 (h_1, h_2)$	$Z_0 (Z_{m1}, Z_{m2})$	$dZ (\sigma_1, \sigma_2)$
1	412	(0.79003)	(0.02236, 0.07286)	(0.56668, $Z_b - 0.4$)	(0.1308, 0.18598)
	443	(0.75970)	"	"	"
	490	(0.71606)	"	"	"
	510	(0.66837)	"	"	"
	555	(0.63125)	"	"	"
	670	(0.48819)	"	"	"
2	412
	443
	490
	510
	555
	670
3	412	0.72878	0.41269	1.97419	0.32456
	443	0.69634	0.39935	1.99286	0.32597
	490	0.64926	0.38958	2.02062	0.32939
	510	0.60475	0.35947	2.01947	0.33881
	555	0.57912	0.34229	1.98089	0.36951
	670	0.43928	0.28438	1.97181	0.39498
4	412	0.63429	0.31302	2.49738	0.22269
	443	0.60805	0.30331	2.51377	0.20354
	490	0.57096	0.29643	2.54444	0.17284
	510	0.52859	0.26599	2.55230	0.16387
	555	0.49991	0.24958	2.55967	0.15465
	670	0.38084	0.20196	2.58522	0.12600
5	412	0.62419	0.28352	1.46587	0.15270
	443	0.59584	0.27017	1.46584	0.14902
	490	0.56202	0.26304	1.46506	0.14387
	510	0.52200	0.22910	1.45096	0.16264
	555	0.49152	0.21144	1.45106	0.15868
	670	0.37346	0.16777	1.47388	0.13662

In Figures 21-30, AC9-measured absorption and scattering spectra from the five stations are compared with model (CASI) results, at 0.5 - 1.0 m depth increments from the surface to the bottom. A single line in any of the plots indicates no change in the spectra with depth. Uniform absorption profiles are observed at stations 1 and 2. At stations 3 - 5, the change in the measured absorption spectral shape with depth (decreasing absorption in the 400-530 nm spectral range) is reflected in the model results. For scattering, the spectral shapes are fairly uniform with depth at all stations, but the magnitudes change. A uniform scattering profile is observed only at station 2. At station 1, a near-bottom increase in scattering is observed in the 2.5 - 3.0 m depth range (see Figure 14 also). At stations 3, the scattering coefficient decreases with depth across the spectrum and the modeled values are slightly higher than the measured values. At stations 4 and 5, uniform absorption and scattering values are observed below the shallow lens of nearshore water.

AC9-measured absorption and scattering coefficients are scatter plotted against model (CASI) results, for all stations, depths, and wavelengths in Figures 31 - 32. The number symbols in each plot represent the station designations and the solid diagonal line represents a one-to-one correspondence between measured and modeled values. At all wavelengths and depths, the modeled absorption values underestimate the measured values, with greater discrepancy at the offshore stations 4 and 5. For scattering, the modeled coefficients more closely matched the measured values. These data points all cluster along the one-to-one line, regardless of station, depth, or wavelength.

Distribution patterns of absorption, scattering, and single scattering albedo at the surface, 1.5 m, 2.5 m, 3.0 m, 3.5 m, and 6.0 m are shown in Figures 33 - 50. The figures represent horizontal slices through the 3-D data volumes at the depths indicated for each of the five SeaWiFS wavelengths. For both absorption and scattering, highest values are observed nearshore and over the sand bar, with lower values seaward. Also, both a and b decrease with depth outside the sand bar as the successively deeper slices pass through the nearshore surface lens of higher optical values. The near-bottom sediment resuspension is apparent inside the sand bar in the 2.5-3.5 m scattering slices. The black pixels in the images represent the intersection of the given depth slice with the shore or the bottom.

3-D data volumes of absorption, scattering, and single scattering albedo from the depth model results are shown in Figures 51 - 56, for each of the six SeaWiFS wavelengths. The shore and sand bar are indicated for orientation. Note the change in the color scale for a and ω_0 between the images (b scale remains constant). A band of highly absorbing and highly scattering water is evident near shore and over the sand bar at all wavelengths. The layer extends seaward with lower values that decrease rapidly with depth, forming a narrowing lens about 2.5 m thick. Low and fairly uniform a and b values are observed offshore below the lens. At 412 nm, ω_0 is lowest in the nearshore band (indicating a more absorption-dominated environment there) with higher values offshore and at depth. Absorption by dissolved organic matter (DOM) associated with river run-off dominates at this wavelength. The opposite pattern is observed for ω_0 at 555 nm, with highest values nearshore and in the surface lens offshore. Particle scattering dominates at this wavelength with little absorption by DOM or phytoplankton pigments.

SUMMARY AND CONCLUSIONS

Surface estimates of a and b derived from aircraft imagery over a coastal area off Florida were pushed to depth to produce 3-D volumetric fields of the optical environment. Measured optical depth profiles at five stations were modeled using a bimodal Gaussian or a sigmoidal parameterization. An iterative technique was developed to adjust these curves to match the surface layer, remote sensing-derived estimates. Unique a , b , and ω_0 depth distributions were thus defined at each pixel in the image. Depth model results compared favorably (both spatially and spectrally) with measured values. The 3-D visualization of the optical fields provided insight into the biological and physical processes affecting DOM and particle distributions in this coastal area.

ACKNOWLEDGMENTS

The authors wish to thank Borstad & Assoc. for their efforts with the collection of the CASI aircraft data. This research was supported by the Littoral Optical Environment PE62435 and the Spectral Signatures PE0601153N programs at the Naval Research Laboratory.

REFERENCES

Gordon, H.R., and D.K. Clark. 1980. Remote sensing optical properties of a stratified ocean: an improved interpretation. *Appl. Opt.*, 19(20): 3428-3430.

Gordon, H.R., and W.R. McCluney. 1975. Estimation of the depth of sunlight penetration in the sea for remote sensing. *Appl. Opt.* 14(2): 413-416.

Gould, R.W., Jr. and R.A. Arnone. In Press. Remote sensing estimates of inherent optical properties in a coastal environment. *Rem. Sens. Environ.*

Lewis, M.R., J.J. Cullen, and T. Platt. 1983. Phytoplankton and thermal structure in the upper ocean: consequences of nonuniformity in the chlorophyll profile. *J. Geophys. Res.*, 88: 2,565-2,570.

Platt, T., C. Caverhill, and S. Sathyendranath. 1991. Basin-scale estimates of oceanic primary production by remote sensing: The North Atlantic. *J. Geophys. Res.*, 96(C8): 15,147-15,159.

Platt, T., S. Sathyendranath, C.M. Caverhill and M.R. Lewis. 1988. Ocean primary production and available light: further algorithms for remote sensing. *Deep-Sea Res.*, 35(6): 855-879.

Sathyendranath, S. and T. Platt. 1989. Remote sensing of ocean chlorophyll: consequences of nonuniform pigment profiles. *Appl. Opt.*, 28: 490-495.

FIGURE LEGENDS

Figure 1. Landsat TM image of the study site on 10 August, 1994, the day of the CASI overflights.

Figure 2. Raw CASI radiance image showing the locations of the moorings relative to the sand bar (the bright band just above the middle of the image. The processing steps are also outlined.

Figure 3. Measured vs. modeled absorption depth profiles, all five stations and all six SeaWiFS wavelengths.

Figure 4. Measured vs. modeled scattering depth profiles, all five stations and all six SeaWiFS wavelengths.

Figure 5. Idealized sigmoidal depth profile model.

Figure 6. Idealized bimodal Gaussian depth profile model.

Figure 7. Bathymetry grid and associated blotch fields.

Figure 8. Summary of the iterative procedure for estimating depth profiles.

Figure 9. Station 1, absorption coefficient vs. depth, comparison of measured (AC9) and modeled (CASI) values. Each line is a separate wavelength.

Figure 10. Station 2, absorption coefficient vs. depth, comparison of measured (AC9) and modeled (CASI) values. Each line is a separate wavelength.

Figure 11. Station 3, absorption coefficient vs. depth, comparison of measured (AC9) and modeled (CASI) values. Each line is a separate wavelength.

Figure 12. Station 4, absorption coefficient vs. depth, comparison of measured (AC9) and modeled (CASI) values. Each line is a separate wavelength.

Figure 13. Station 5, absorption coefficient vs. depth, comparison of measured (AC9) and modeled (CASI) values. Each line is a separate wavelength.

Figure 14. Station 1, scattering coefficient vs. depth, comparison of measured (AC9) and modeled (CASI) values. Each line is a separate wavelength.

Figure 15. Station 2, scattering coefficient vs. depth, comparison of measured (AC9) and

modeled (CASI) values. Each line is a separate wavelength.

Figure 16. Station 3, scattering coefficient vs. depth, comparison of measured (AC9) and modeled (CASI) values. Each line is a separate wavelength.

Figure 17. Station 4, scattering coefficient vs. depth, comparison of measured (AC9) and modeled (CASI) values. Each line is a separate wavelength.

Figure 18. Station 5, scattering coefficient vs. depth, comparison of measured (AC9) and modeled (CASI) values. Each line is a separate wavelength.

Figure 19. Surface absorption vs. wavelength, comparison of measured (AC9) and modeled (CASI) values. Each line is a separate station.

Figure 20. Surface scattering vs. wavelength, comparison of measured (AC9) and modeled (CASI) values. Each line is a separate station.

Figure 21. Station 1, absorption coefficient vs. wavelength, comparison of measured (AC9) and modeled (CASI) values. Each line is a separate depth. A single line indicates uniform values with depth.

Figure 22. Station 2, absorption coefficient vs. wavelength, comparison of measured (AC9) and modeled (CASI) values. Each line is a separate depth. A single line indicates uniform values with depth.

Figure 23. Station 3, absorption coefficient vs. wavelength, comparison of measured (AC9) and modeled (CASI) values. Each line is a separate depth.

Figure 24. Station 4, absorption coefficient vs. wavelength, comparison of measured (AC9) and modeled (CASI) values. Each line is a separate depth.

Figure 25. Station 5, absorption coefficient vs. wavelength, comparison of measured (AC9) and modeled (CASI) values. Each line is a separate depth.

Figure 26. Station 1, scattering coefficient vs. wavelength, comparison of measured (AC9) and modeled (CASI) values. Each line is a separate depth.

Figure 27. Station 2, scattering coefficient vs. wavelength, comparison of measured (AC9) and modeled (CASI) values. Each line is a separate depth. A single line indicates uniform values with depth.

Figure 28. Station 3, scattering coefficient vs. wavelength, comparison of measured (AC9) and modeled (CASI) values. Each line is a separate depth.

Figure 29. Station 4, scattering coefficient vs. wavelength, comparison of measured (AC9) and modeled (CASI) values. Each line is a separate depth.

Figure 30. Station 5, scattering coefficient vs. wavelength, comparison of measured (AC9) and modeled (CASI) values. Each line is a separate depth.

Figure 31. Measured (AC9) vs. modeled (CASI) absorption coefficients, all depths and stations. Each of the six SeaWiFS wavelengths is plotted separately.

Figure 32. Measured (AC9) vs. modeled (CASI) scattering coefficients, all depths and stations. Each of the six SeaWiFS wavelengths is plotted separately.

Figure 33. Modeled absorption coefficients at 412 nm. Each image is a separate horizontal depth slice. Black pixels indicate shore or the intersection of the slice with the bottom.

Figure 34. Modeled absorption coefficients at 443 nm. Each image is a separate horizontal depth slice. Black pixels indicate shore or the intersection of the slice with the bottom.

Figure 35. Modeled absorption coefficients at 490 nm. Each image is a separate horizontal depth slice. Black pixels indicate shore or the intersection of the slice with the bottom.

Figure 36. Modeled absorption coefficients at 510 nm. Each image is a separate horizontal depth slice. Black pixels indicate shore or the intersection of the slice with the bottom.

Figure 37. Modeled absorption coefficients at 555 nm. Each image is a separate horizontal depth slice. Black pixels indicate shore or the intersection of the slice with the bottom.

Figure 38. Modeled absorption coefficients at 670 nm. Each image is a separate horizontal depth slice. Black pixels indicate shore or the intersection of the slice with the bottom.

Figure 39. Modeled scattering coefficients at 412 nm. Each image is a separate horizontal depth slice. Black pixels indicate shore or the intersection of the slice with the bottom.

Figure 40. Modeled scattering coefficients at 443 nm. Each image is a separate horizontal depth slice. Black pixels indicate shore or the intersection of the slice with the bottom.

Figure 41. Modeled scattering coefficients at 490 nm. Each image is a separate horizontal depth slice. Black pixels indicate shore or the intersection of the slice with the bottom.

Figure 42. Modeled scattering coefficients at 510 nm. Each image is a separate horizontal depth slice. Black pixels indicate shore or the intersection of the slice with the bottom.

Figure 43. Modeled scattering coefficients at 555 nm. Each image is a separate horizontal depth

slice. Black pixels indicate shore or the intersection of the slice with the bottom.

Figure 44. Modeled scattering coefficients at 670 nm. Each image is a separate horizontal depth slice. Black pixels indicate shore or the intersection of the slice with the bottom.

Figure 45. Modeled single scattering albedo at 412 nm. Each image is a separate horizontal depth slice. Black pixels indicate shore or the intersection of the slice with the bottom.

Figure 46. Modeled single scattering albedo at 443 nm. Each image is a separate horizontal depth slice. Black pixels indicate shore or the intersection of the slice with the bottom.

Figure 47. Modeled single scattering albedo at 490 nm. Each image is a separate horizontal depth slice. Black pixels indicate shore or the intersection of the slice with the bottom.

Figure 48. Modeled single scattering albedo at 510 nm. Each image is a separate horizontal depth slice. Black pixels indicate shore or the intersection of the slice with the bottom.

Figure 49. Modeled single scattering albedo at 555 nm. Each image is a separate horizontal depth slice. Black pixels indicate shore or the intersection of the slice with the bottom.

Figure 50. Modeled single scattering albedo at 670 nm. Each image is a separate horizontal depth slice. Black pixels indicate shore or the intersection of the slice with the bottom.

Figure 51. 3-D data volumes for absorption, scattering, and single scattering albedo at 412 nm.

Figure 52. 3-D data volumes for absorption, scattering, and single scattering albedo at 443 nm.

Figure 53. 3-D data volumes for absorption, scattering, and single scattering albedo at 490 nm.

Figure 54. 3-D data volumes for absorption, scattering, and single scattering albedo at 510 nm.

Figure 55. 3-D data volumes for absorption, scattering, and single scattering albedo at 555 nm.

Figure 56. 3-D data volumes for absorption, scattering, and single scattering albedo at 670nm.

Study
Site:

Ft. Walton
Beach, Fl

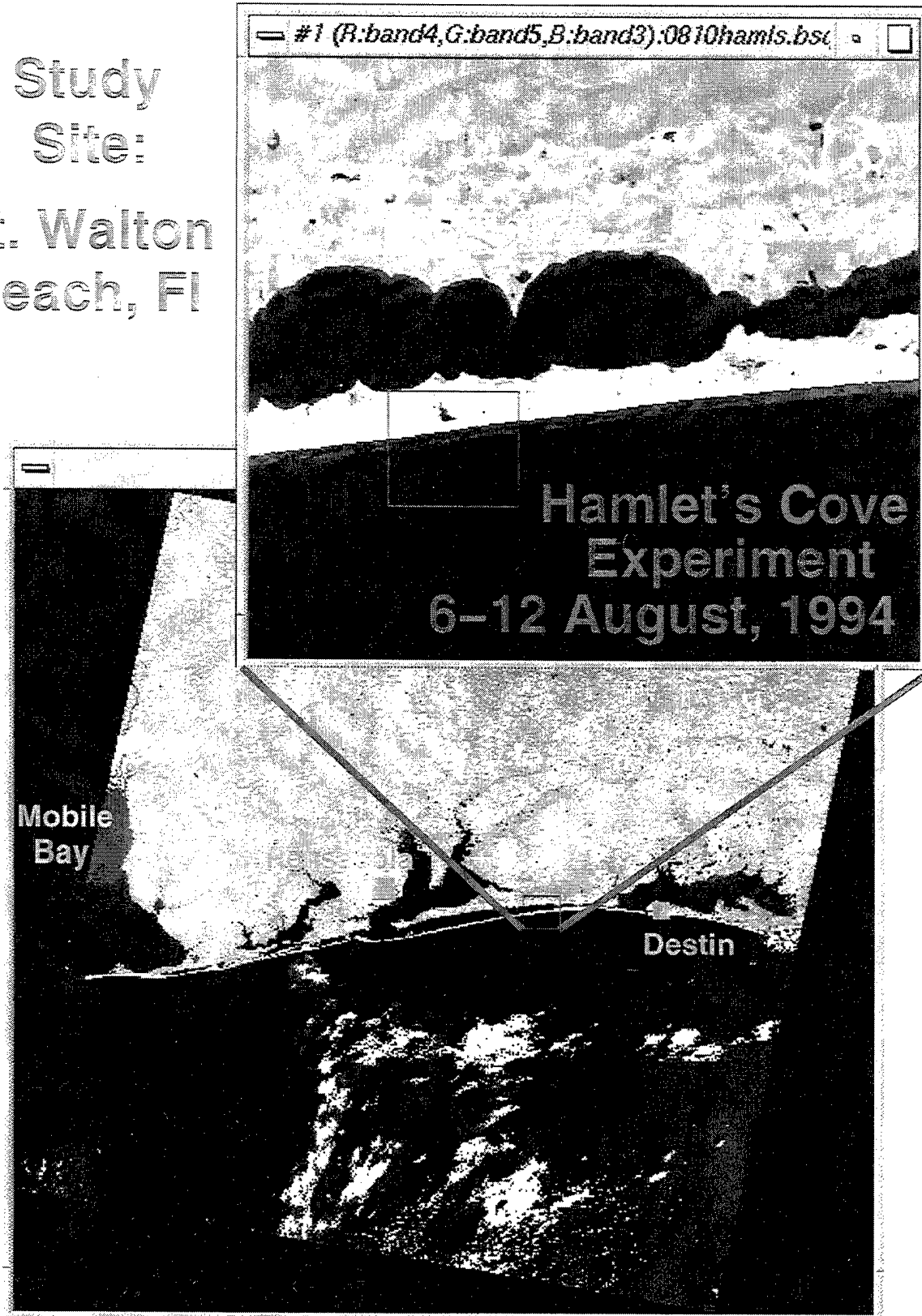
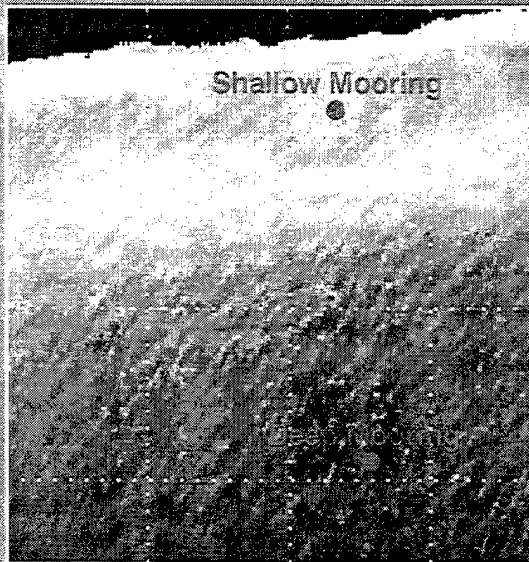


Fig. 1

Processing



- Import raw OLI/OL2 imagery (6 bands)
- Apply atmospheric correction
- Remove bottom reflectance component
- Apply modified SeafMS optical model to estimate surface a , b values
- Iterate depth profile model parameters to obtain subsurface estimates of a , b , ω_0
- Repeat for all pixels $\forall \lambda$'s



Produce 3-D Volumetric a , b , ω_0 fields
(0.5 m intervals from surface to bottom)

Fig. 2

Measured vs. Modeled Absorption

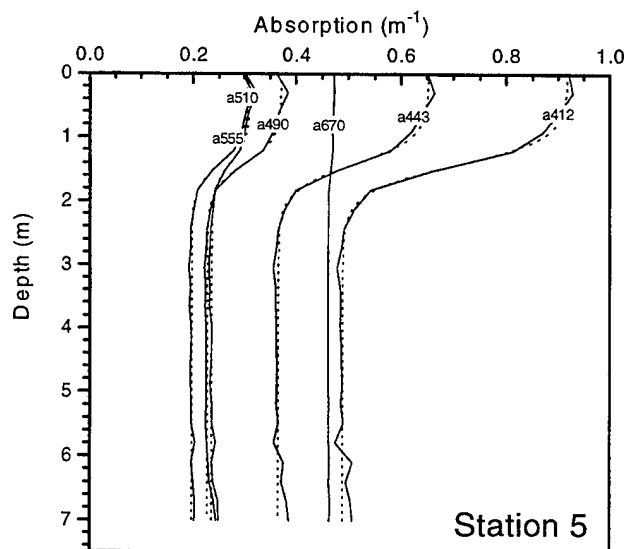
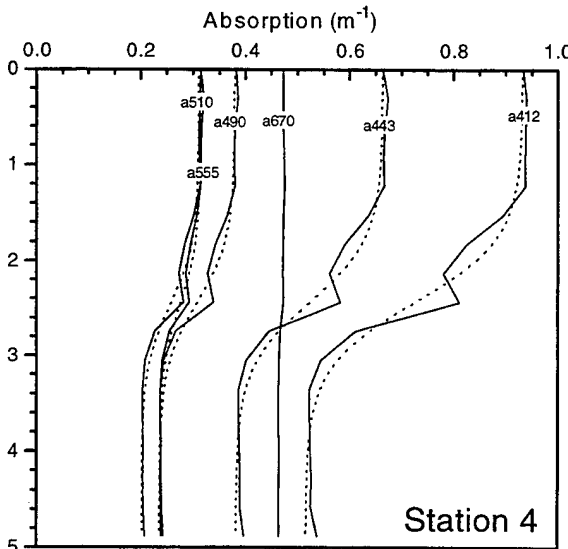
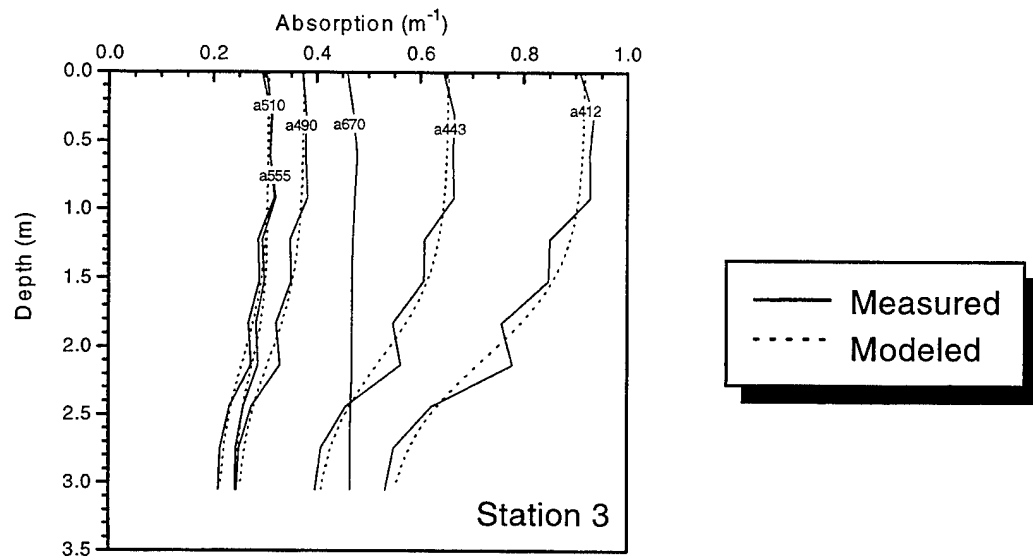
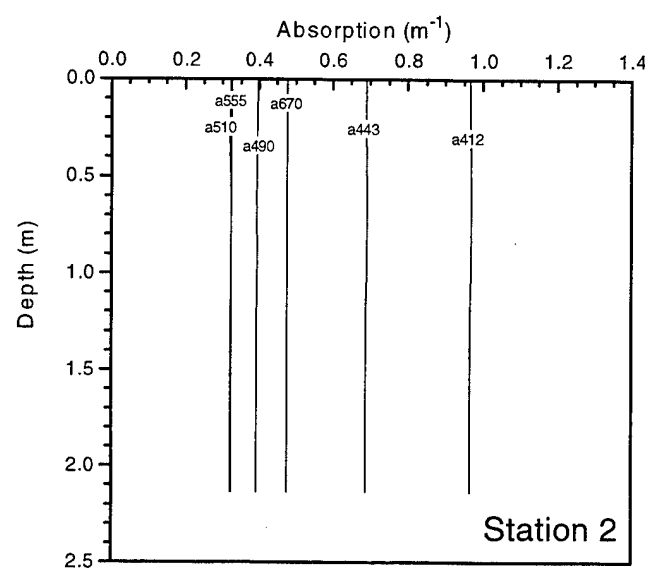
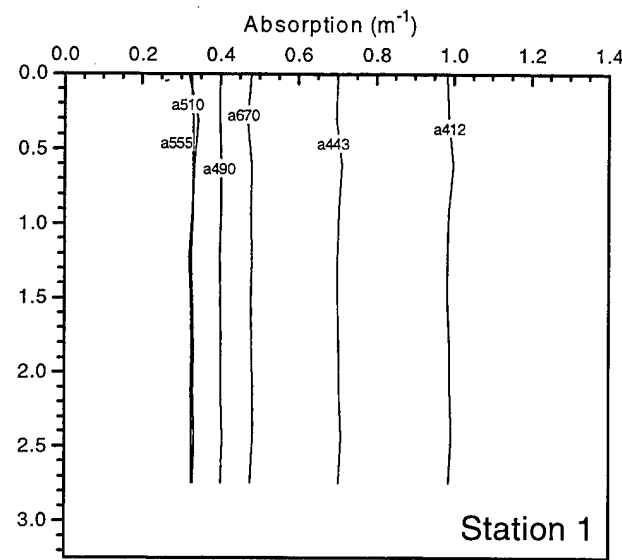


Fig. 3

Measured vs. Modeled Scattering

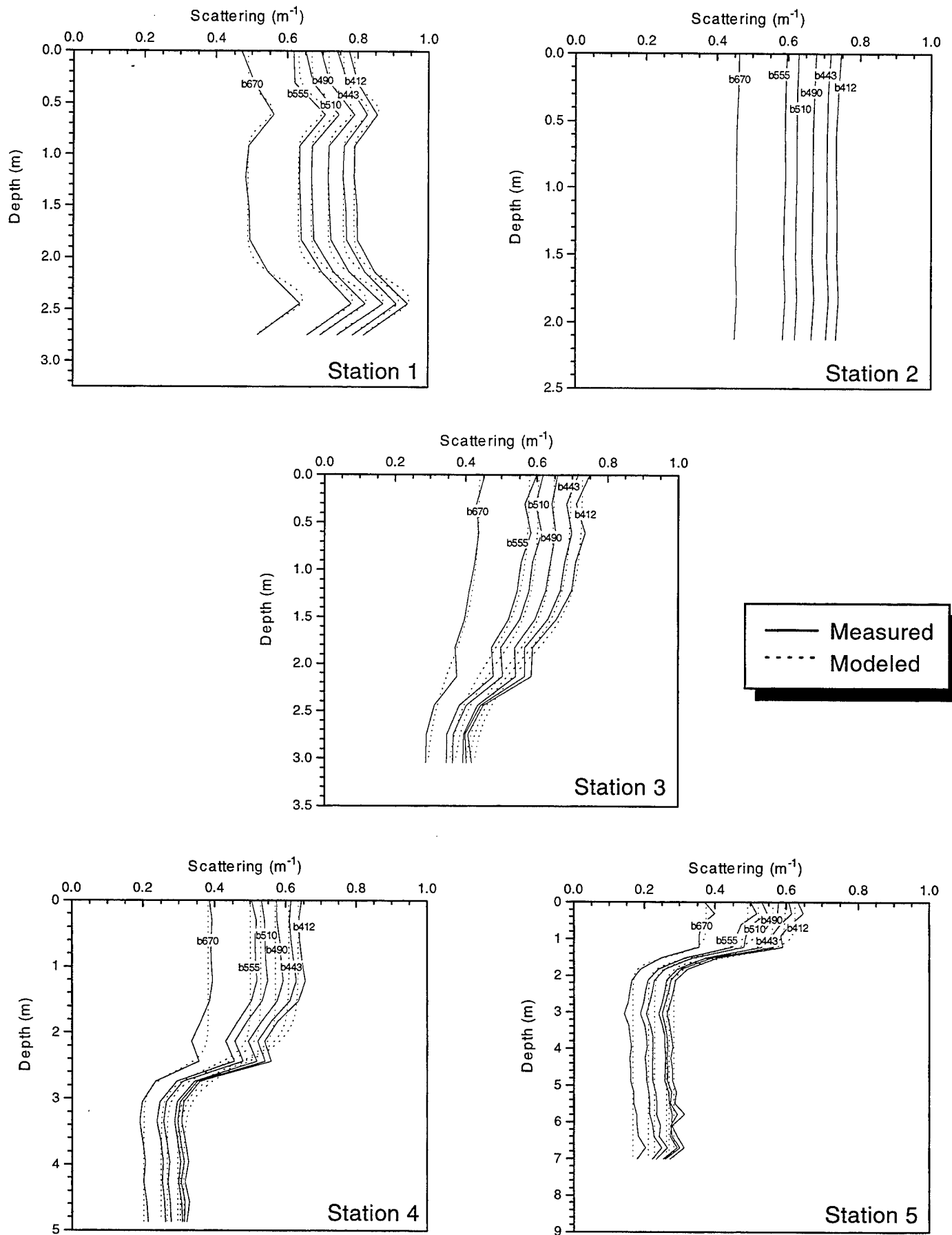


Fig. 4

Idealized Sigmoidal Model for Absorption, Scattering vs. Depth

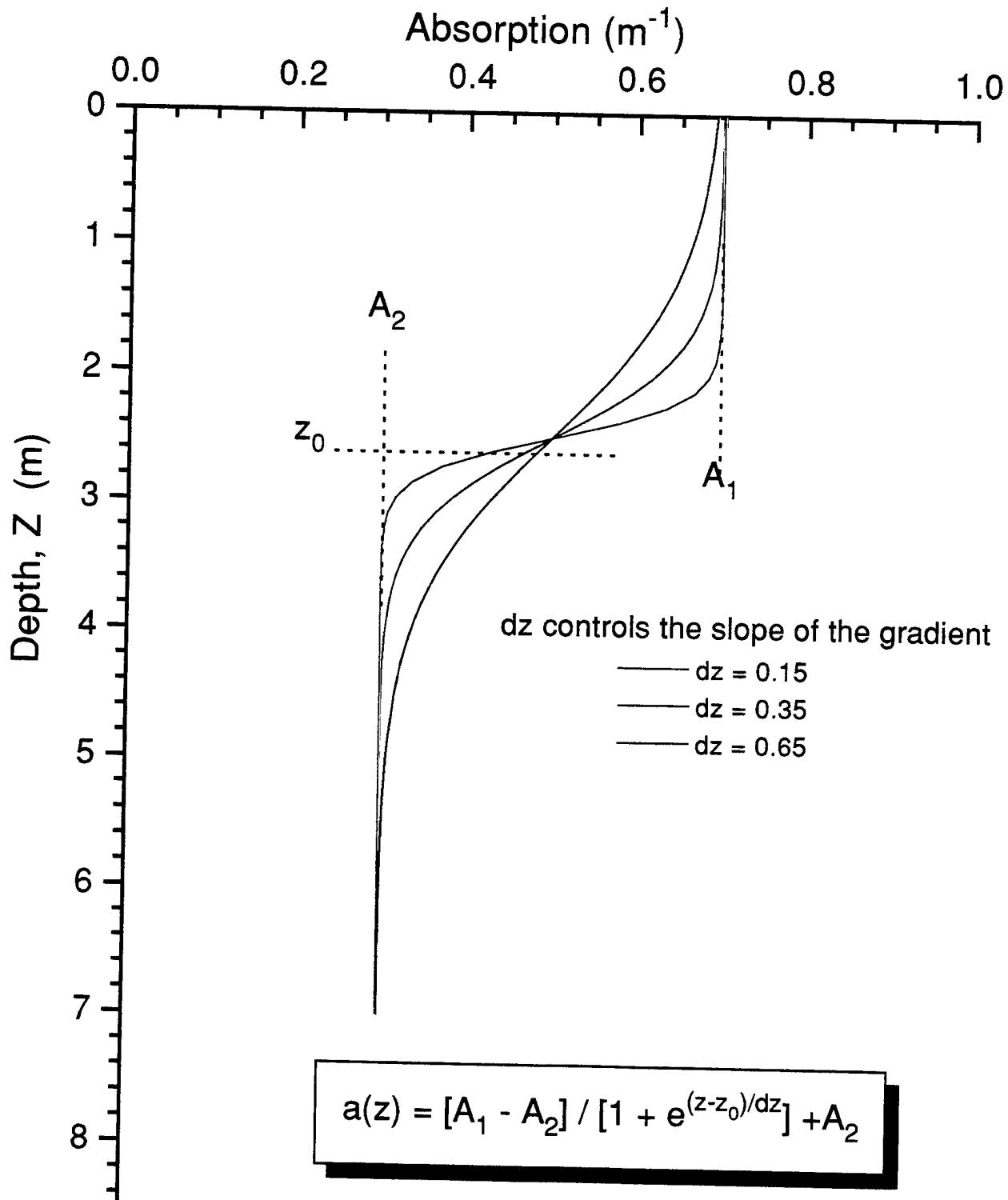


Fig. 5

Idealized Bimodal Gaussian Model for Scattering vs. Depth

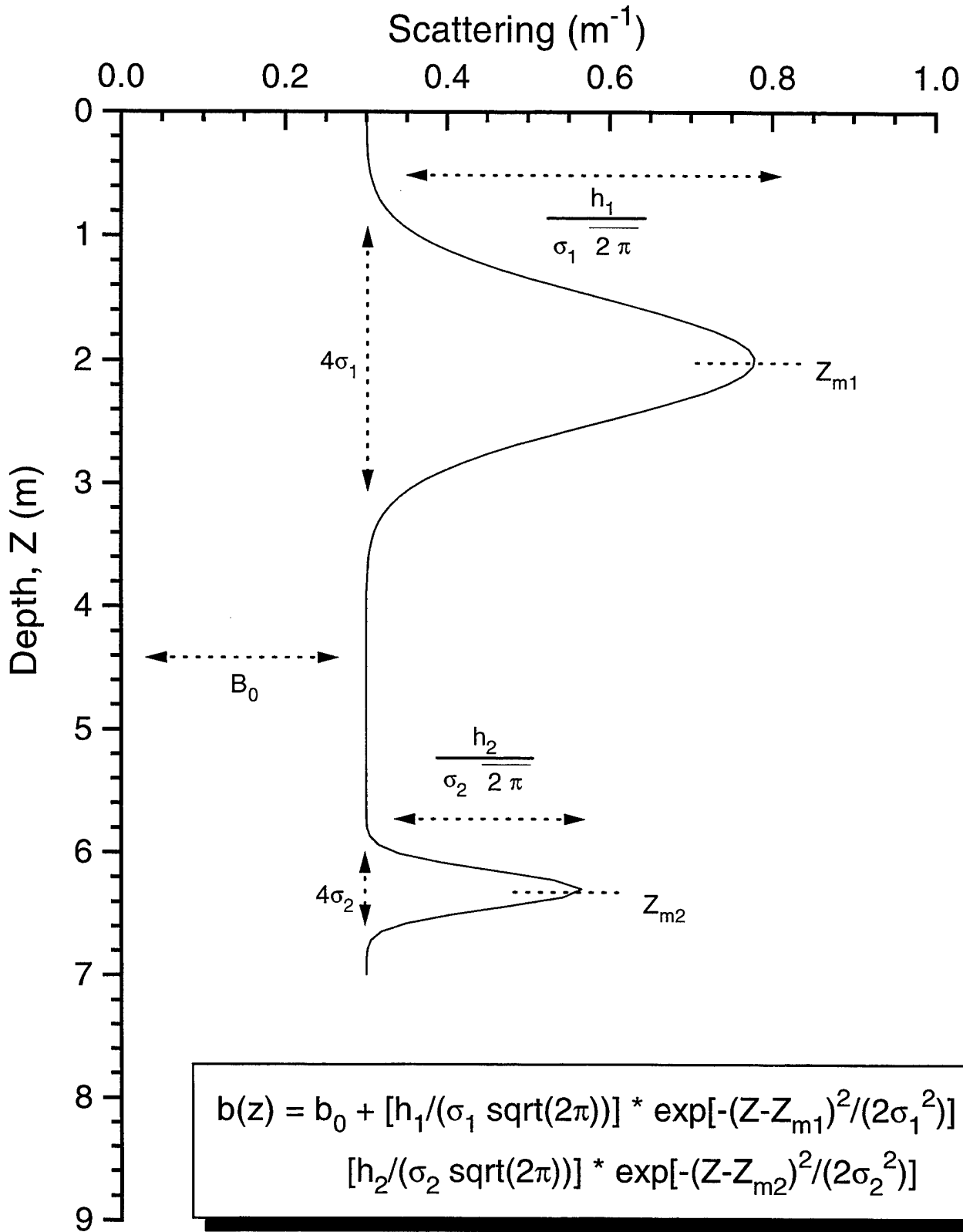


Fig. 6

Hamlet's Cove, 10 August 1994

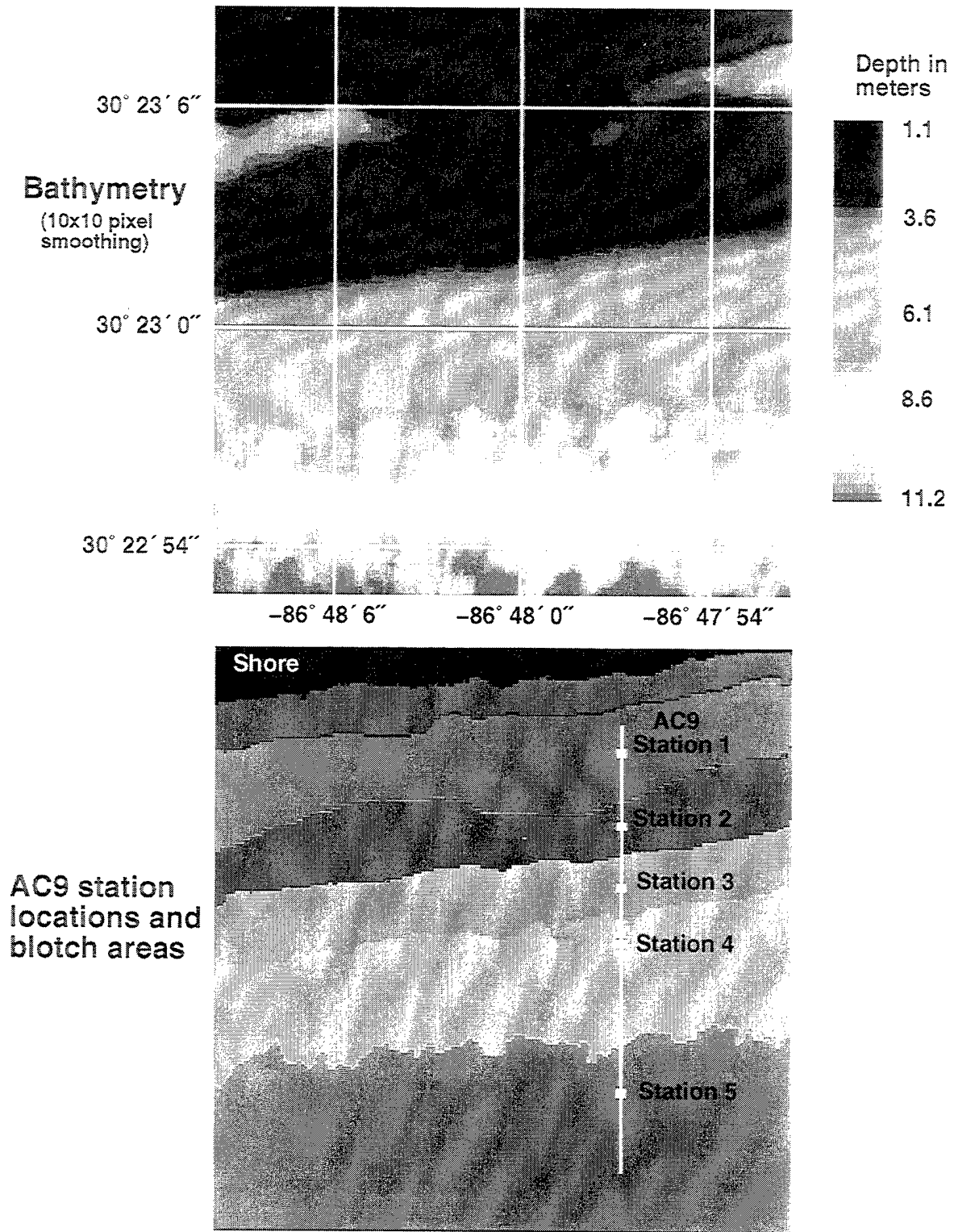
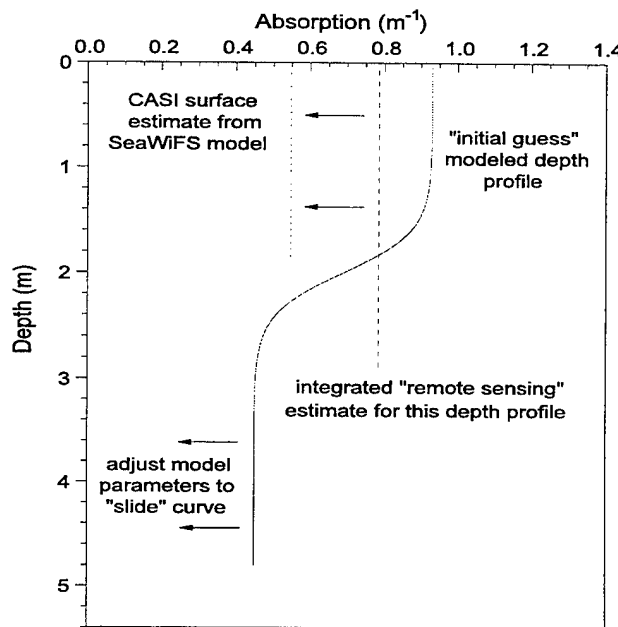


Fig. 7

Iterative Estimation of Absorption and Scattering Depth Profiles at Each Pixel



1. Calculate $K_d(\lambda)$ depth profile from "initial guess" $a(\lambda)$ and $b(\lambda)$ depth profiles measured with AC9:

$$K_d = a/\mu_{sw} [1 + (0.425 \mu_{sw} - 0.19) b/a]^{1/2}, \text{ and}$$

$$\mu_{sw} = \cos [\sin^{-1}(1/n_w \sin \theta_s)]$$

where K_d is the downwelling diffuse attenuation coefficient, n_w is the sea water index of refraction, θ_s is the solar zenith angle, and μ_{sw} is the cosine of the refracted solar angle.

2. Integrate $a(\lambda)$ and $b(\lambda)$ depth profiles to obtain "remote sensing" estimates (i.e., what a remote sensor would see):

$$a(\lambda) = \int^{zb} a(z) f(z) dz / \int^{zb} f(z) dz, \text{ and}$$

$$f(z) = \exp [- \int^{zb} 2K(z) dz]$$

where z_b is bottom depth determined at each pixel from the CASI 510 nm radiance channel:

$$z_b = 1.05161 A + 0.24542 A^2, \text{ and}$$

$$A = 4106.94 \cdot (CH \ 510)^{(-0.987818)}$$

3. Compare integrated a and b calculations to CASI estimates; if both agree within 5%, a and b depth profiles are defined.

4. If integrated and CASI values do not agree within 5%, adjust the a and b depth model parameters to shift the integrated values toward the CASI values. Repeat steps 1-3 until the values converge.

5. Calculate single scattering albedo, ω_0 :

$$\omega_0 = b / (a + b)$$

6. Loop over all pixels and wavelengths.

7. Output $a(\lambda)$, $b(\lambda)$, and $\omega_0(\lambda)$ every 0.5 m from the surface to the bottom.

Fig. 8

Hamlet's Cove Station 1
Absorption Depth Profiles vs. Wavelength

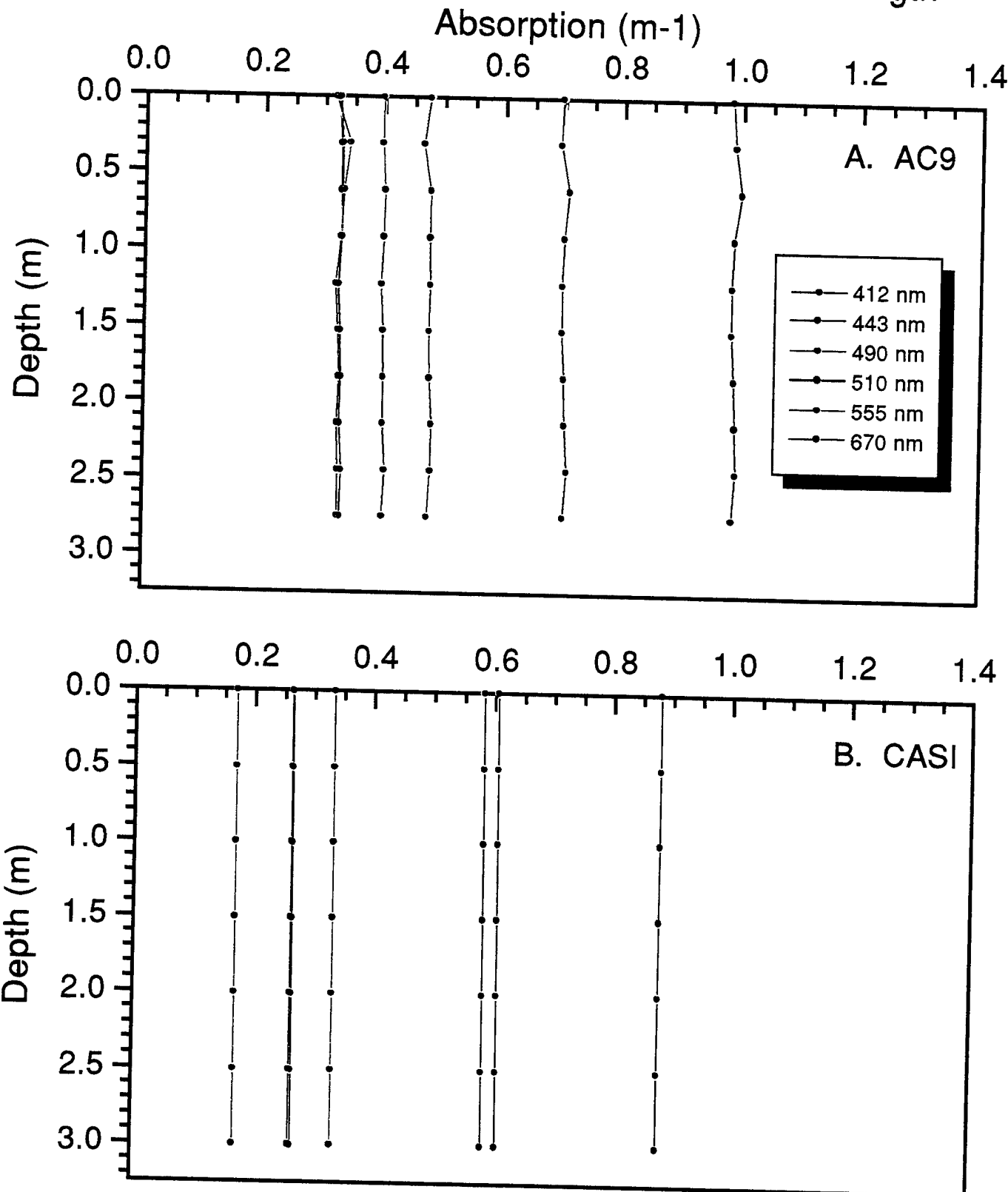


Fig. 9

Hamlet's Cove Station 2
Absorption Depth Profiles vs. Wavelength

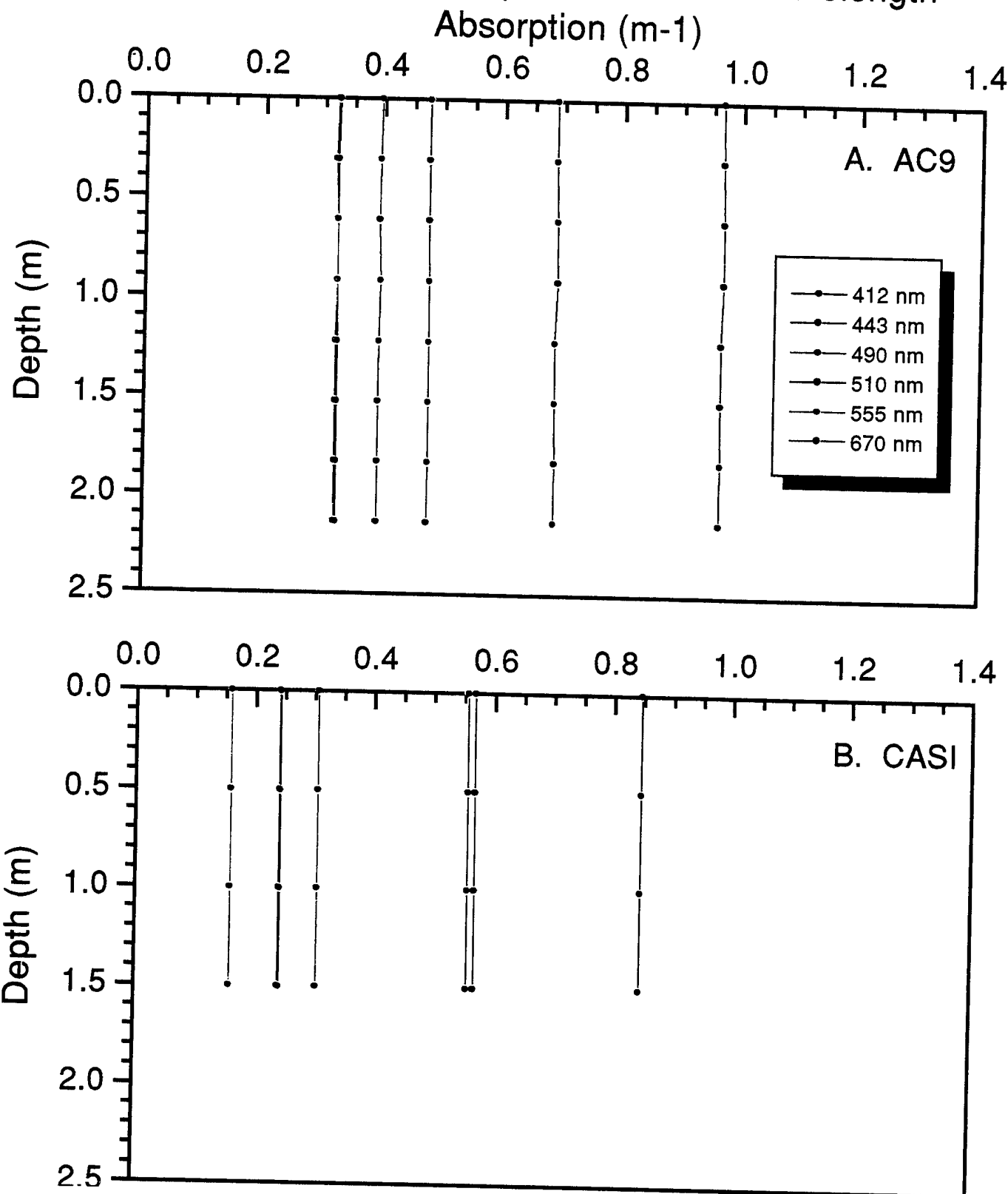


Fig. 10

Hamlet's Cove Station 3
Absorption Depth Profiles vs. Wavelength

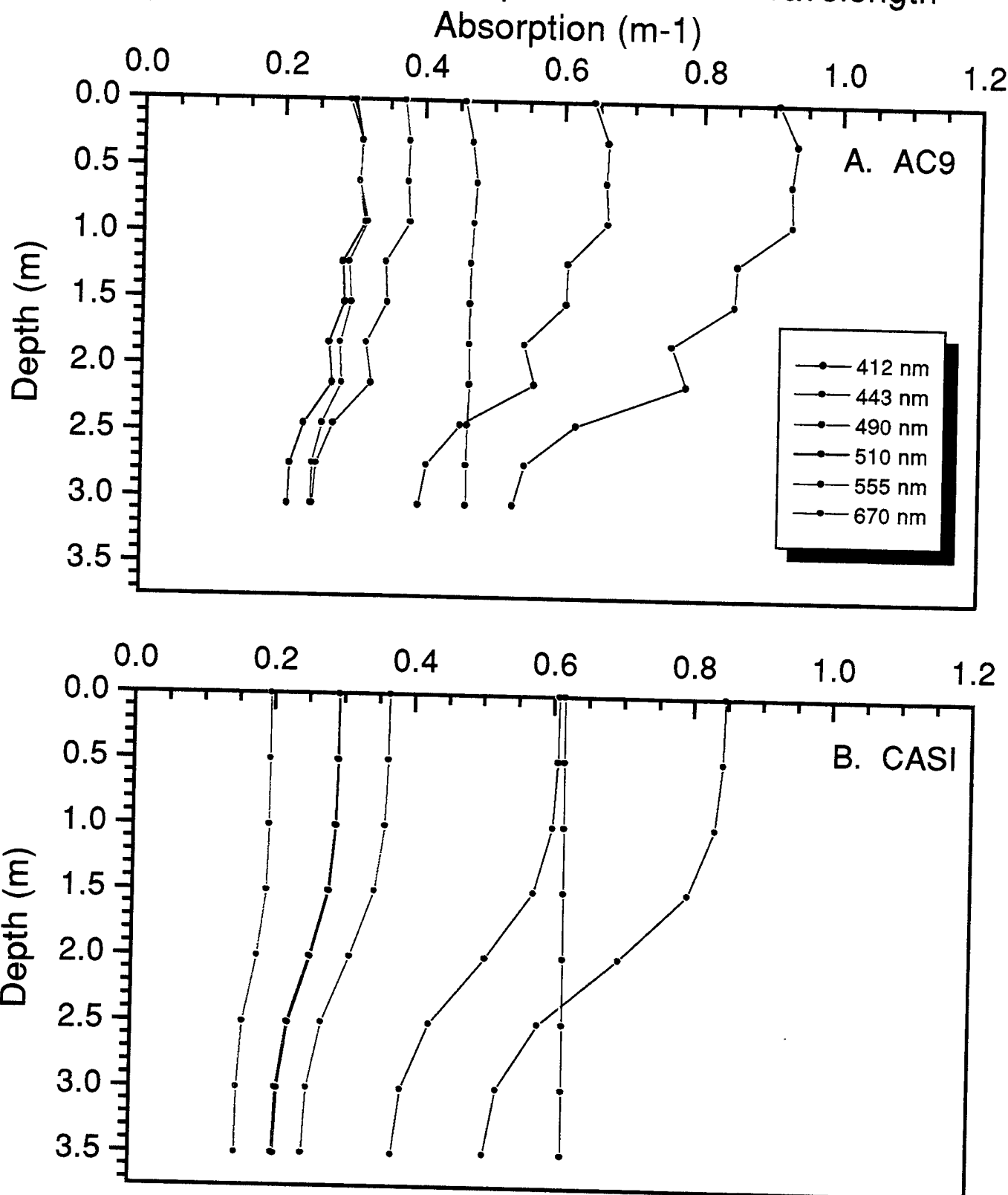


Fig. 11

Hamlet's Cove Station 4
Absorption Depth Profiles vs. Wavelength

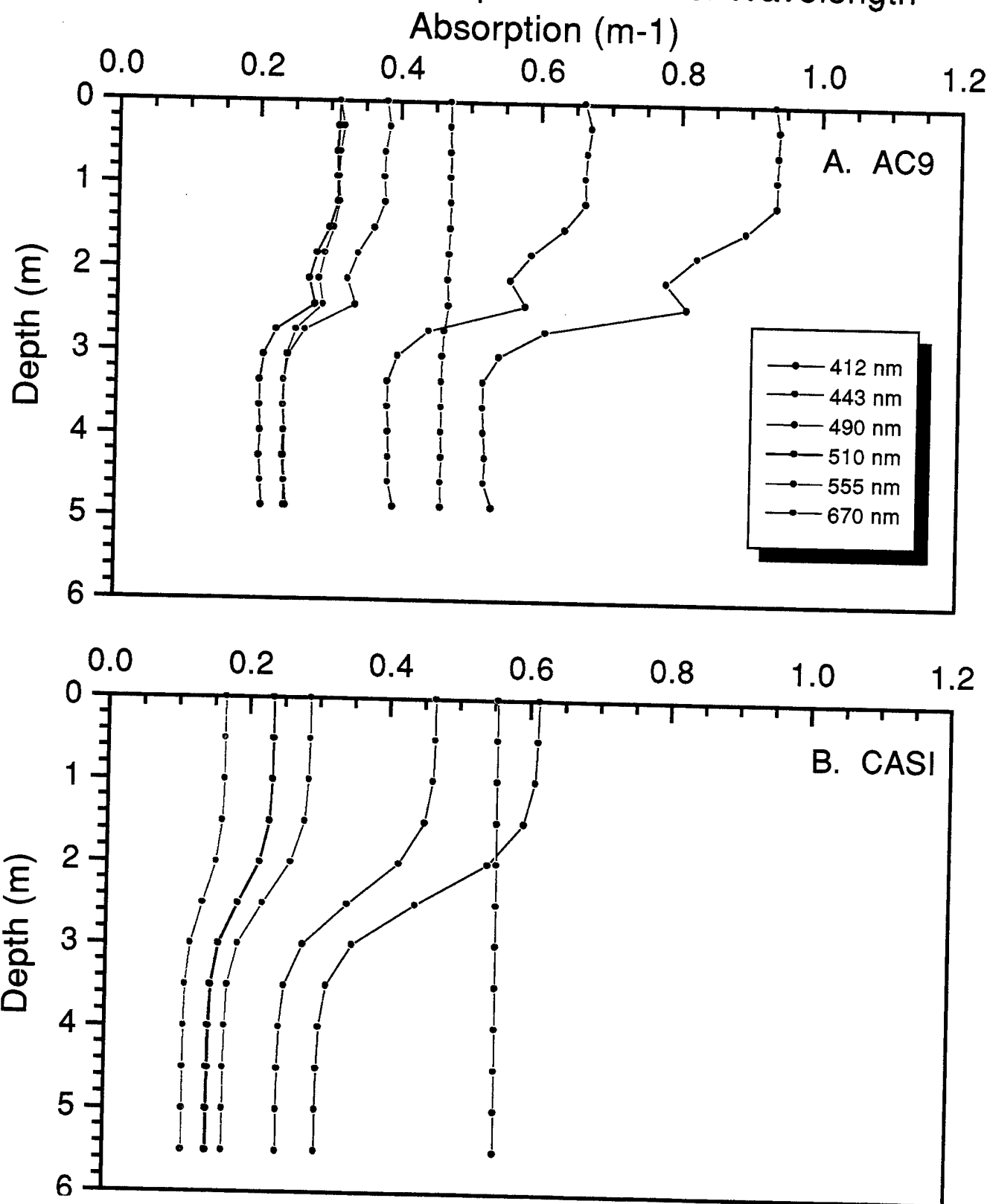


Fig. 12

Hamlet's Cove Station 5
Absorption Depth Profiles vs. Wavelength

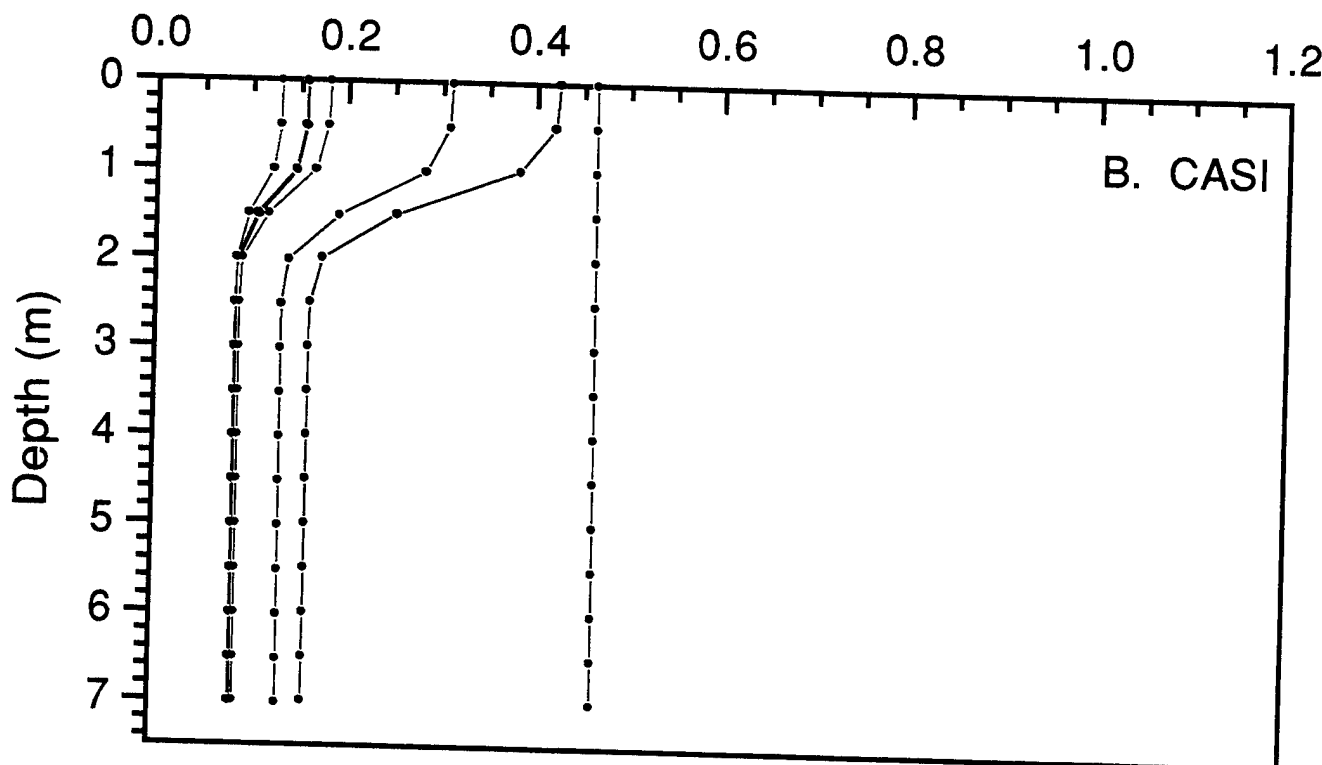
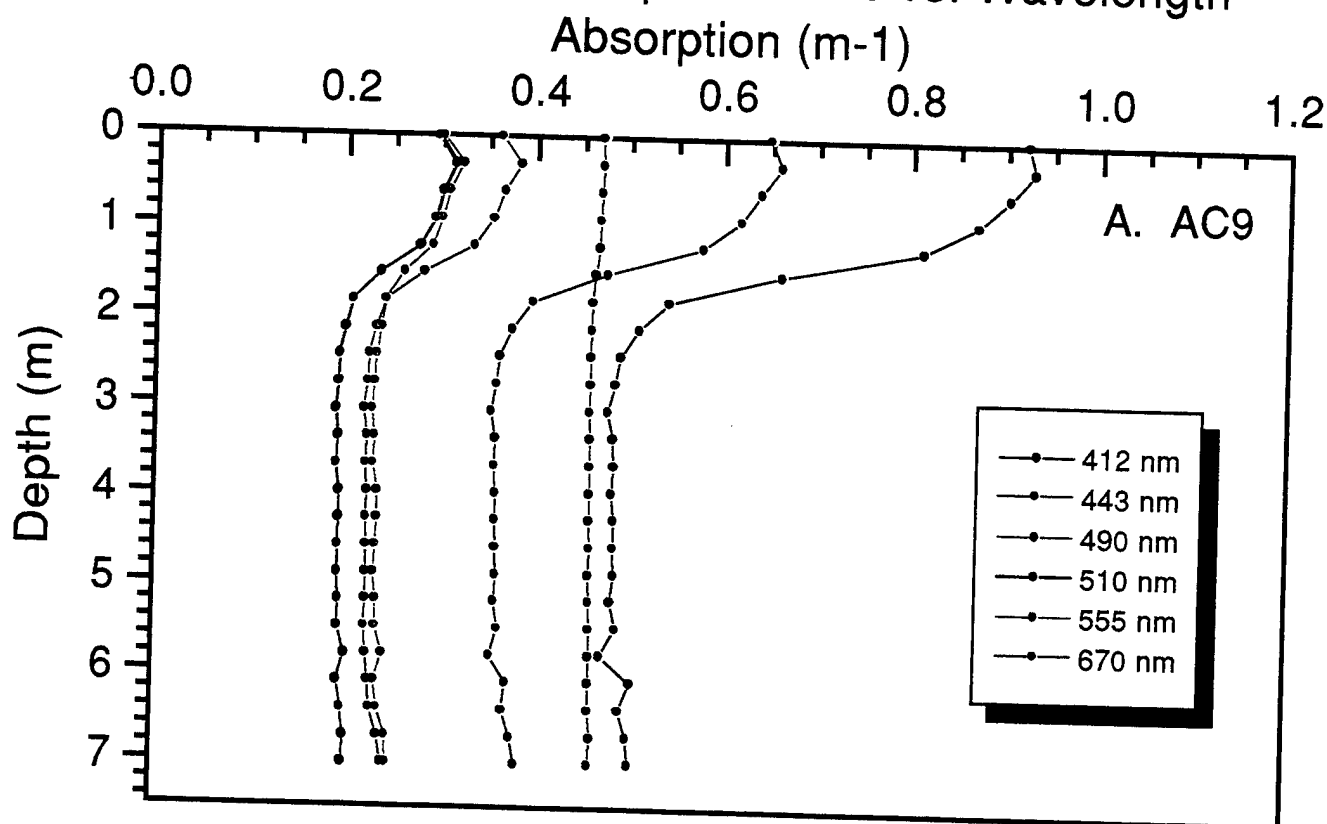


Fig. 13

Hamlet's Cove Station 1
Scattering Depth Profiles vs. Wavelength

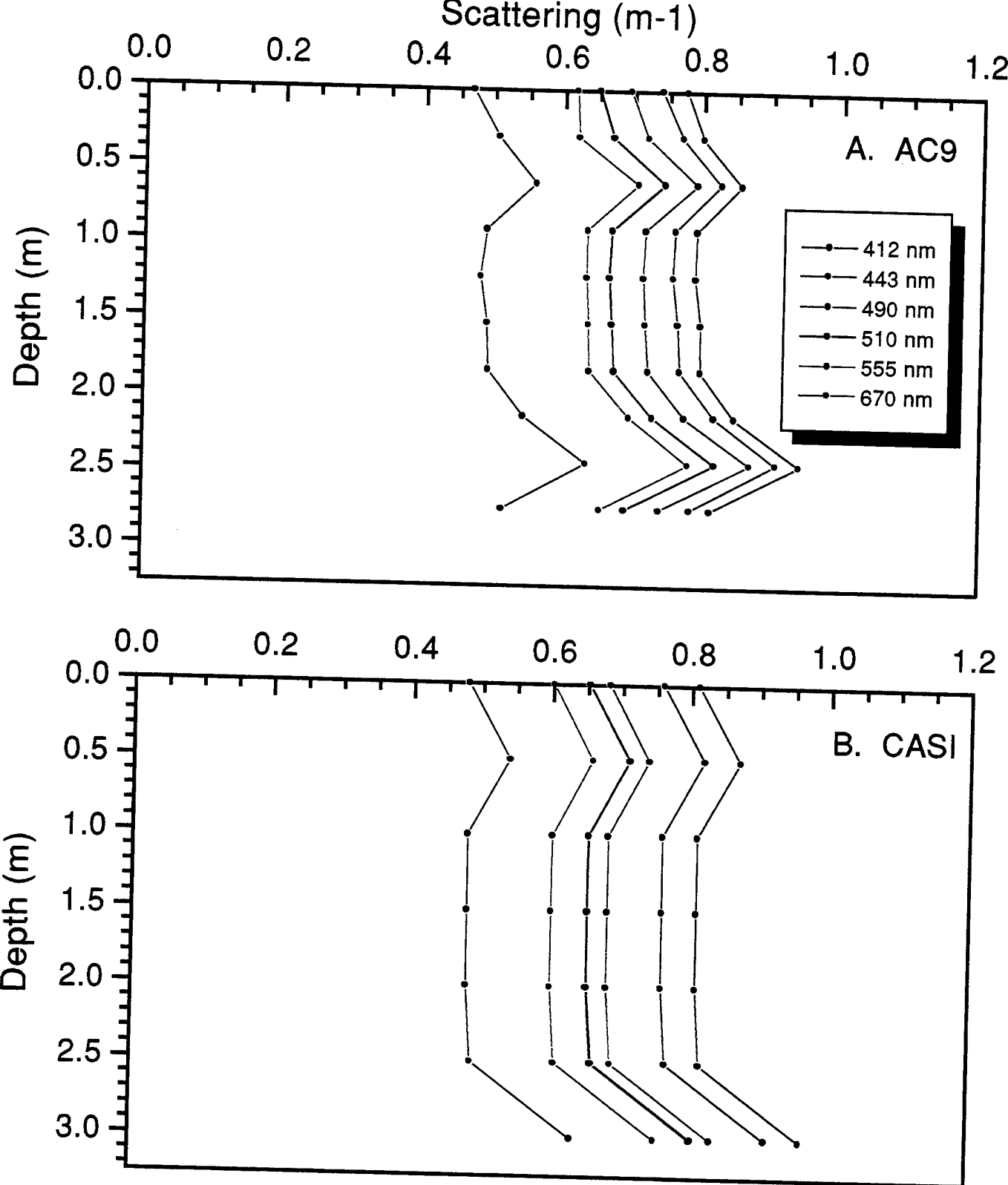


Fig. 14

Hamlet's Cove Station 2
Scattering Depth Profiles vs. Wavelength
Scattering (m⁻¹)

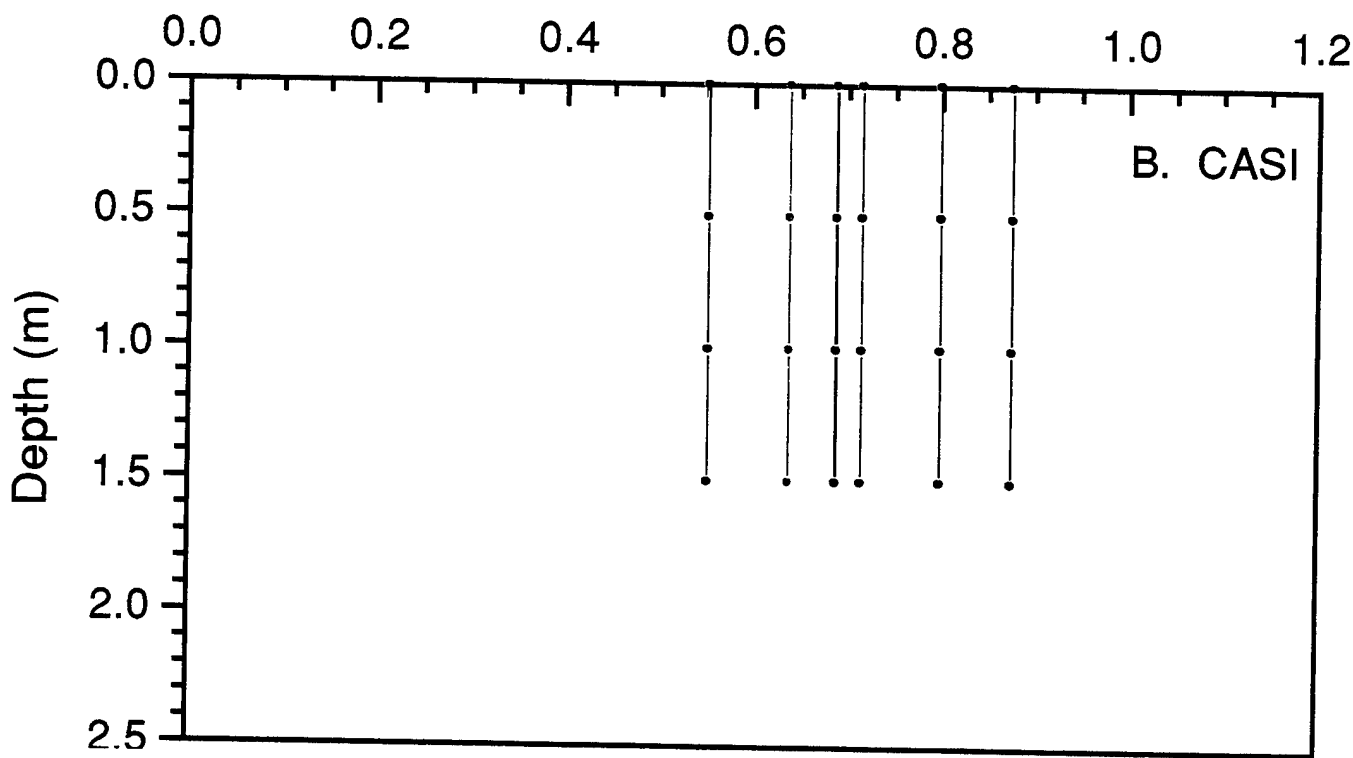
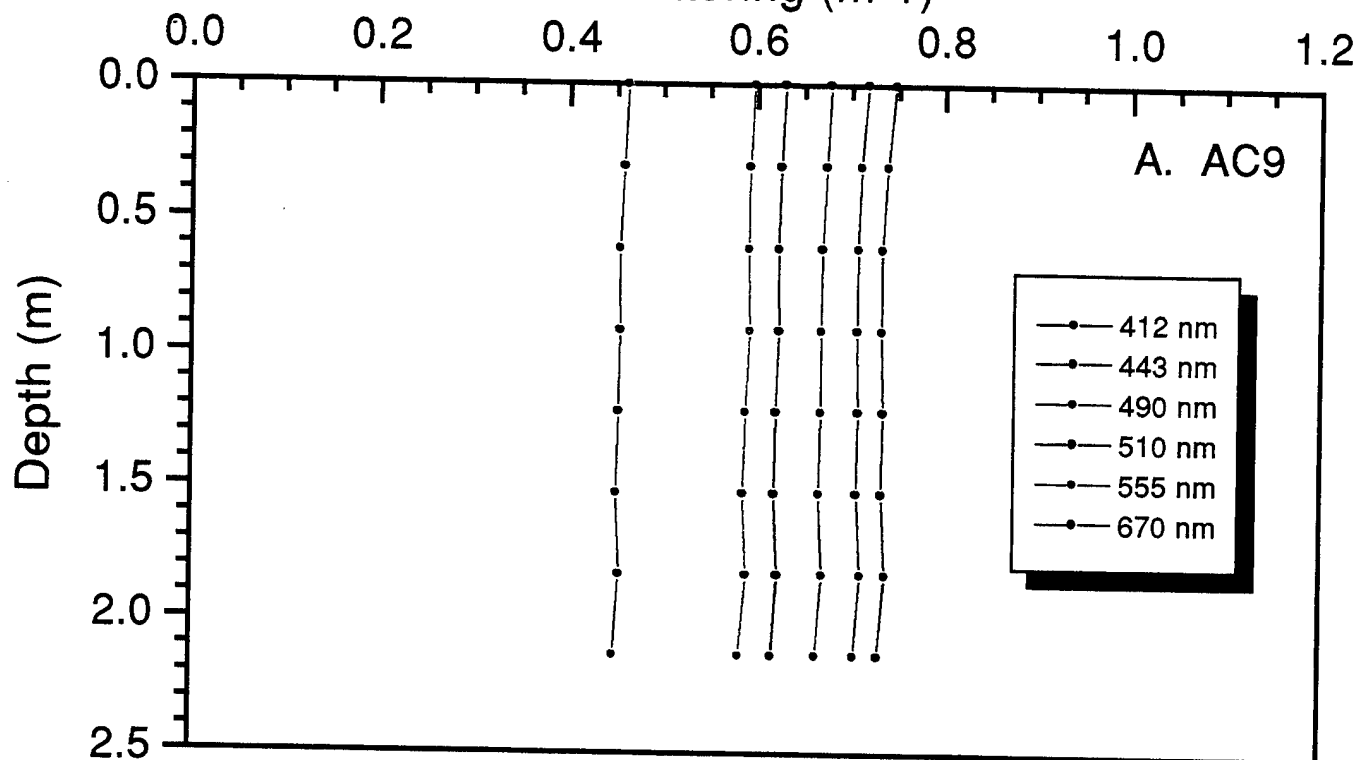


Fig. 15

Hamlet's Cove Station 3
Scattering Depth Profiles vs. Wavelength
Scattering (m-1)

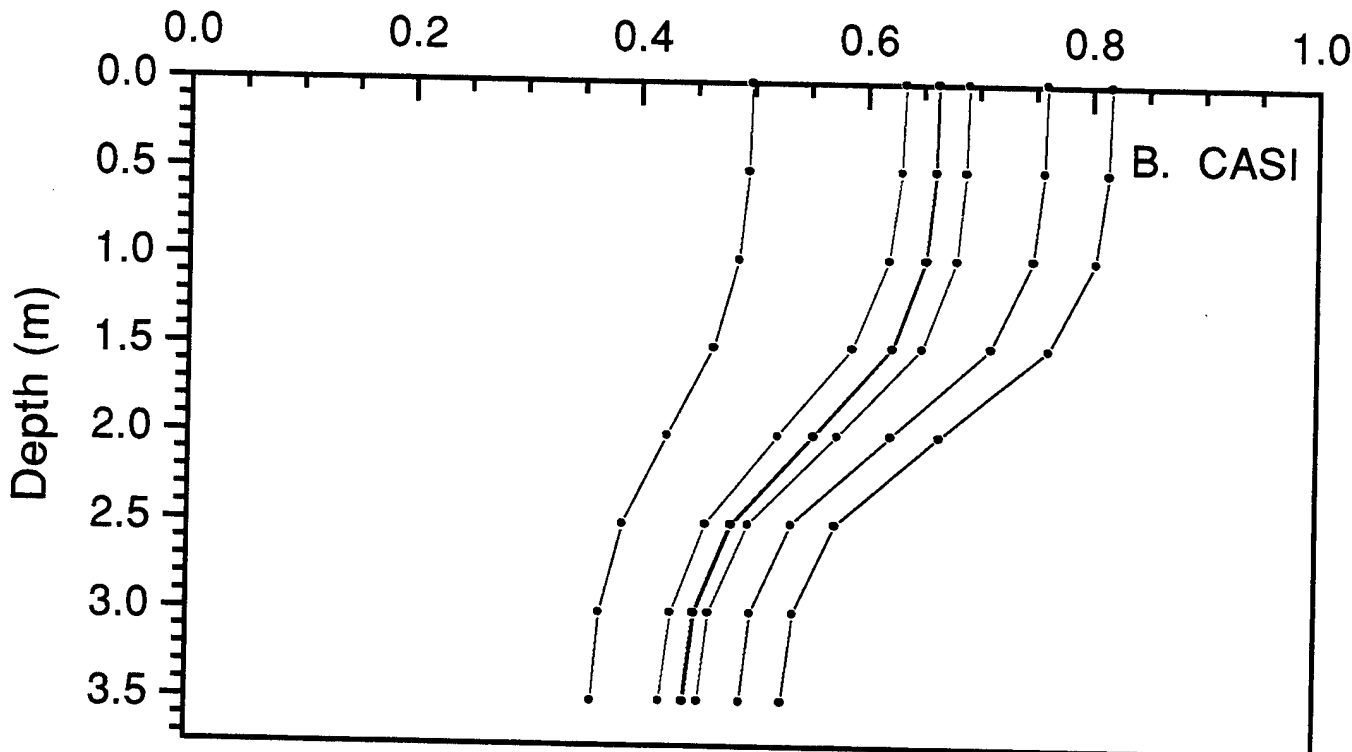
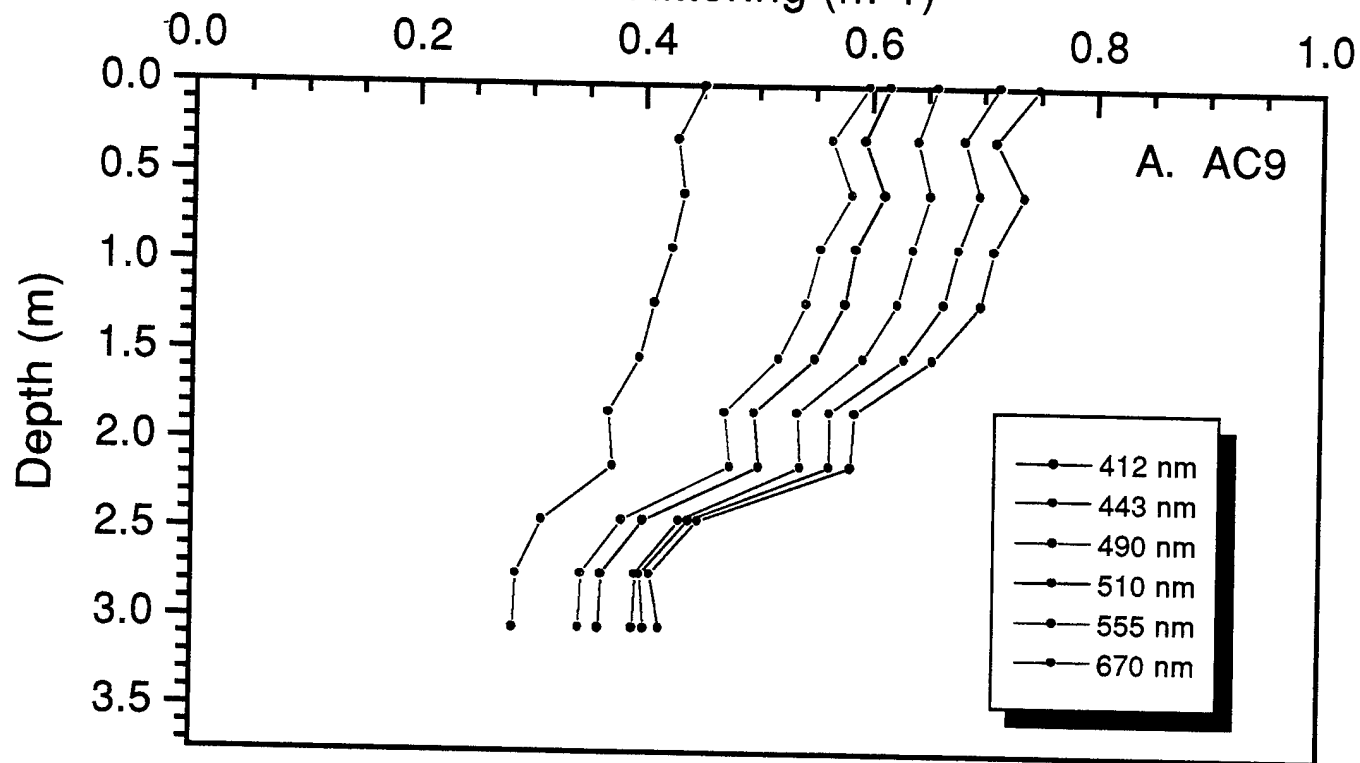


Fig. 16

Hamlet's Cove Station 4
Scattering Depth Profiles vs. Wavelength

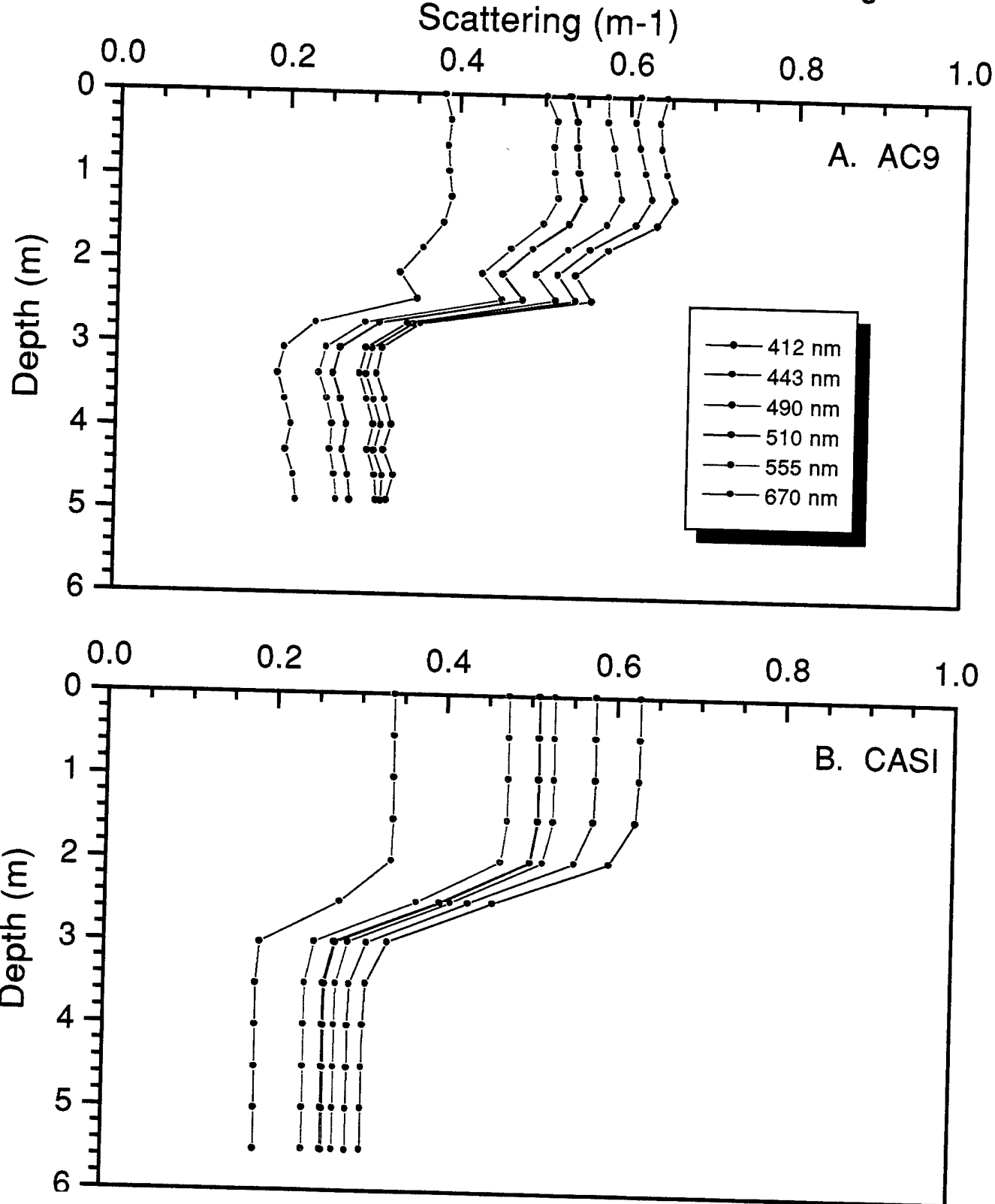


Fig. 17

Hamlet's Cove Station 5
Scattering Depth Profiles vs. Wavelength

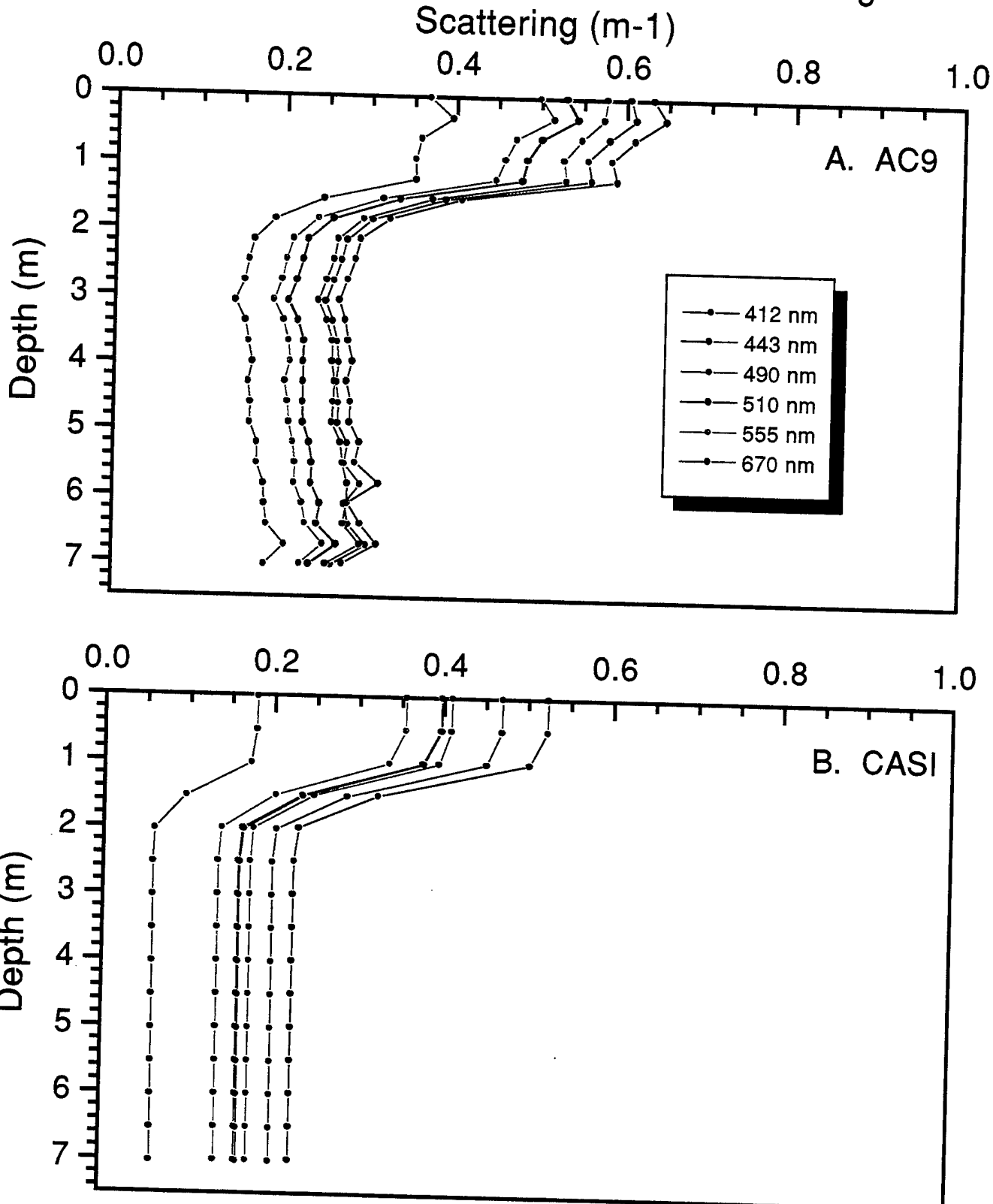


Fig. 18

Hamlet's Cove
Spectral Surface Absorption vs. Station

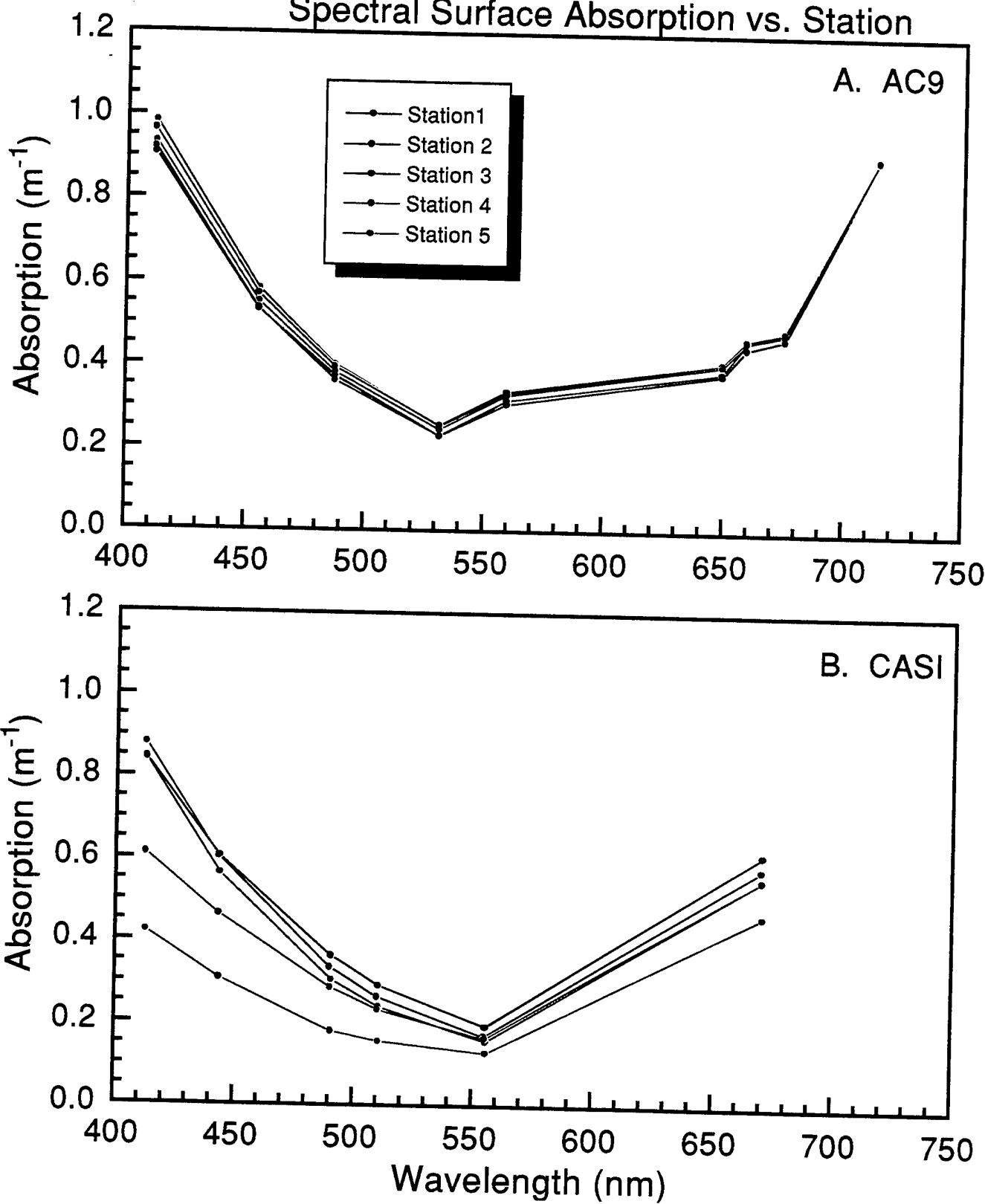


Fig. 19

Hamlet's Cove
Surface Scattering vs. Wavelength

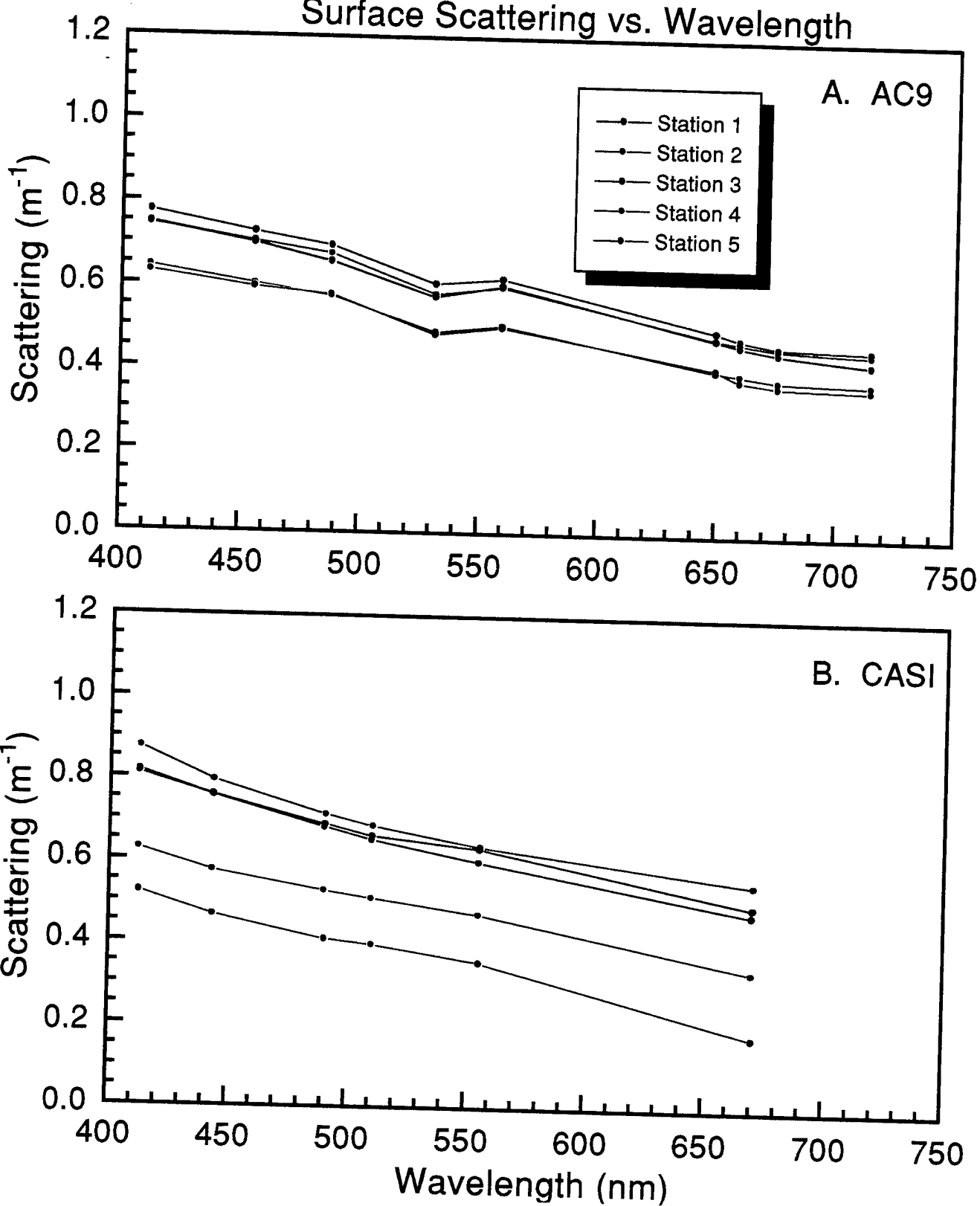


Fig. 20

Hamlet's Cove Station 1
Spectral Absorption vs. Depth

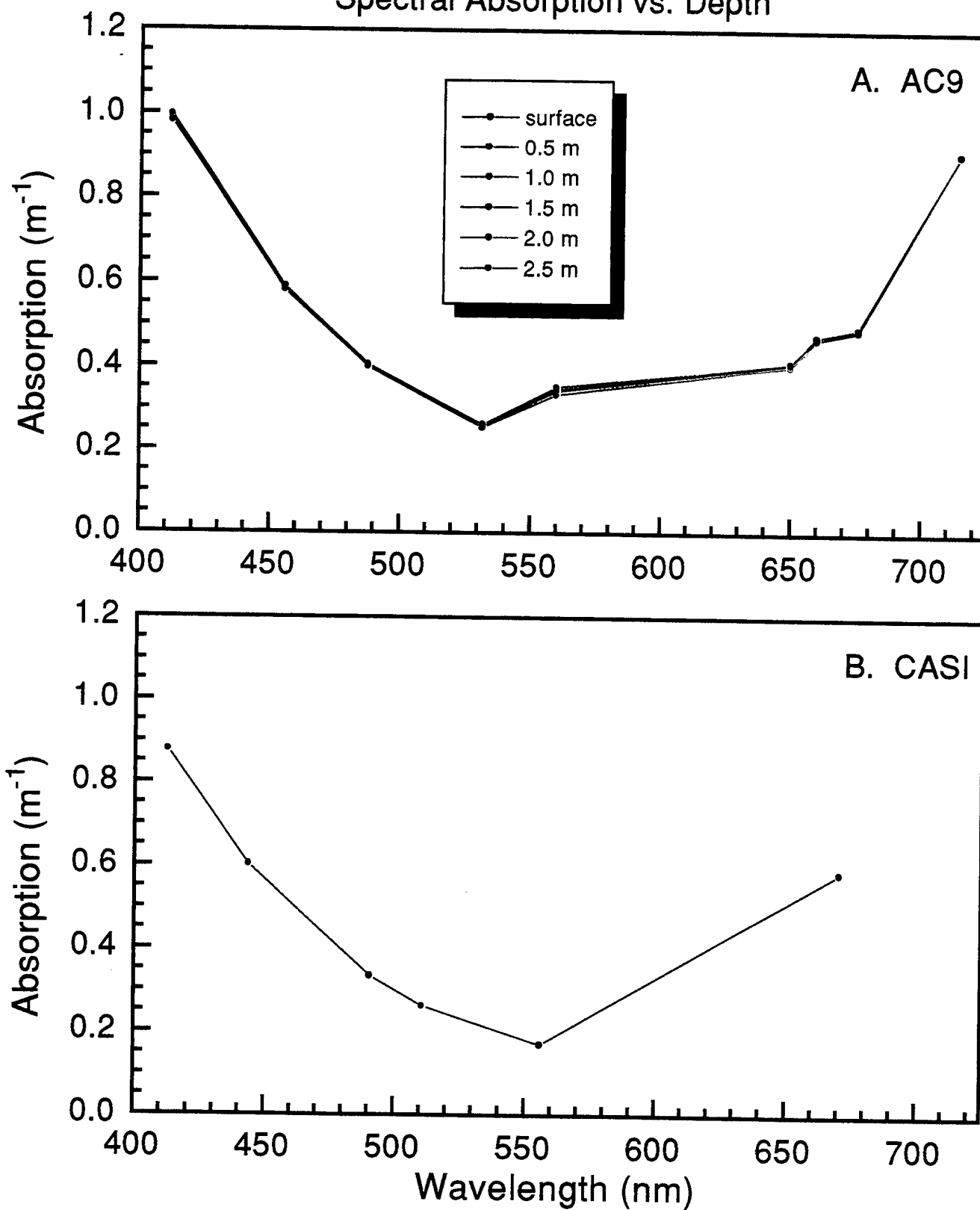


Fig. 21

Hamlet's Cove Station 2
Spectral Absorption vs. Depth

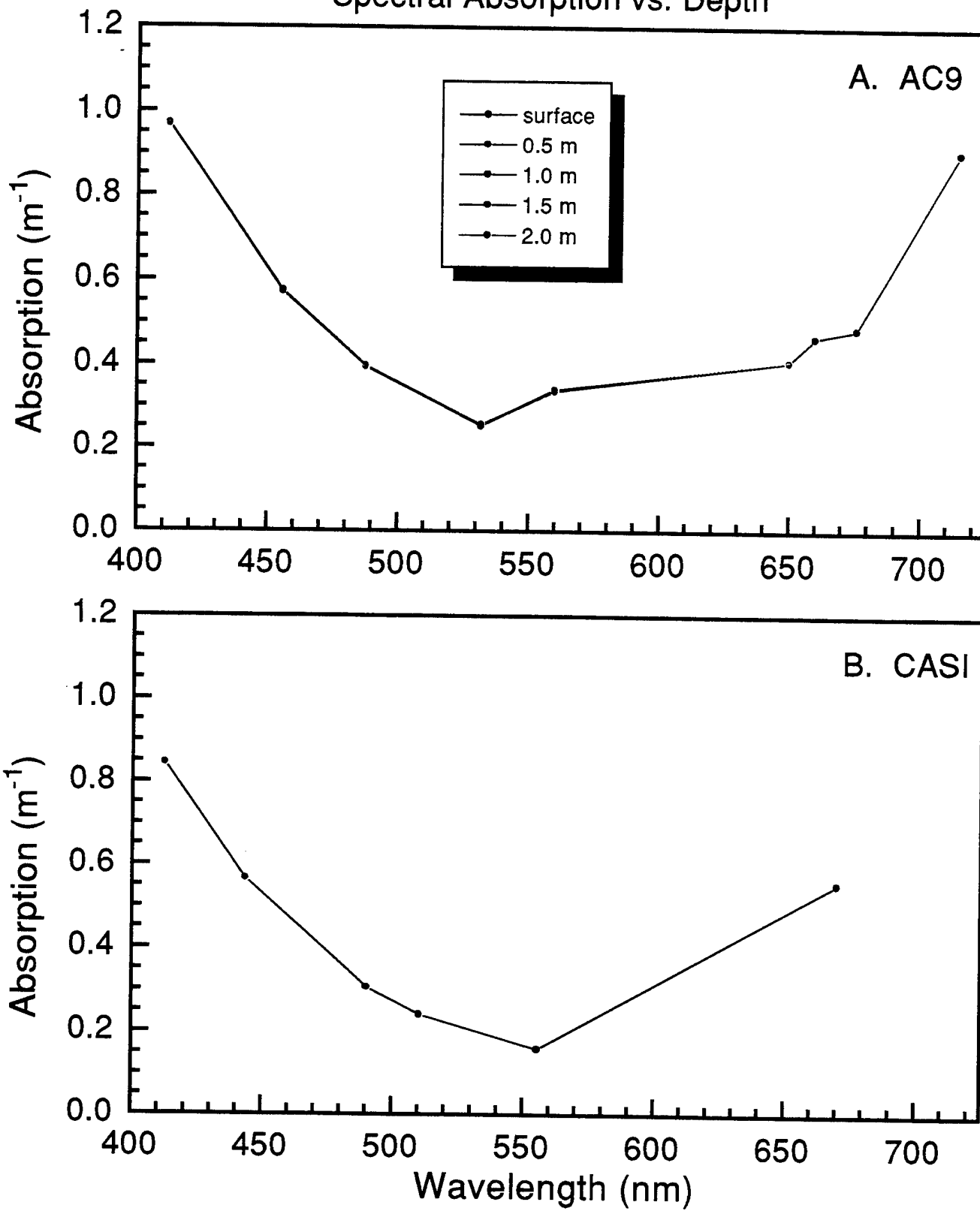


Fig. 22

Hamlet's Cove Station 3
Spectral Absorption vs. Depth

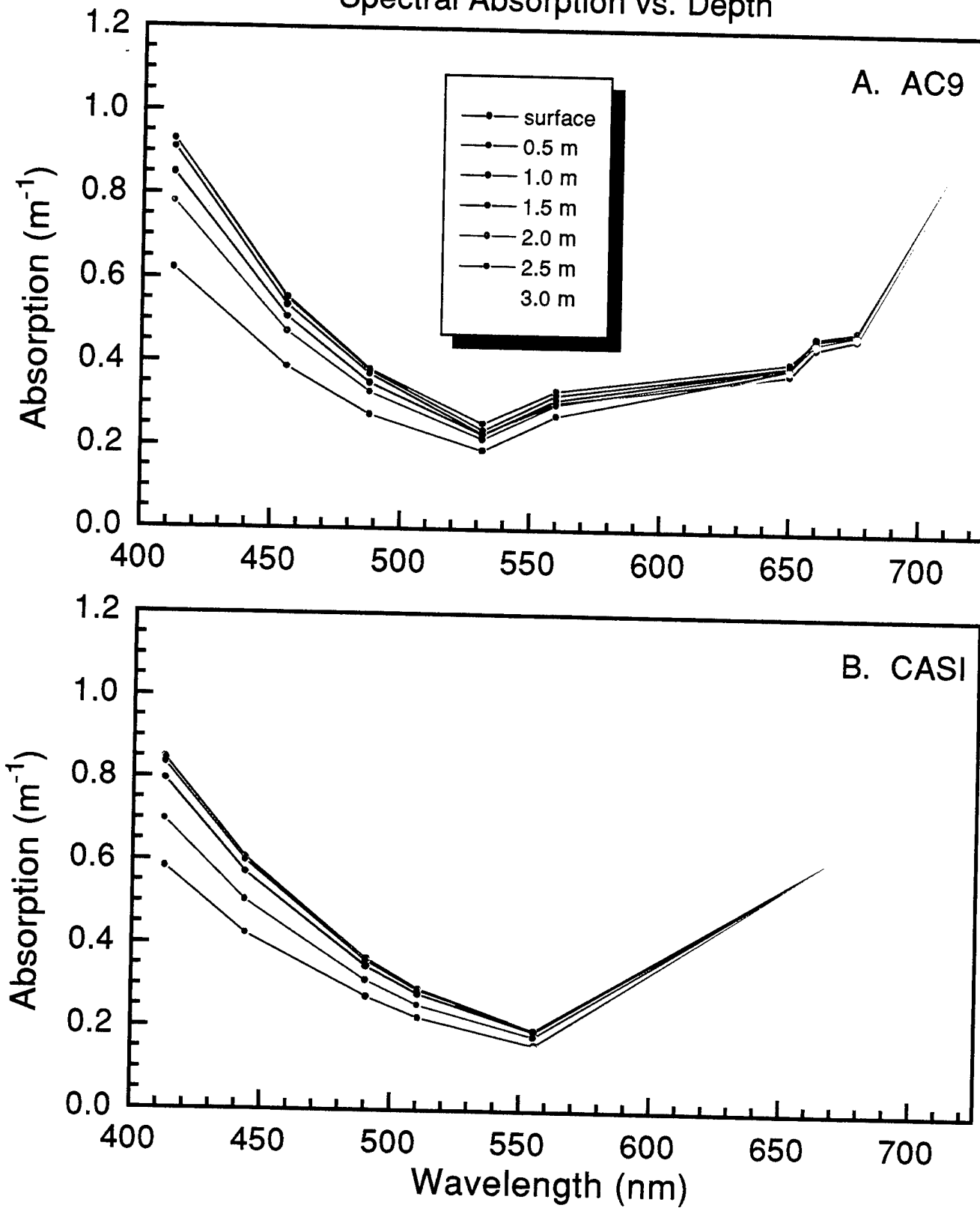


Fig. 23

Hamlet's Cove Station 4
Spectral Absorption vs. Depth

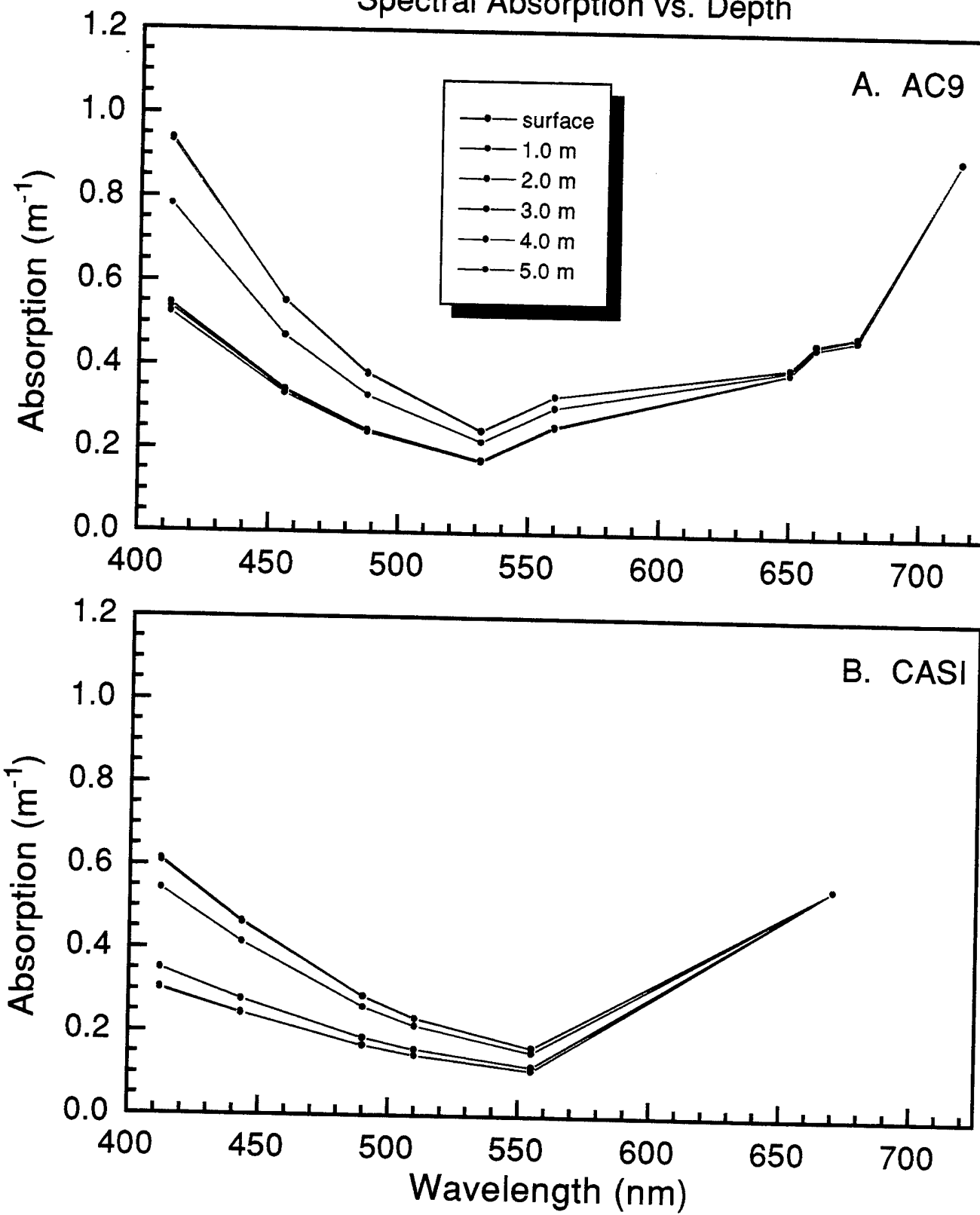


Fig. 24

Hamlet's Cove Station 5
Spectral Absorption vs. Depth

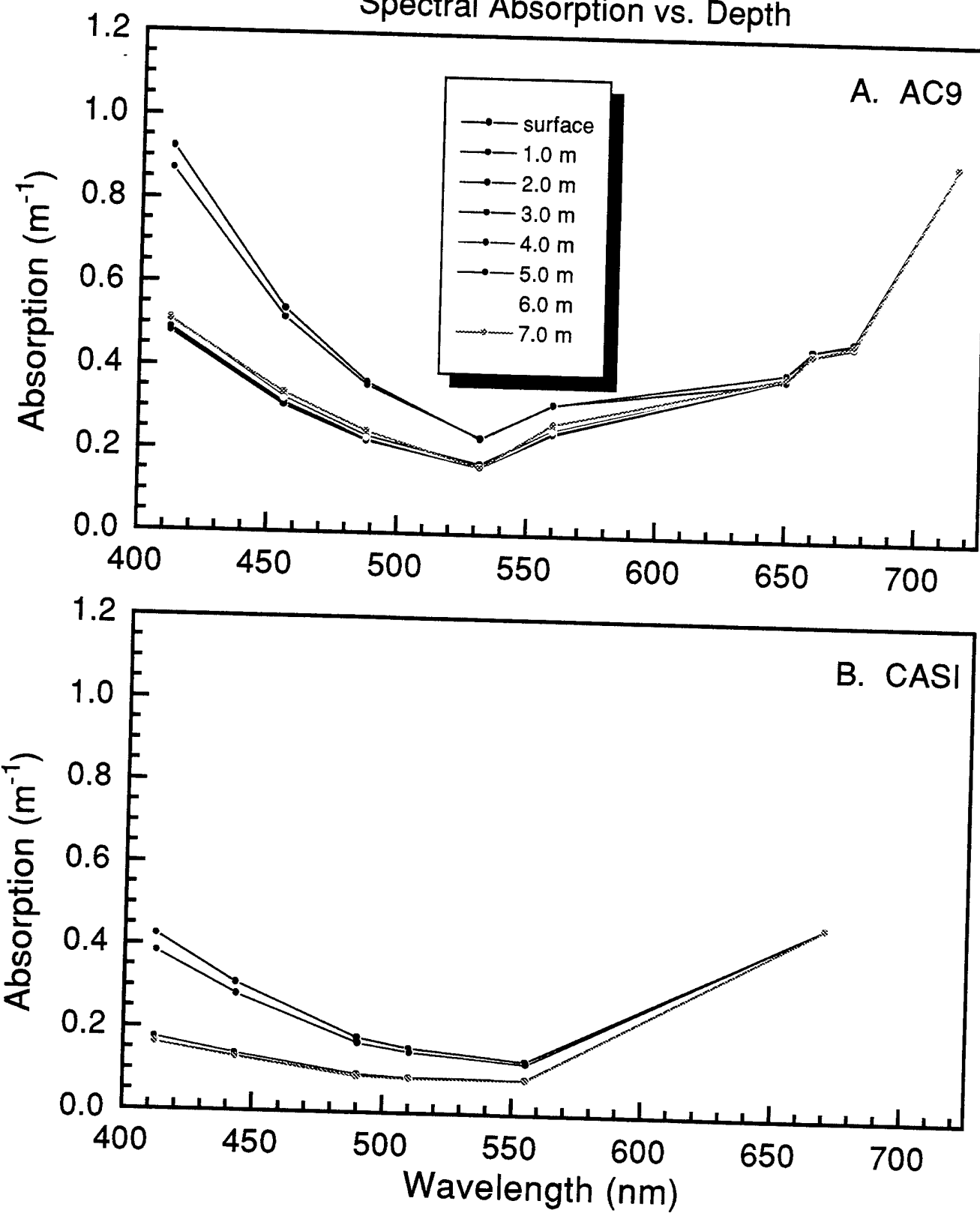


Fig. 25

Hamlet's Cove Station 1
Spectral Scattering vs. Depth

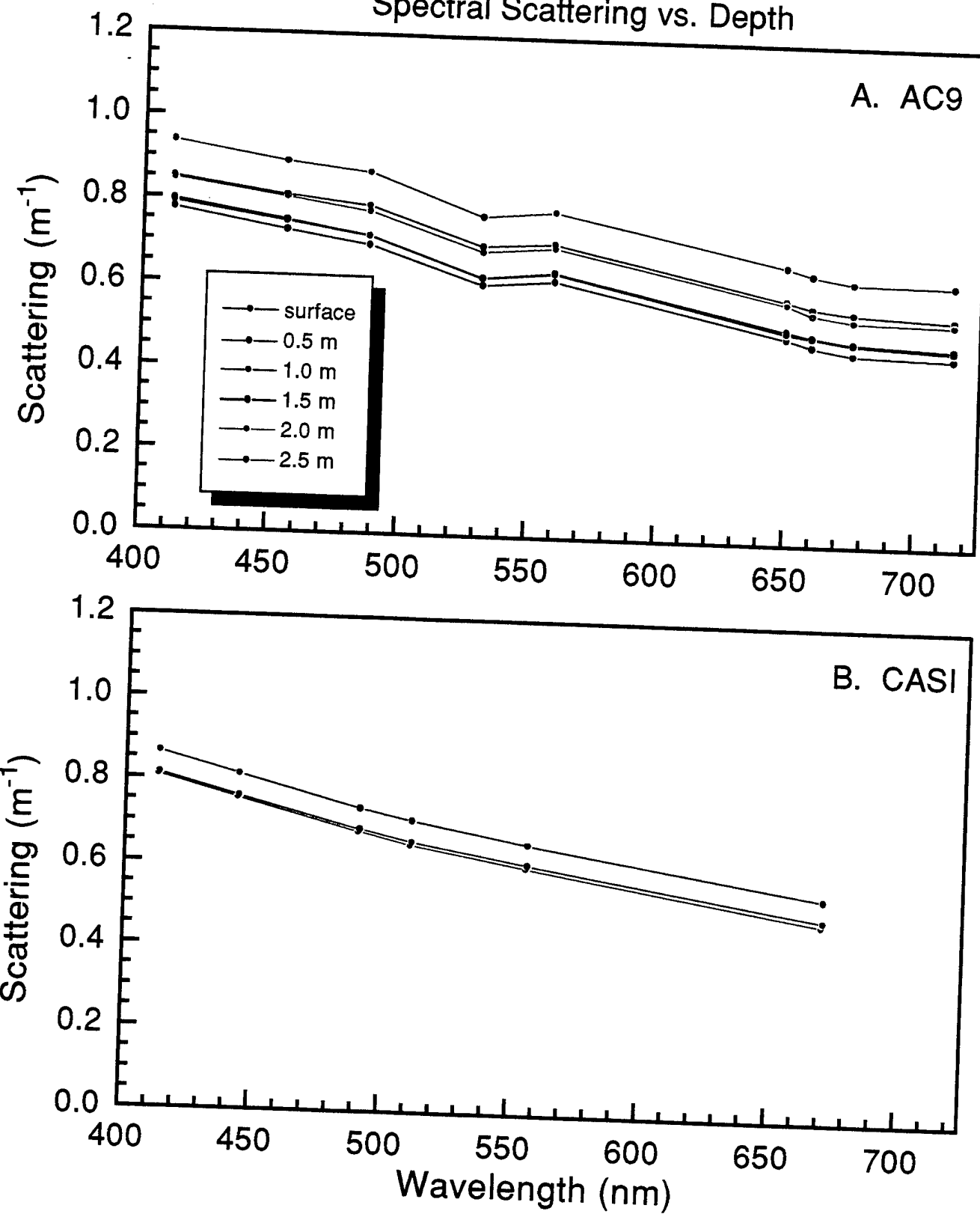


Fig. 26

Hamlet's Cove Station 2
Spectral Scattering vs. Depth

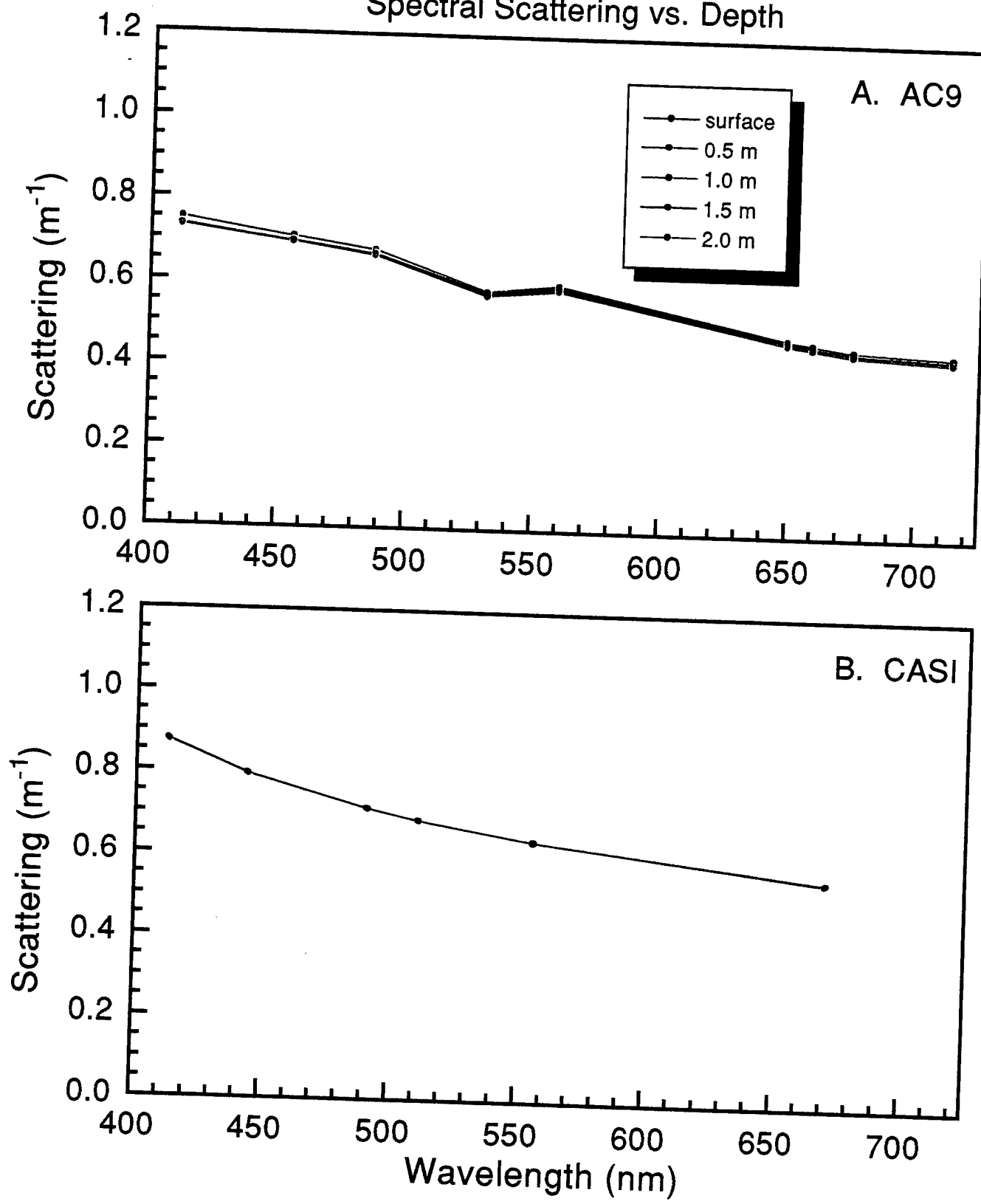


Fig. 27

Hamlet's Cove Station 3
Spectral Scattering vs. Depth

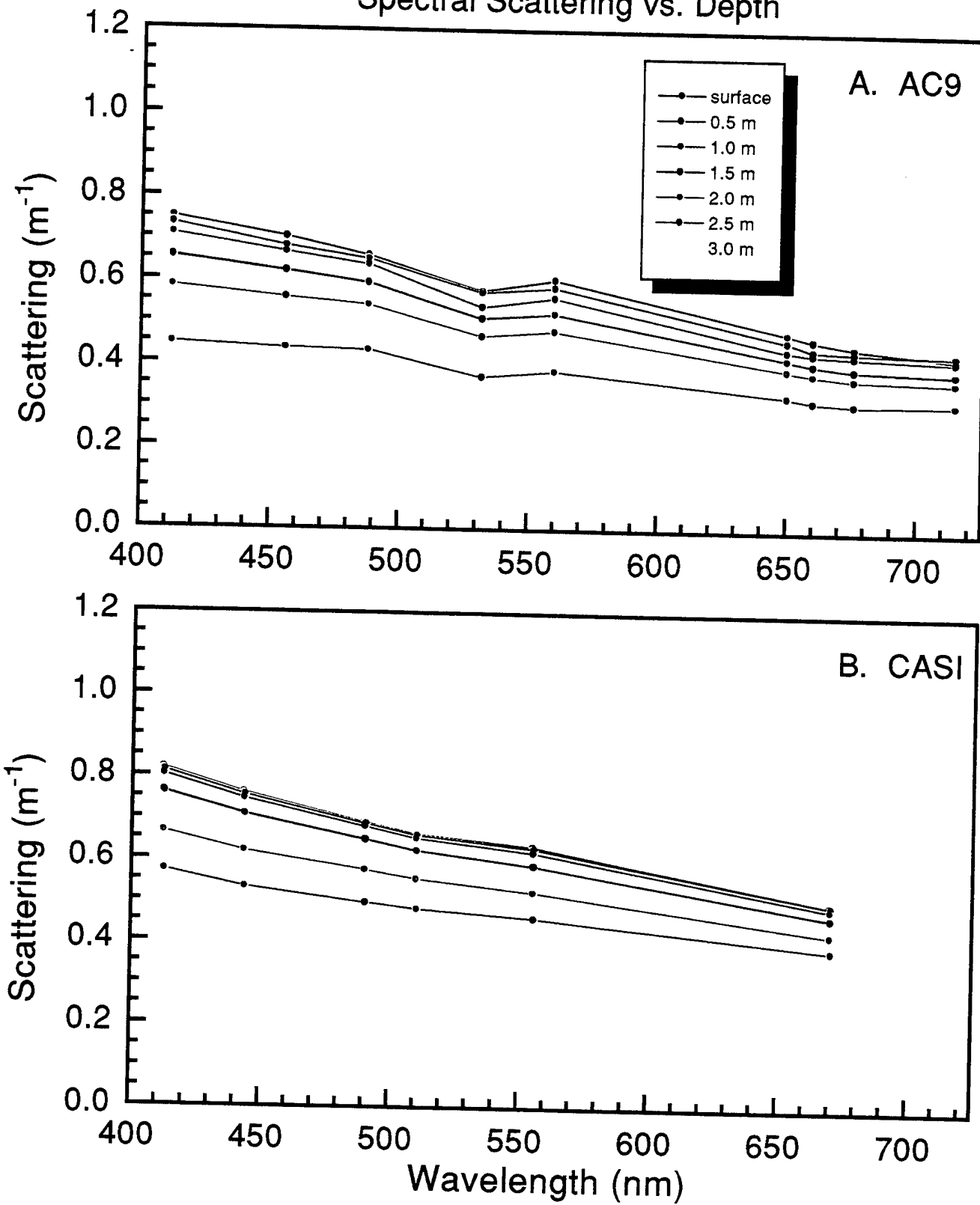


Fig. 28

Hamlet's Cove Station 4
Spectral Scattering vs. Depth

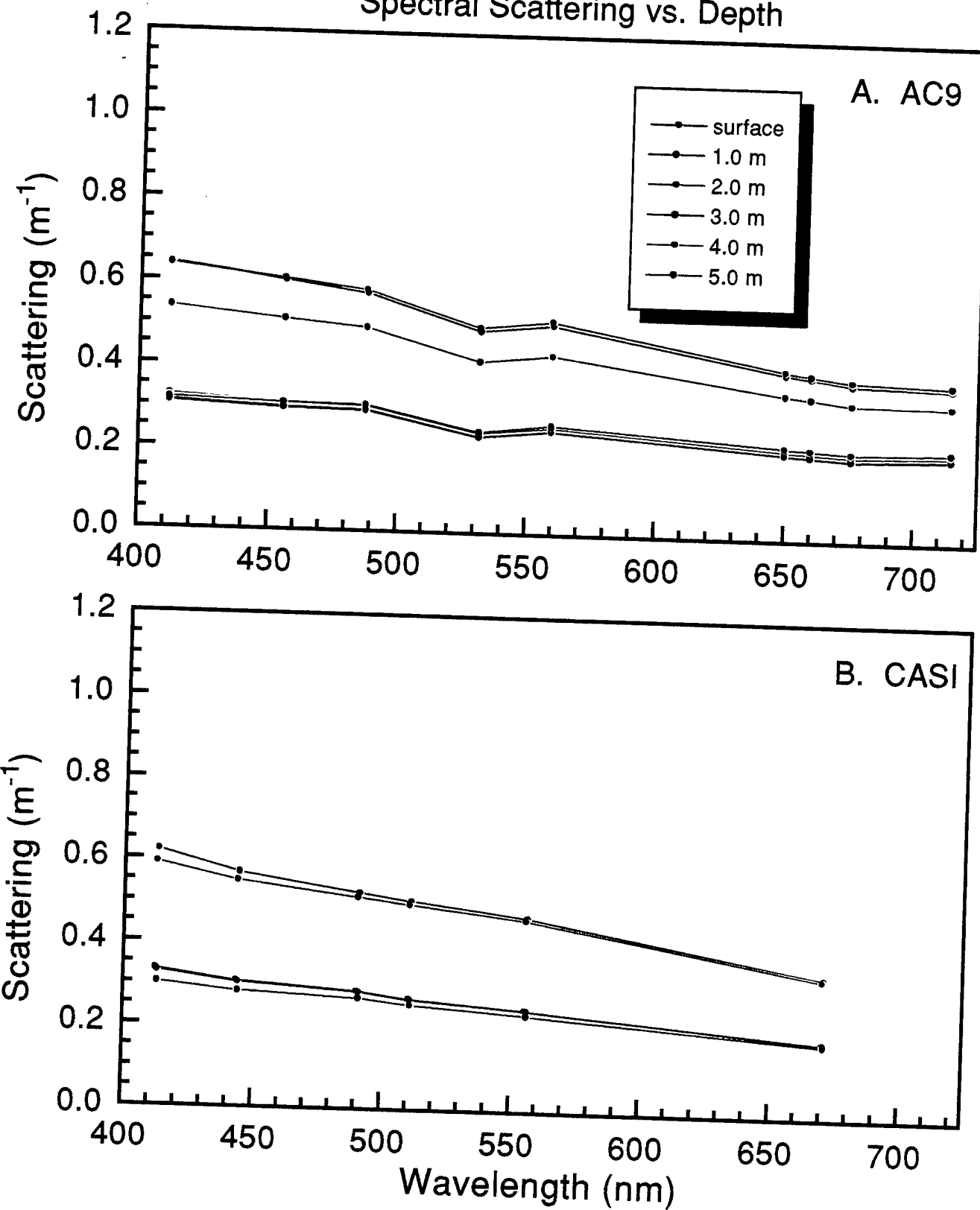


Fig. 29

Hamlet's Cove Station 5
Spectral Scattering vs. Depth

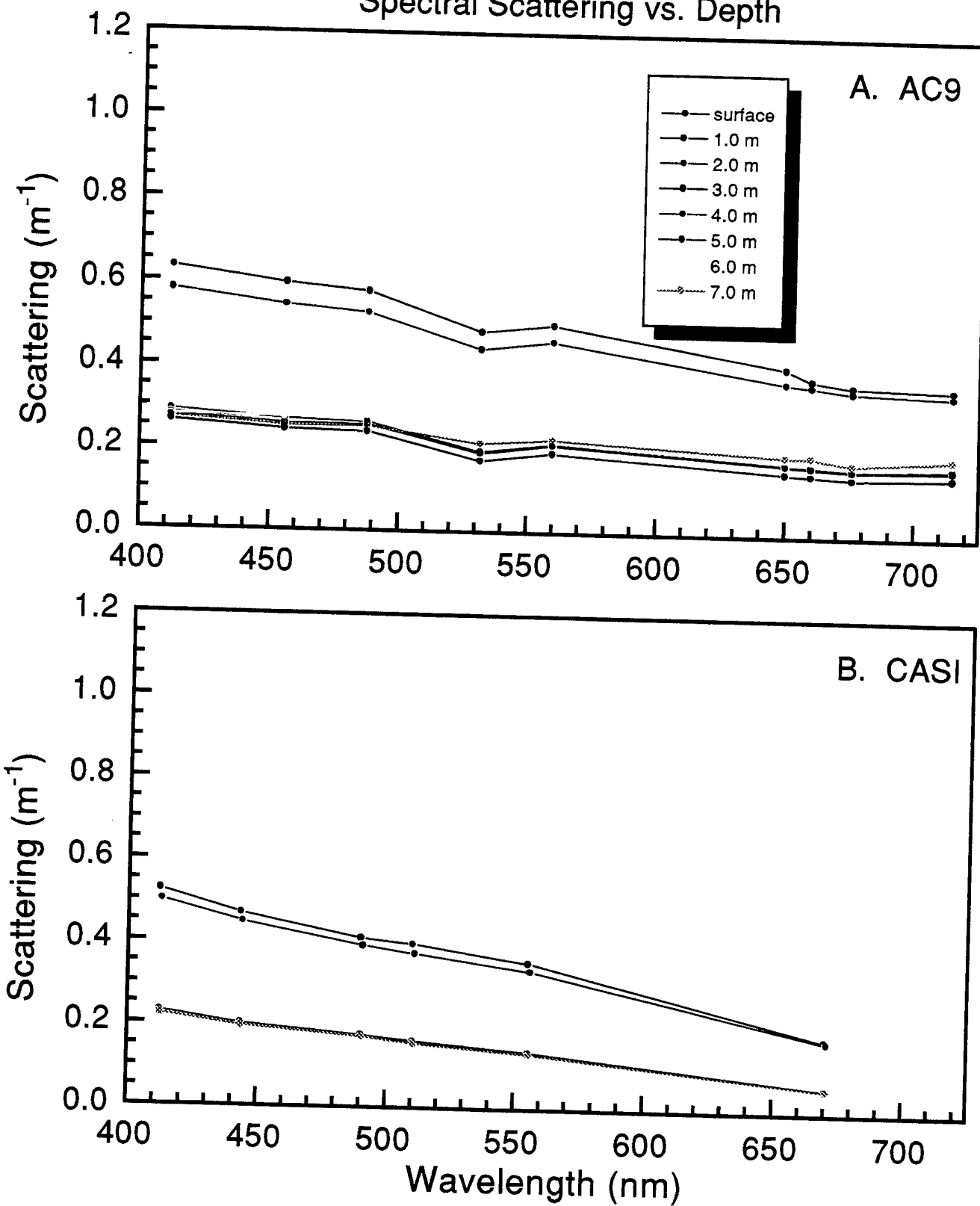


Fig. 30

AC9 Measured vs. CASI Modeled Absorption All Depths and Stations

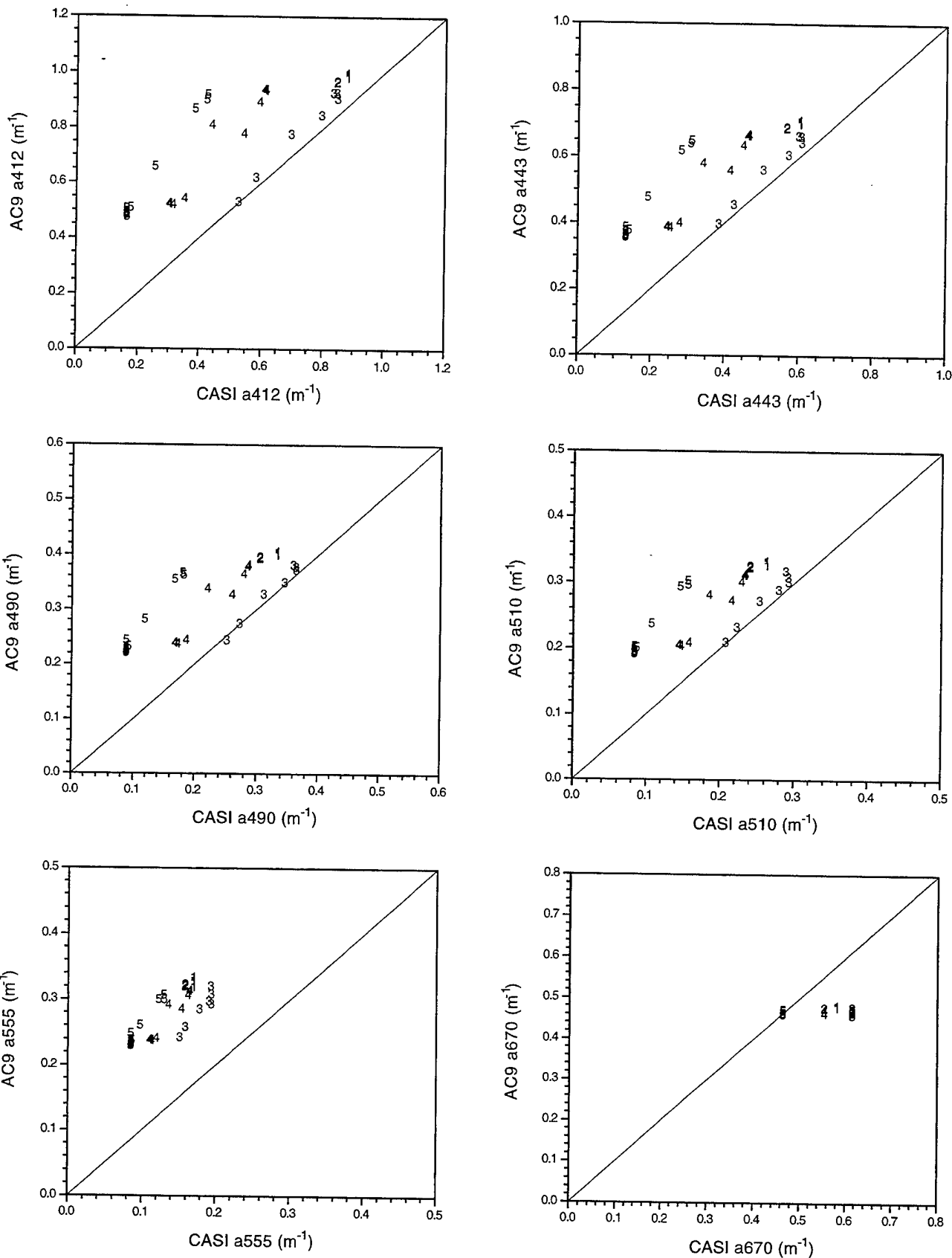


Fig. 31

AC9 Measured vs. CASI Modeled Scattering All Depths and Stations

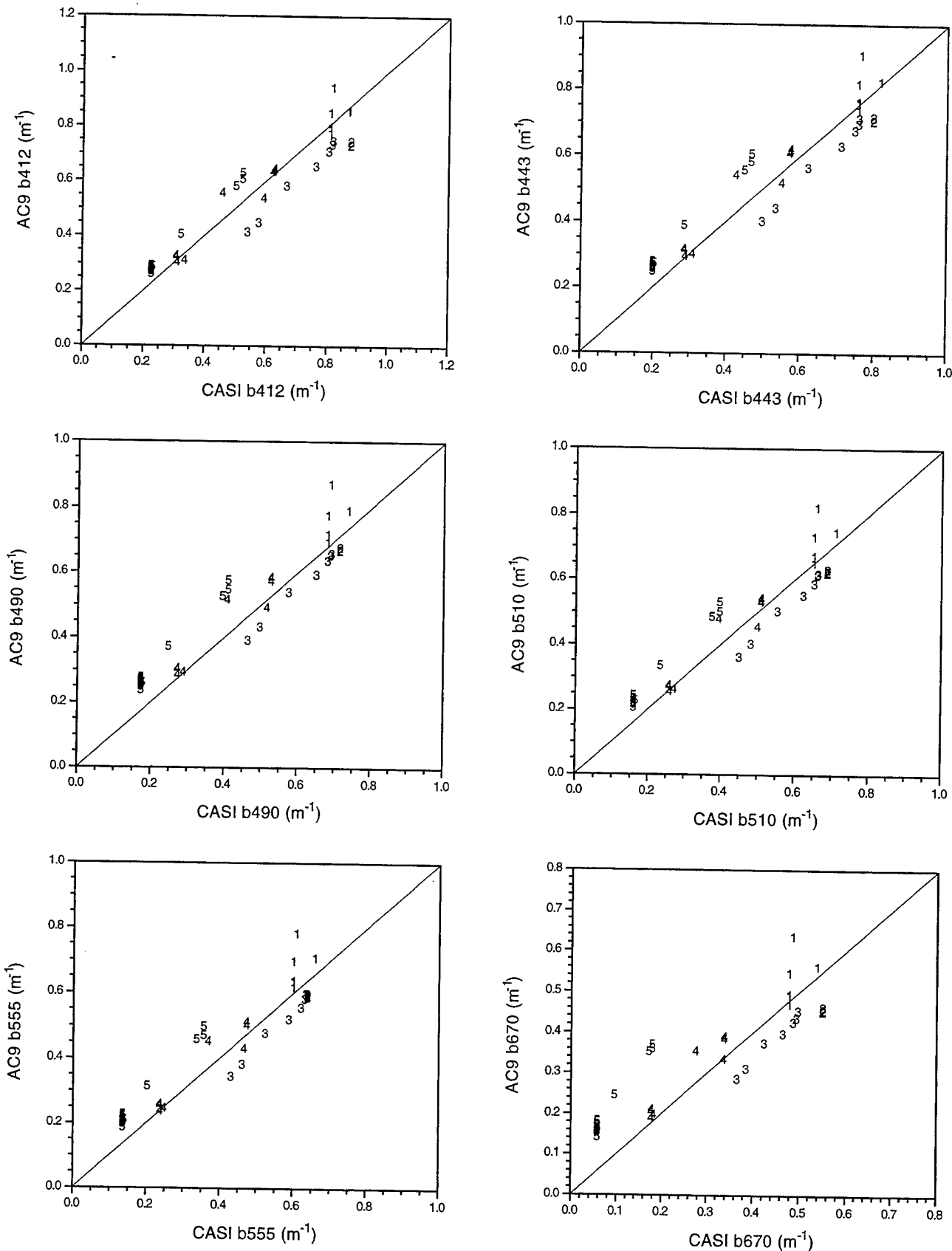


Fig. 32

Absorption at 412 nm (m^{-1})

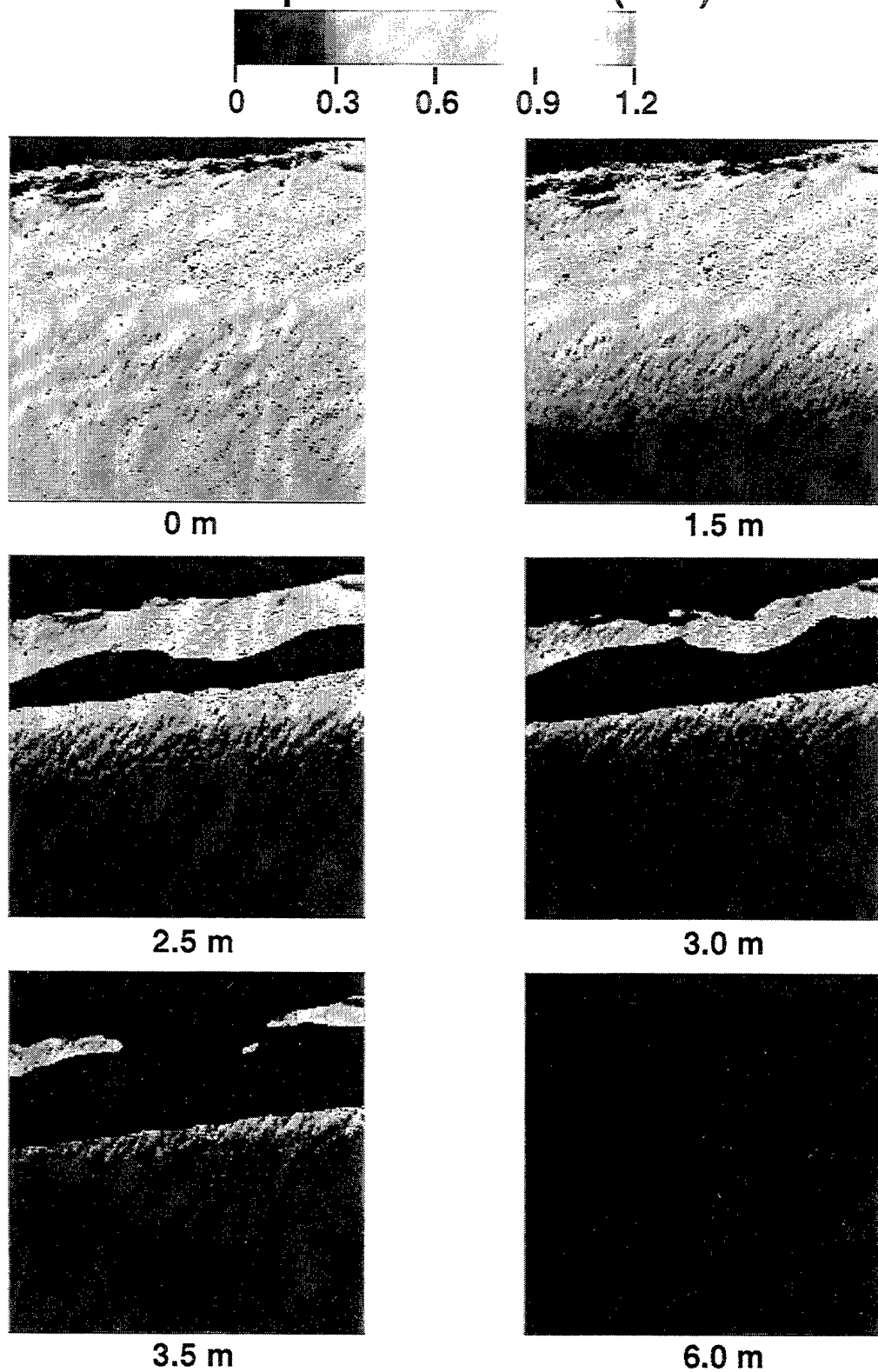
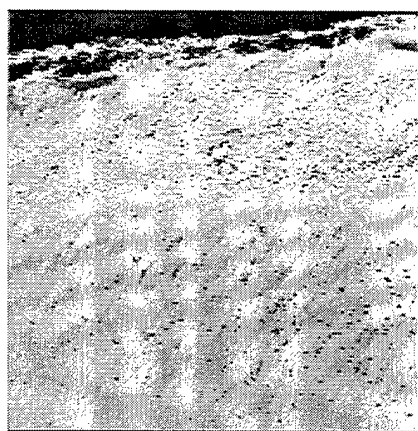
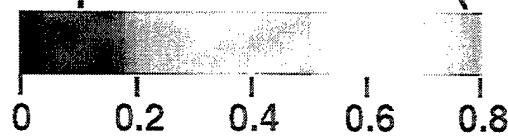
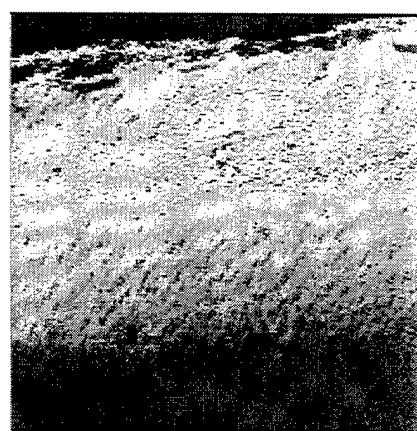


Fig. 33

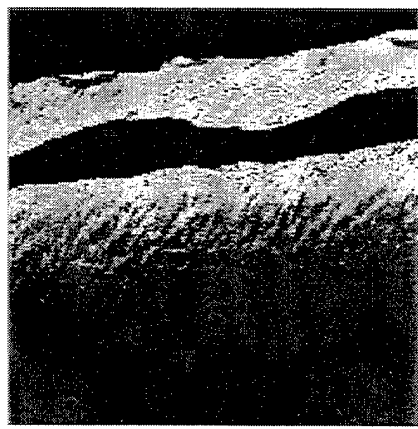
Absorption at 443 nm (m^{-1})



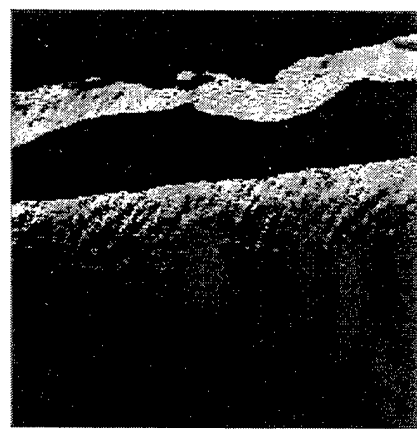
0 m



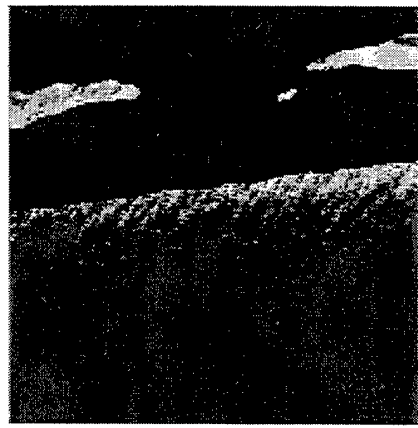
1.5 m



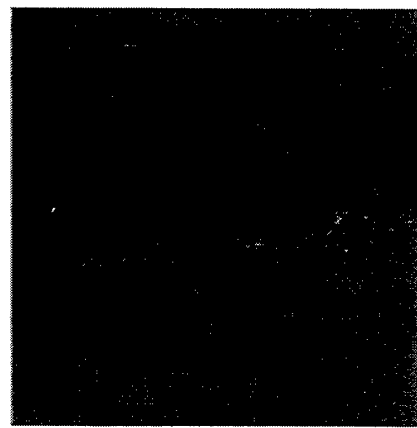
2.5 m



3.0 m



3.5 m



6.0 m

Fig. 34

Absorption at 490 nm (m^{-1})

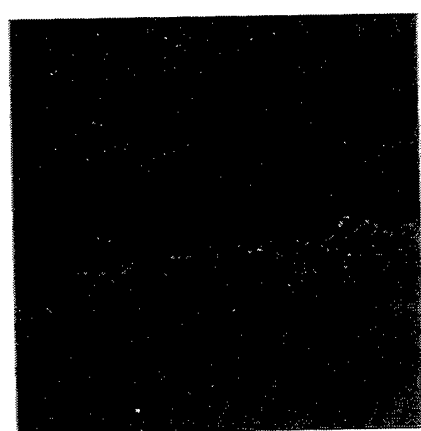
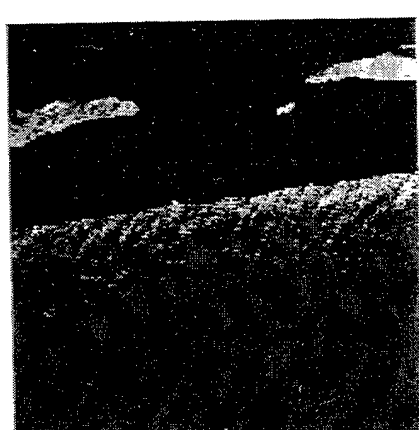
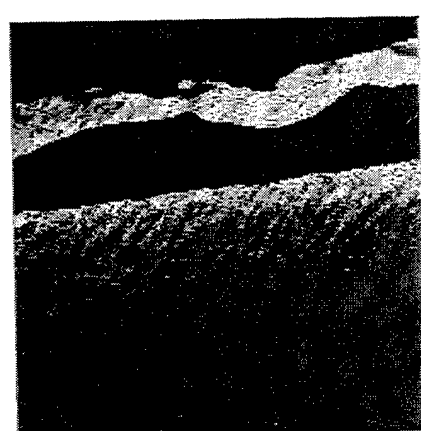
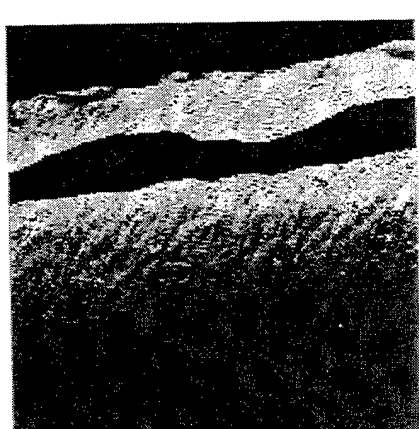
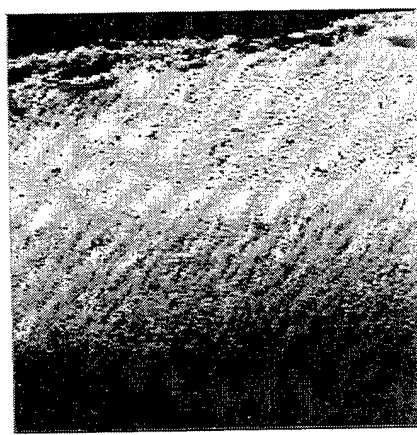
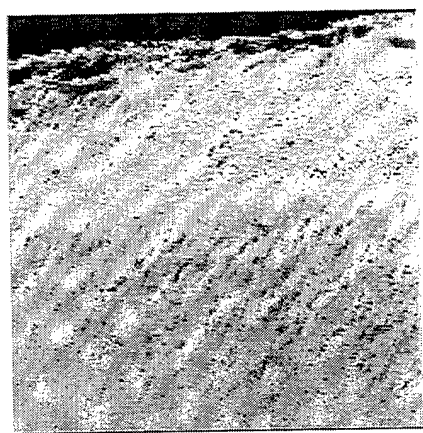
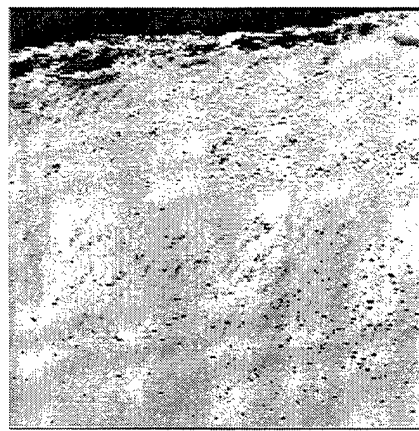
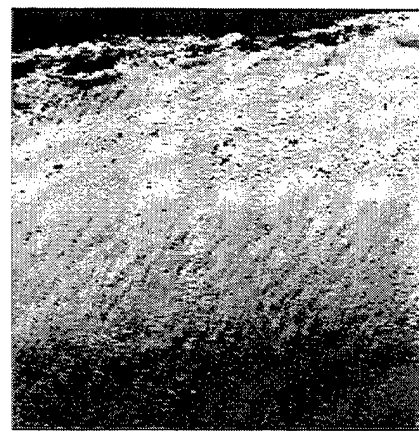


Fig. 35

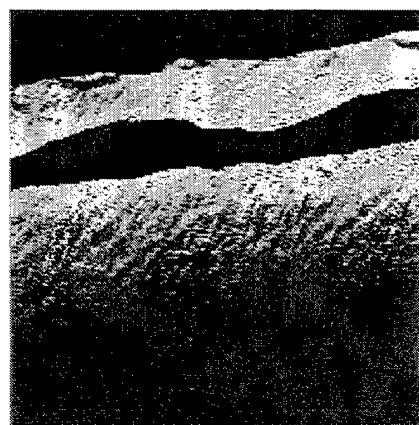
Absorption at 510 nm (m^{-1})



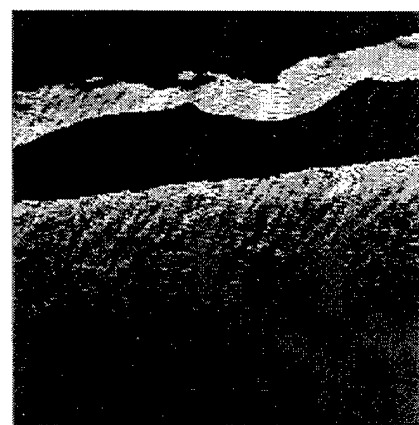
0 m



1.5 m



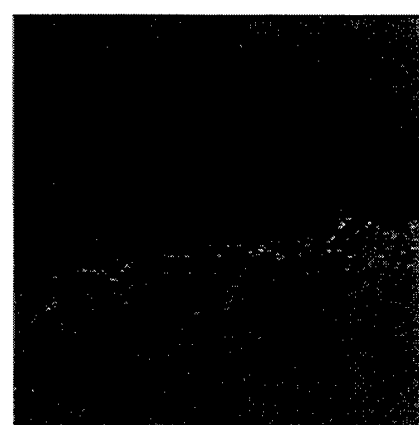
2.5 m



3.0 m



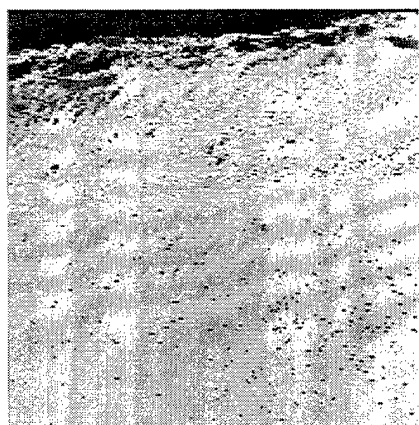
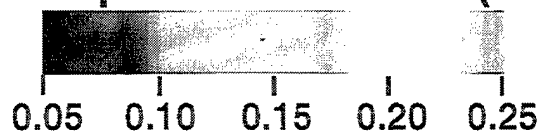
3.5 m



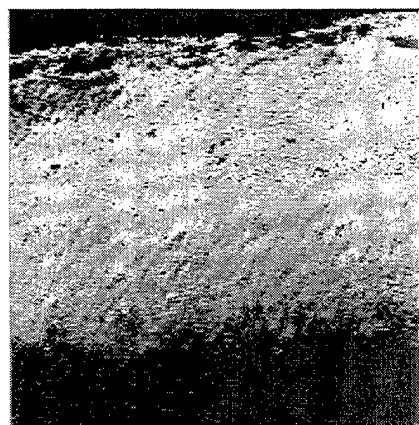
6.0 m

Fig. 36

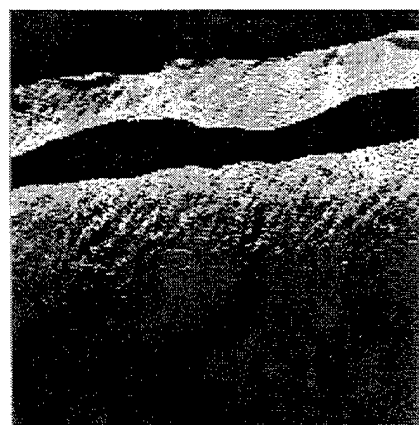
Absorption at 555 nm (m^{-1})



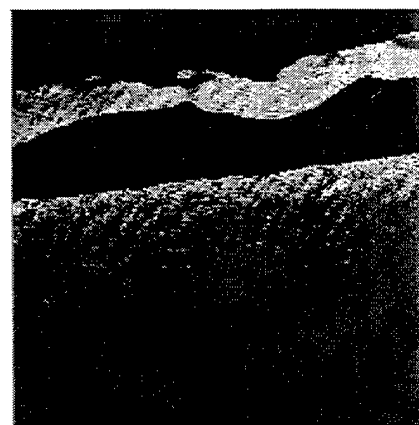
0 m



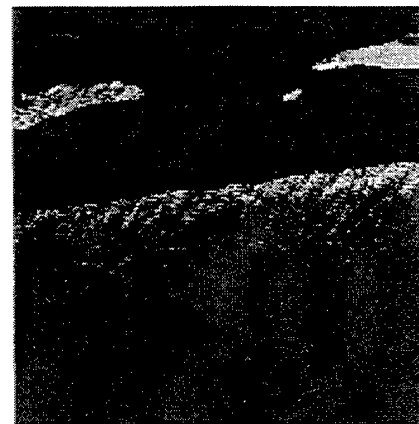
1.5 m



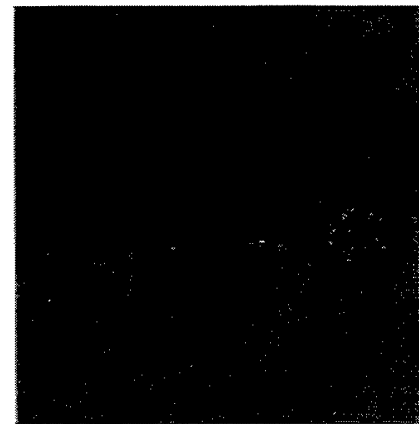
2.5 m



3.0 m



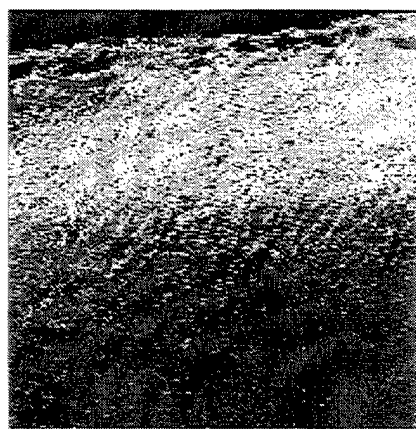
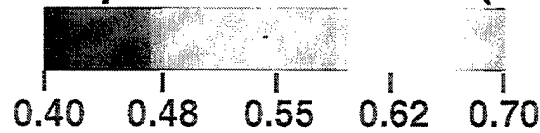
3.5 m



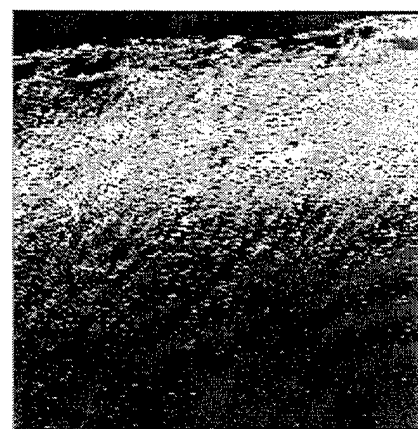
6.0 m

Fig. 37

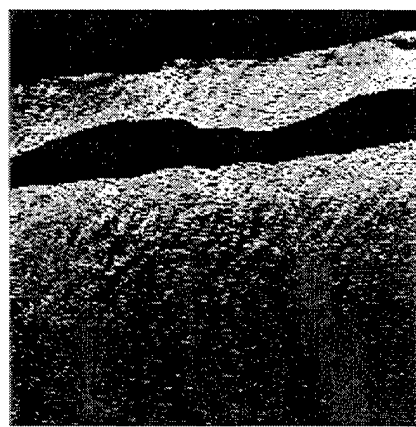
Absorption at 670 nm (m^{-1})



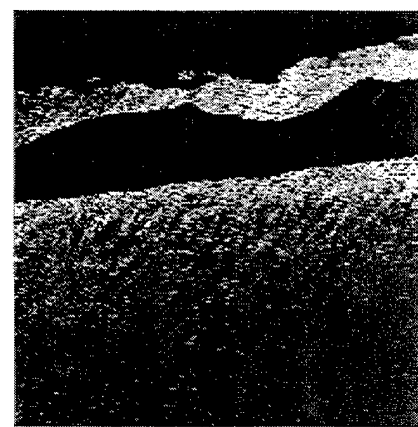
0 m



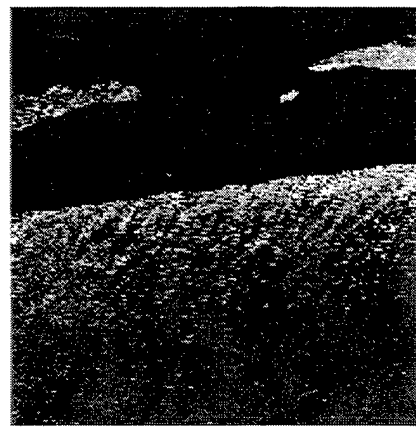
1.5 m



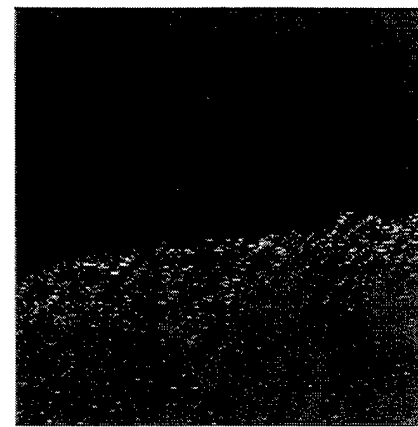
2.5 m



3.0 m



3.5 m



6.0 m

Fig. 38

Scattering at 412 nm (m^{-1})

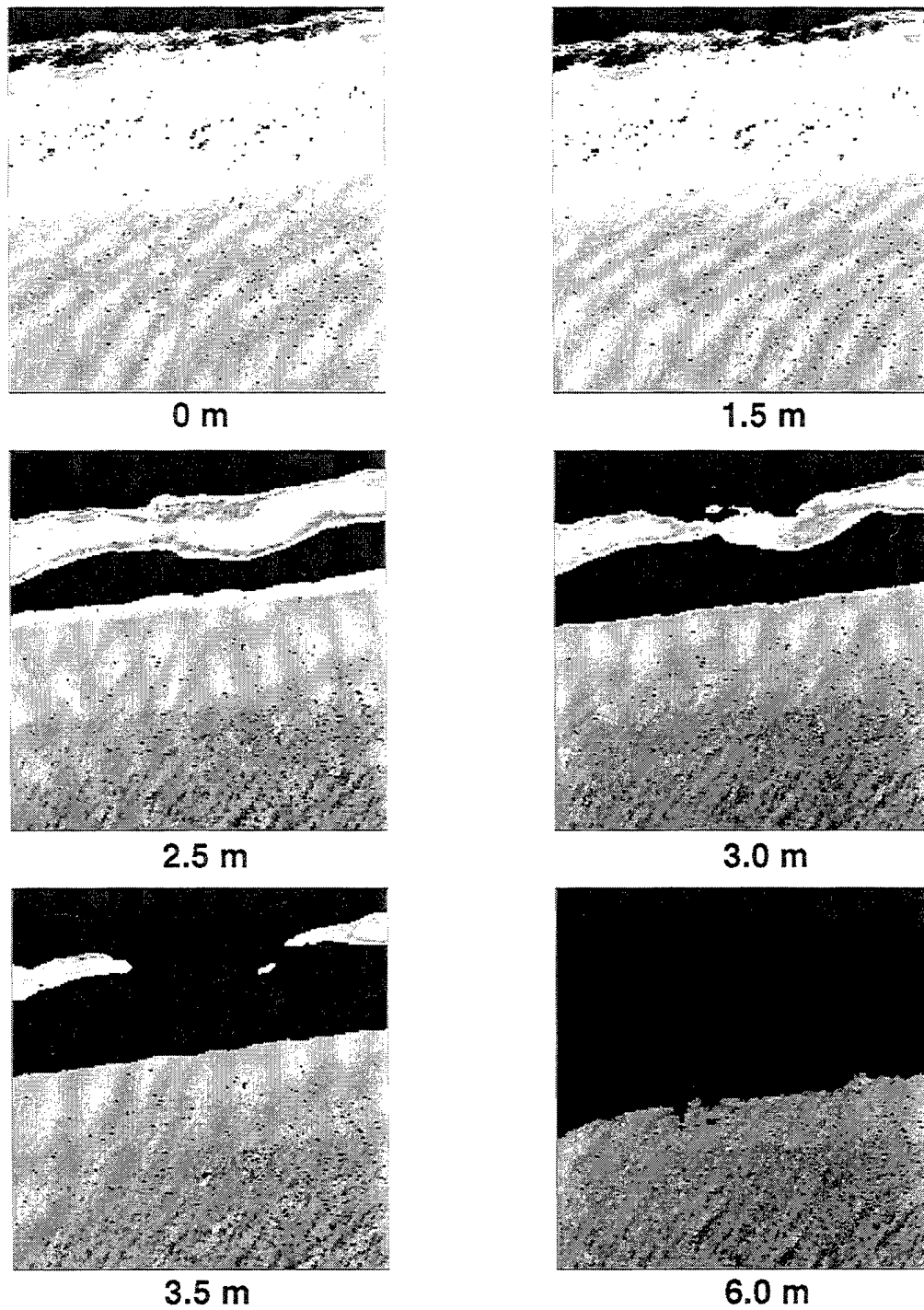
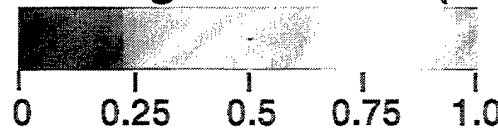


Fig. 39

Scattering at 443 nm (m^{-1})



0 m



1.5 m



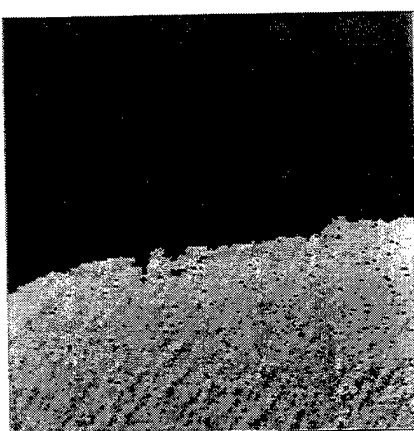
2.5 m



3.0 m



3.5 m



6.0 m

Fig. 40

Scattering at 490 nm (m^{-1})

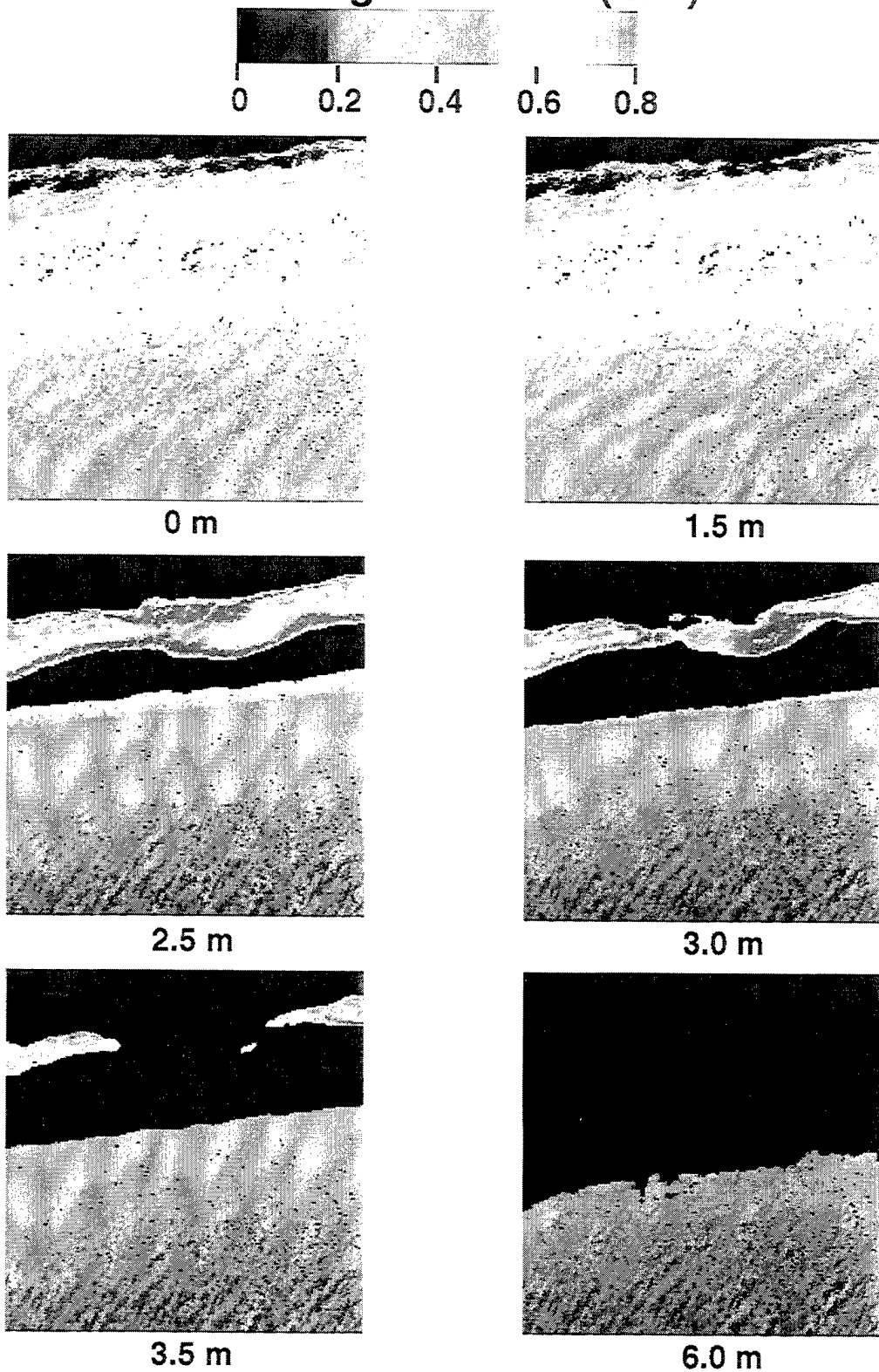
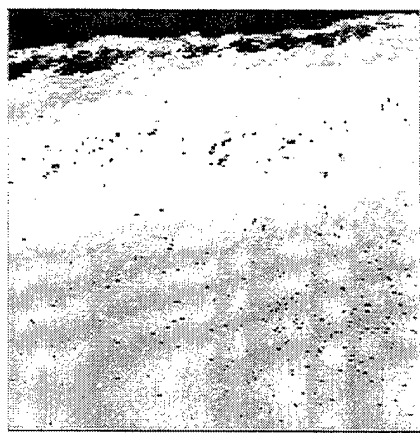


Fig. 4.

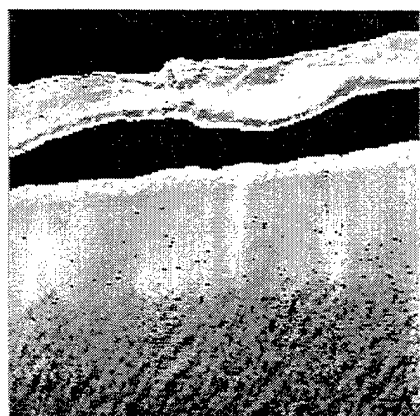
Scattering at 510 nm (m^{-1})



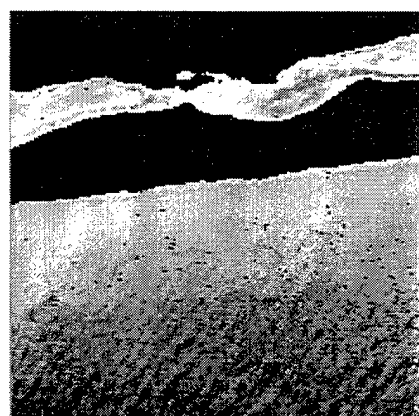
0 m



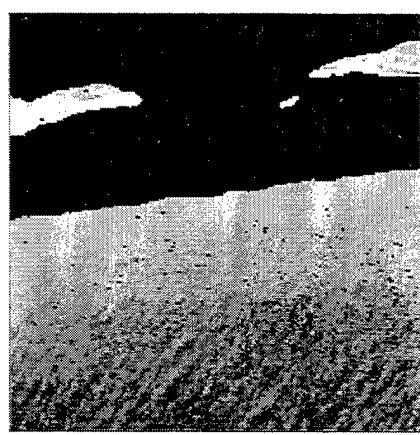
1.5 m



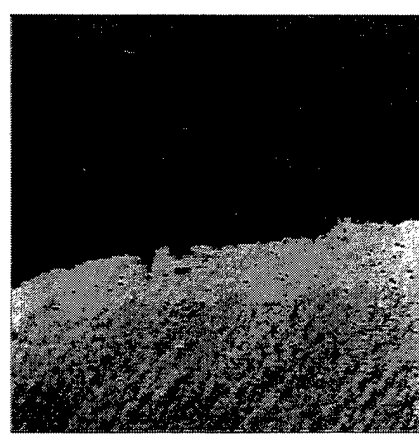
2.5 m



3.0 m



3.5 m



6.0 m

Fig. 42

Scattering at 555 nm (m^{-1})

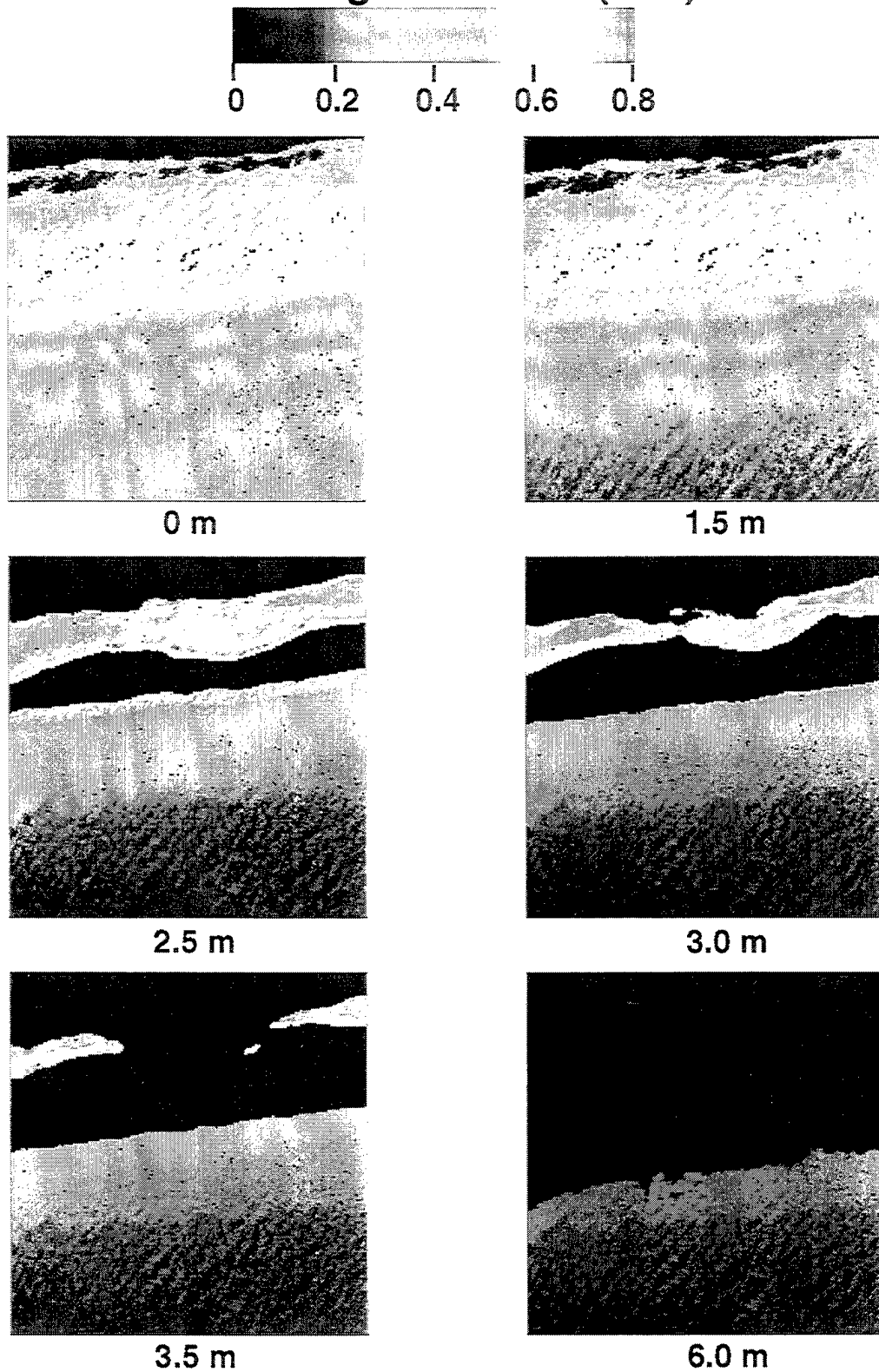


Fig. 43

Scattering at 670 nm (m^{-1})

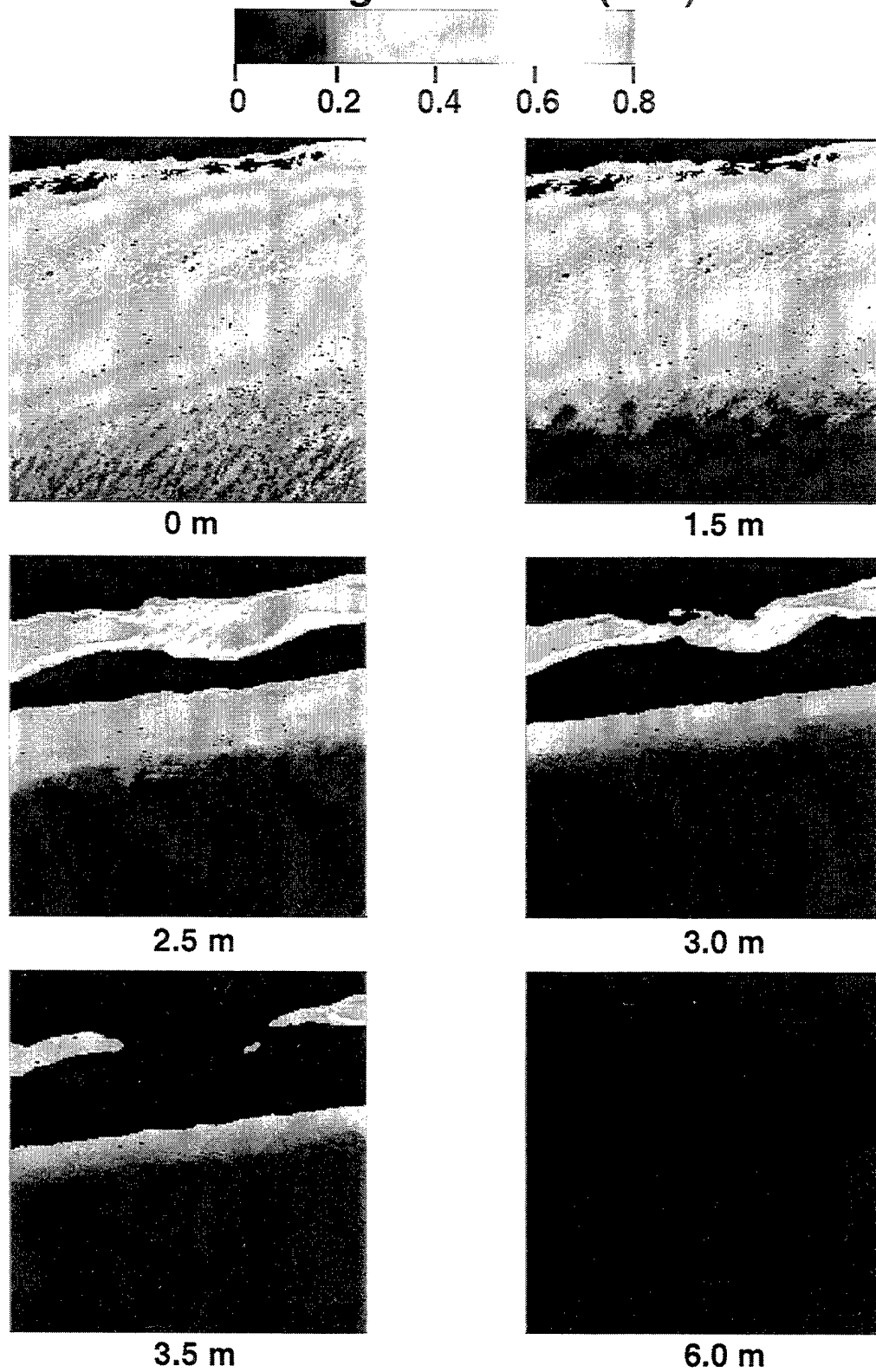


Fig. 44

Single Scattering Albedo at 412 nm

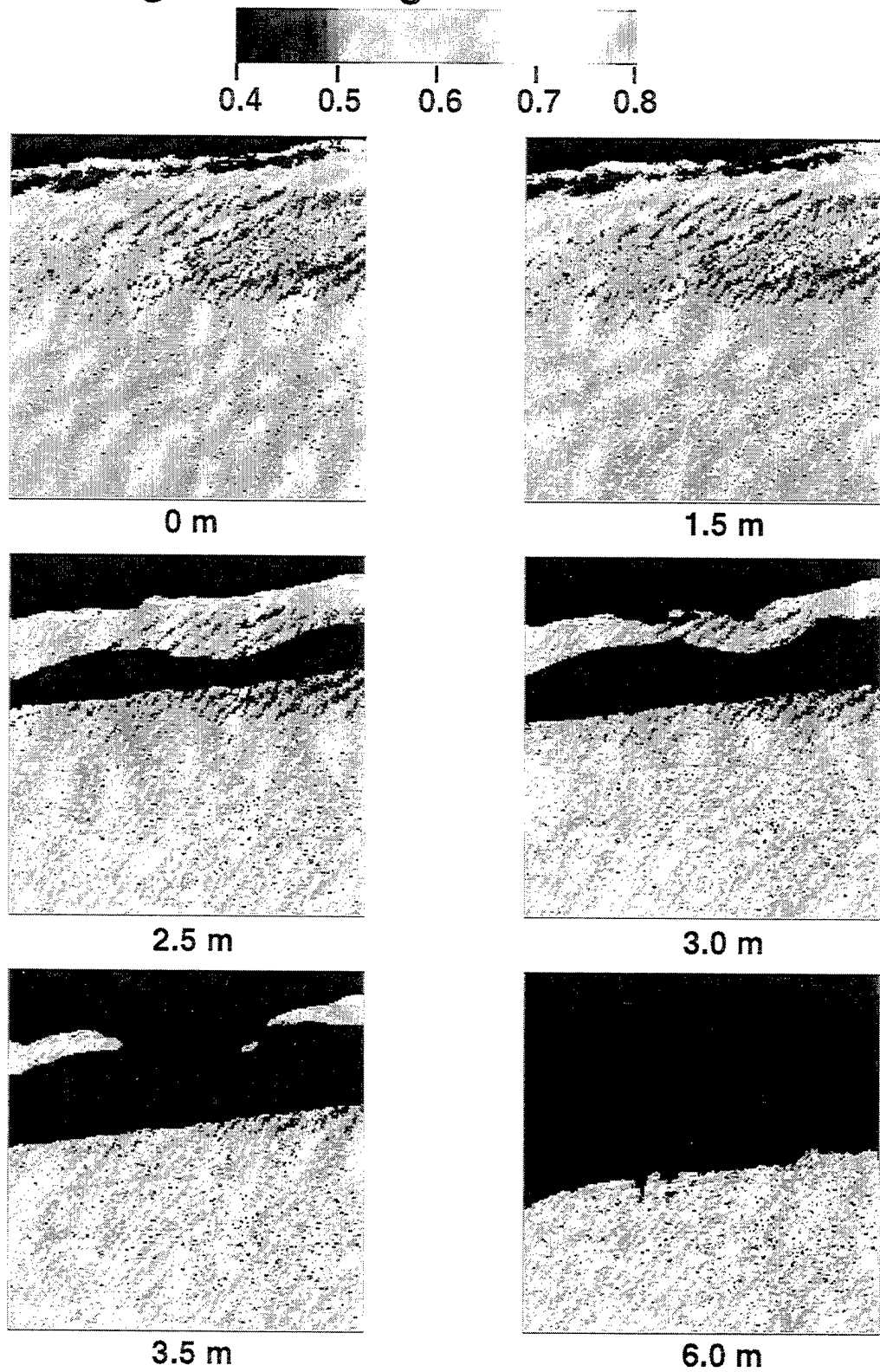


Fig. 45

Single Scattering Albedo at 443 nm

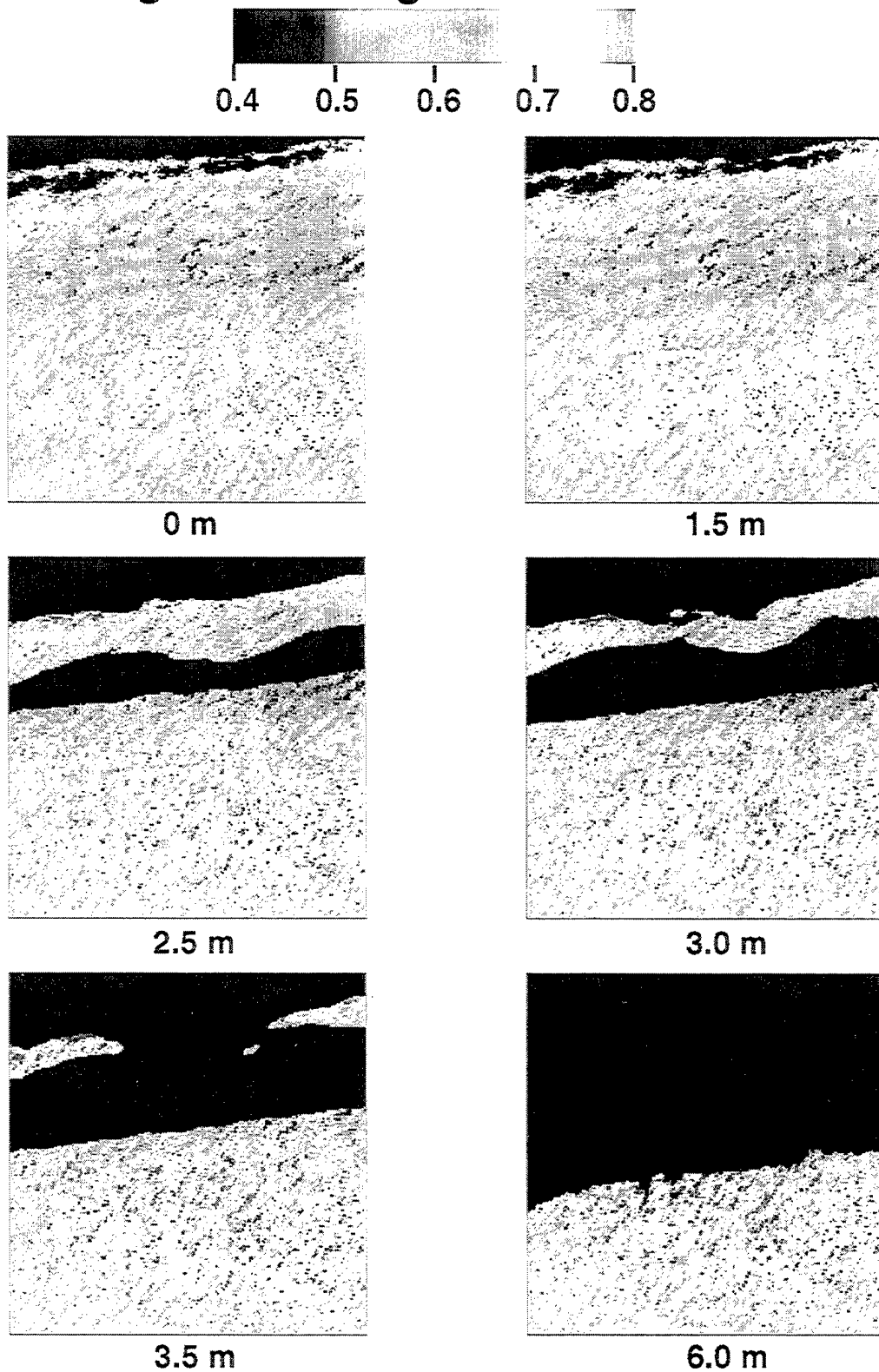


Fig. 46

Single Scattering Albedo at 490 nm

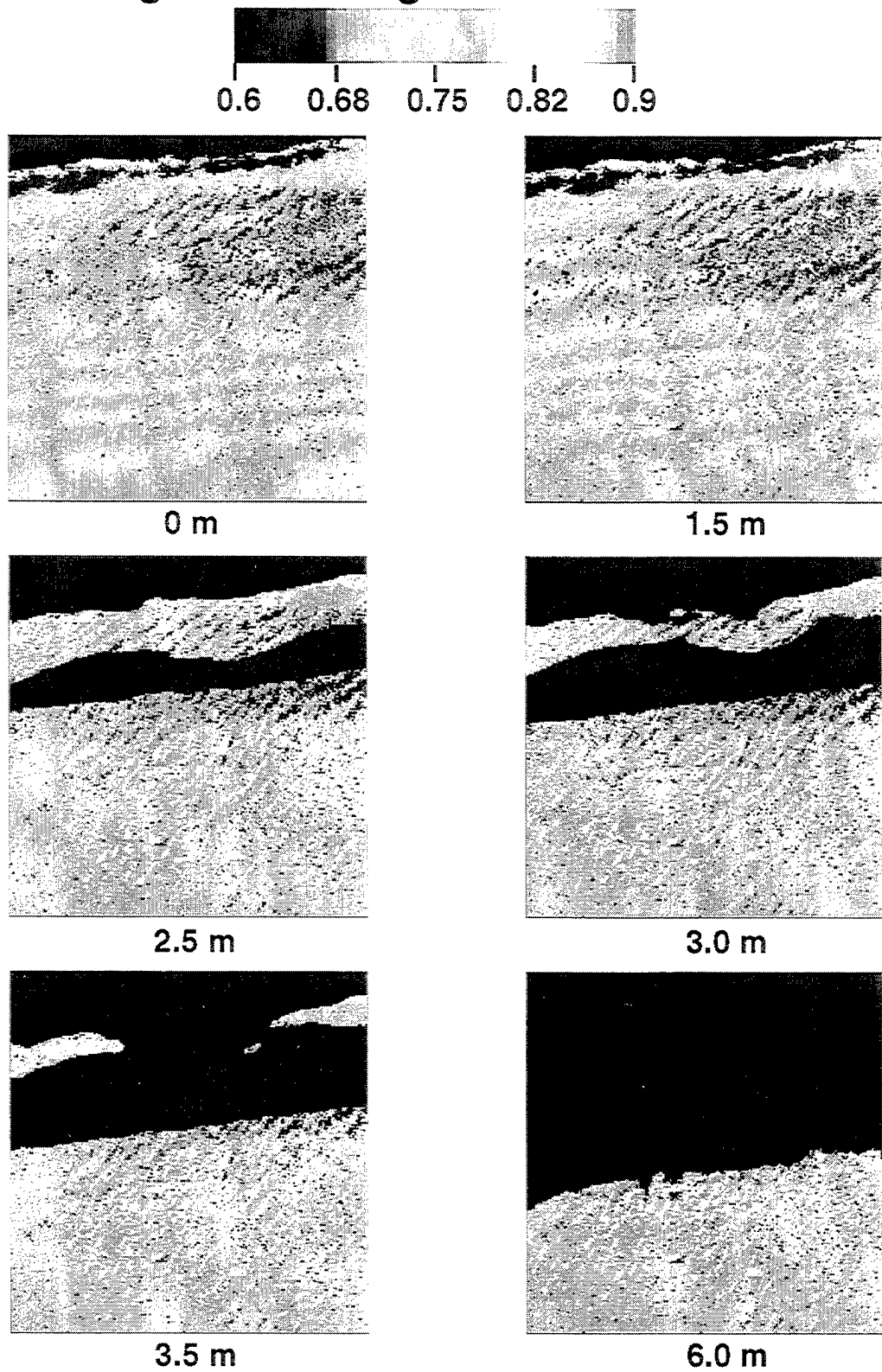


Fig. 47

Single Scattering Albedo at 510 nm

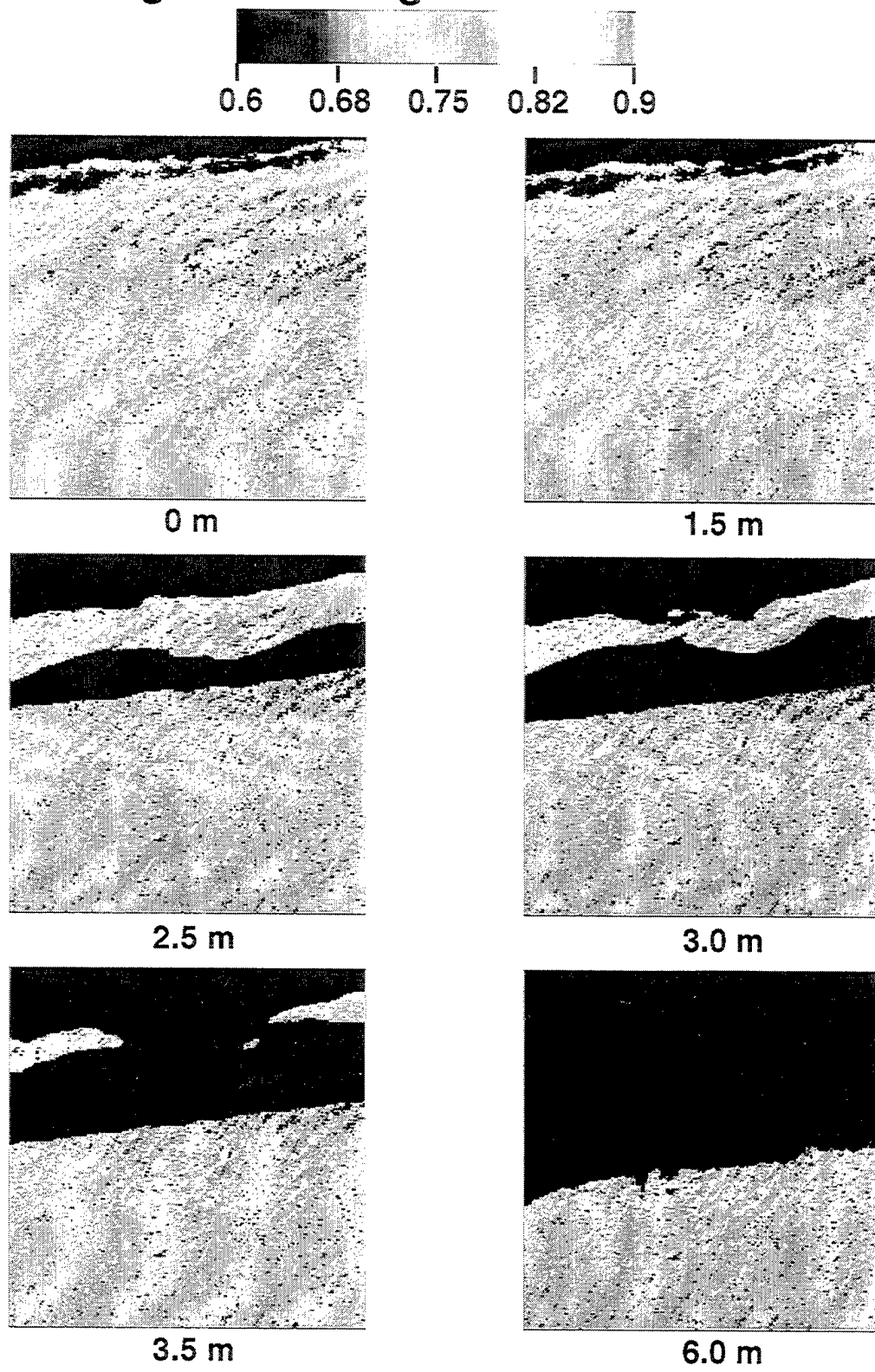


Fig. 48

Single Scattering Albedo at 555 nm

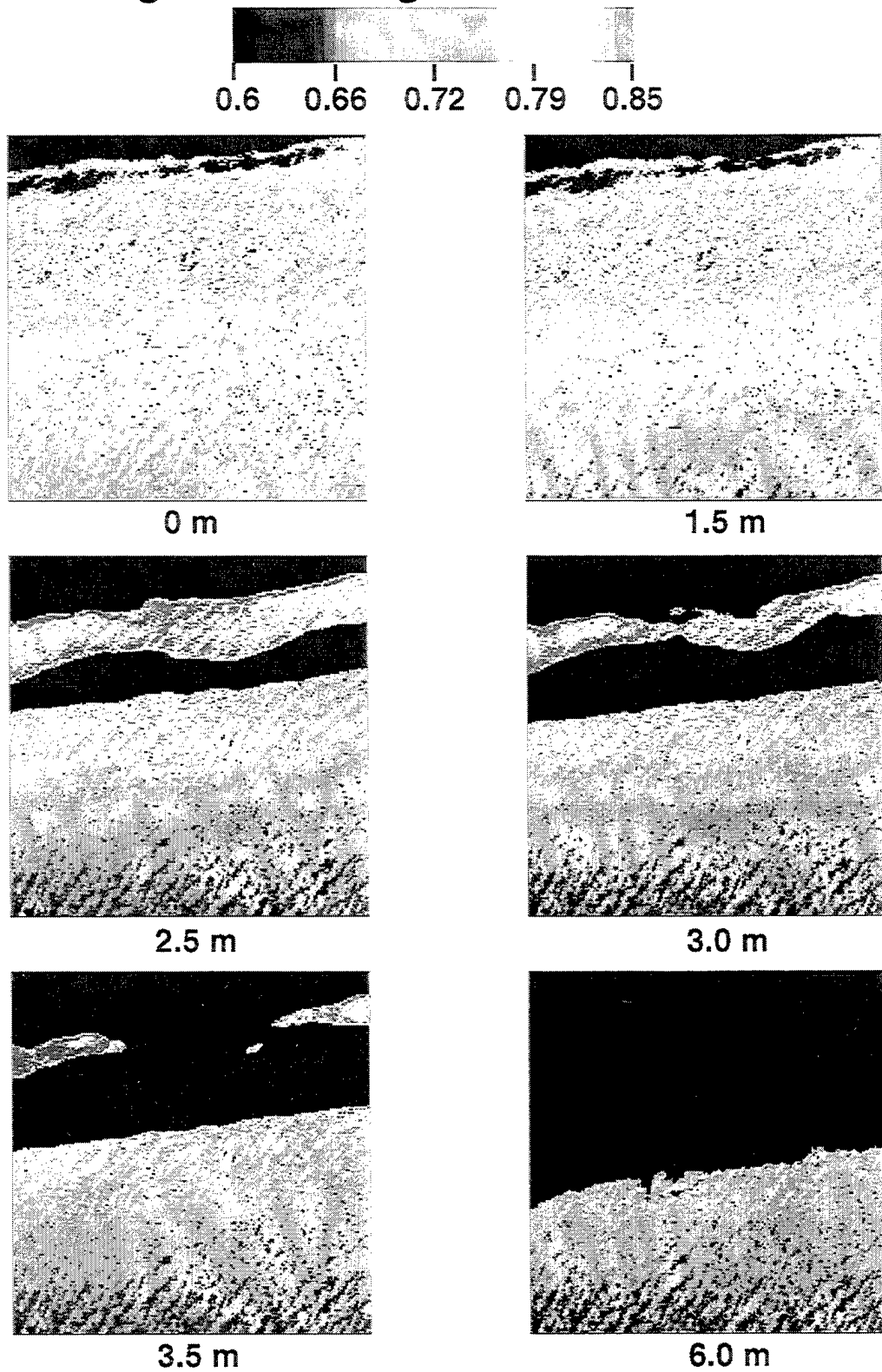


Fig. 49

Single Scattering Albedo at 670 nm

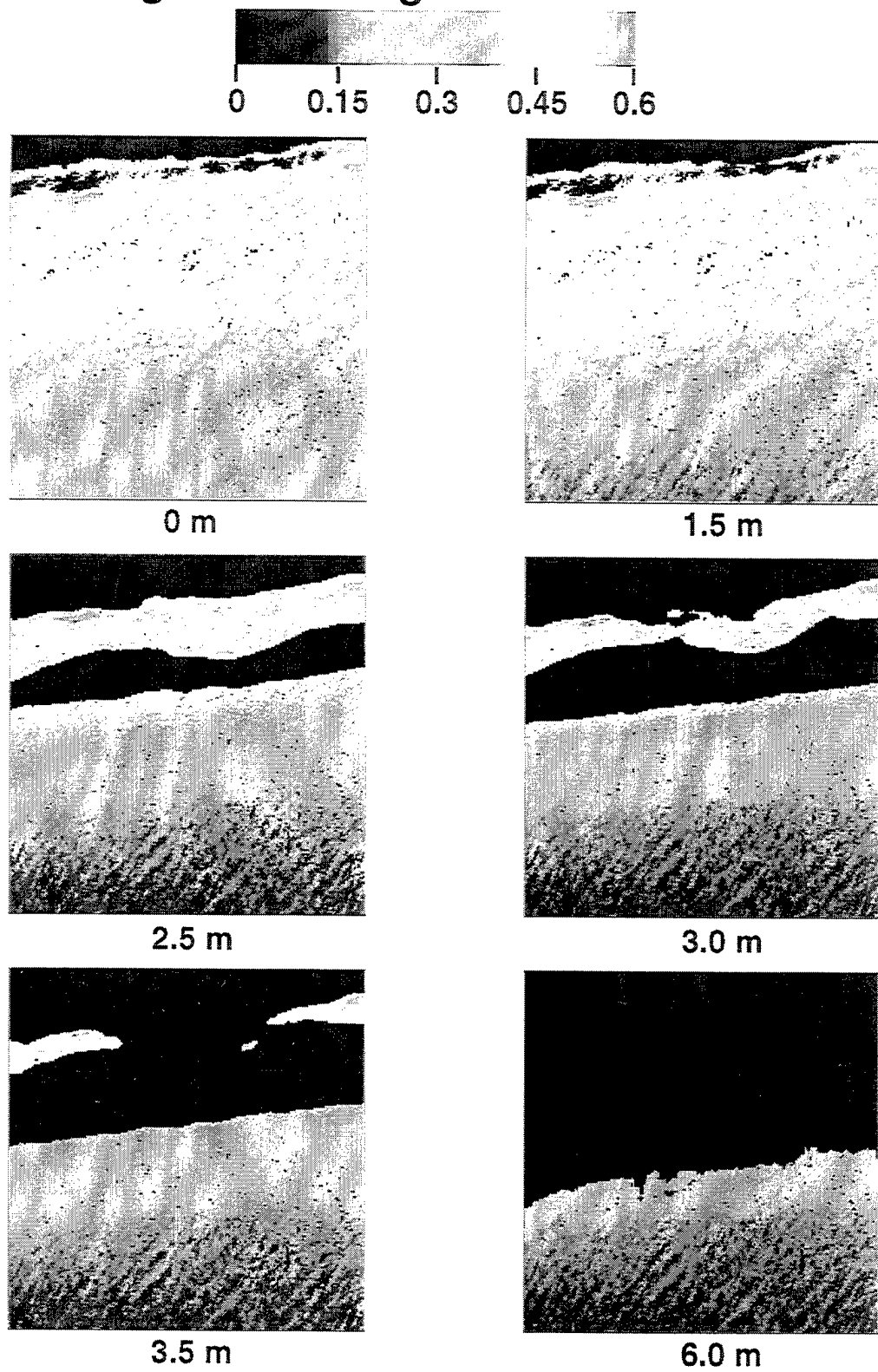
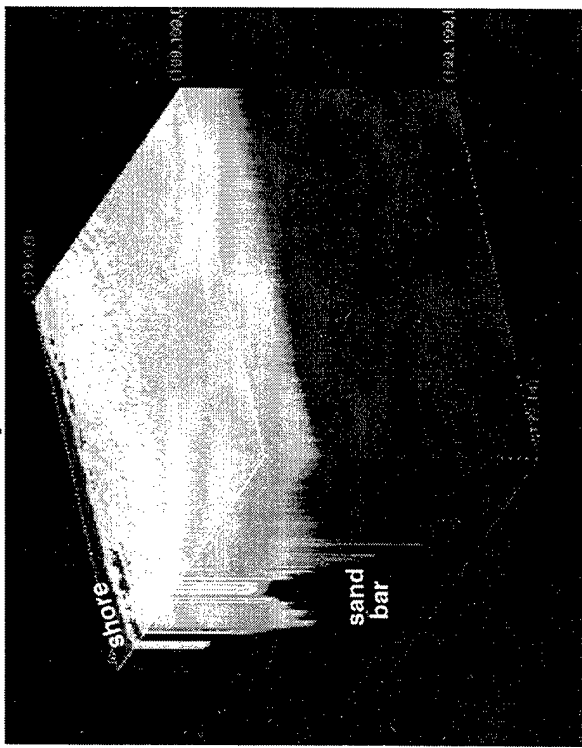
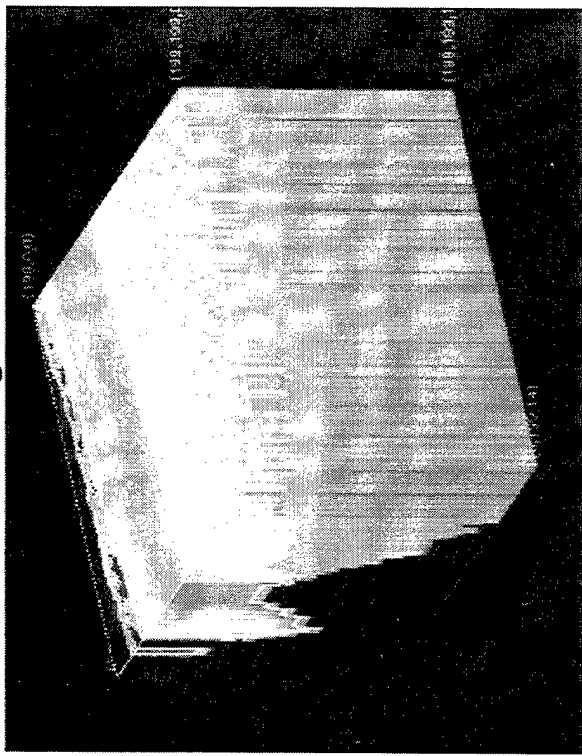


Fig. 50

Absorption at 412 nm



Scattering at 412 nm



Single Scattering Albedo at 412 nm

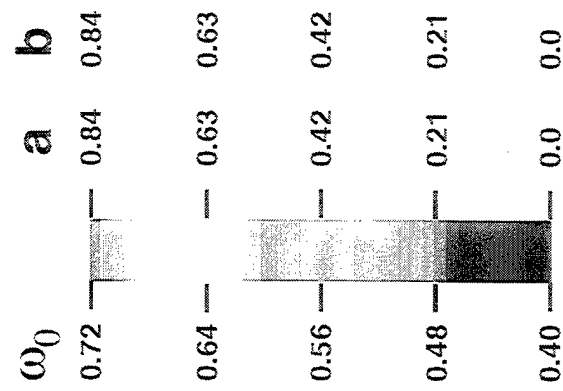
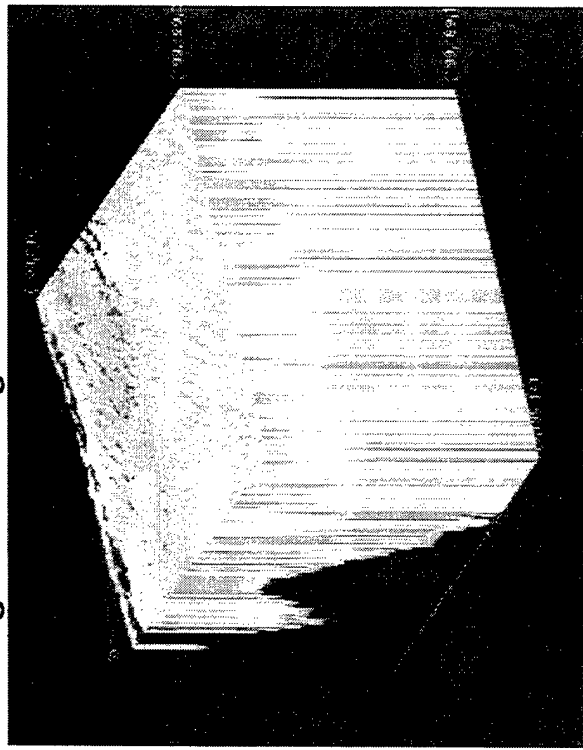
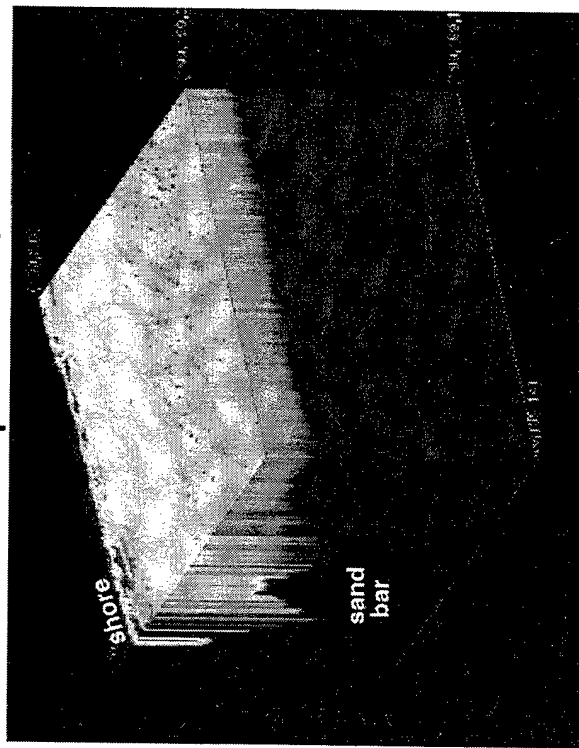
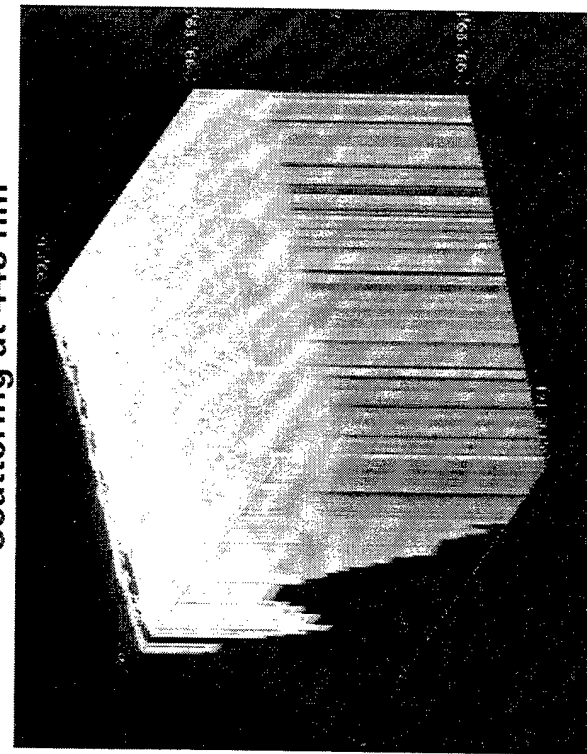


Fig. 51

Absorption at 443 nm



Scattering at 443 nm



Single Scattering Albedo at 443 nm

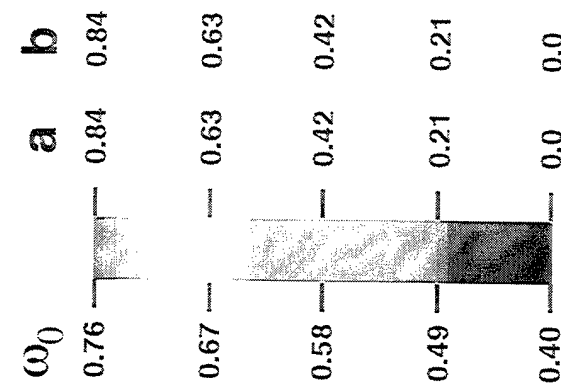
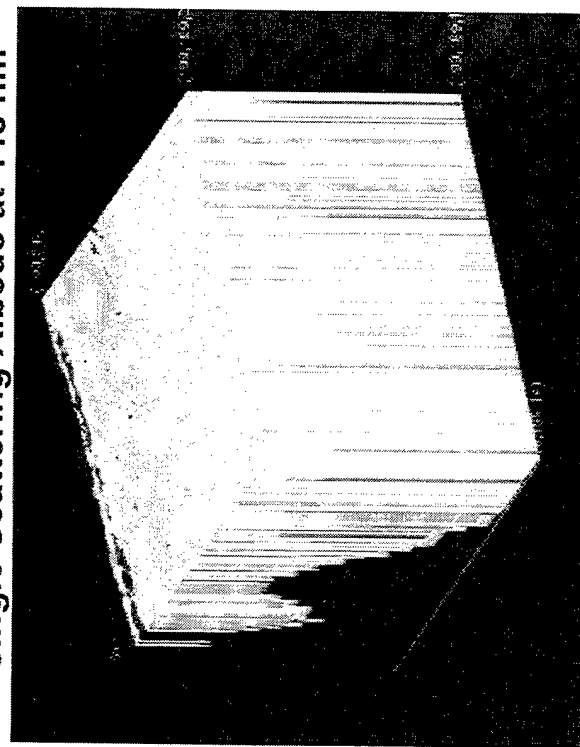
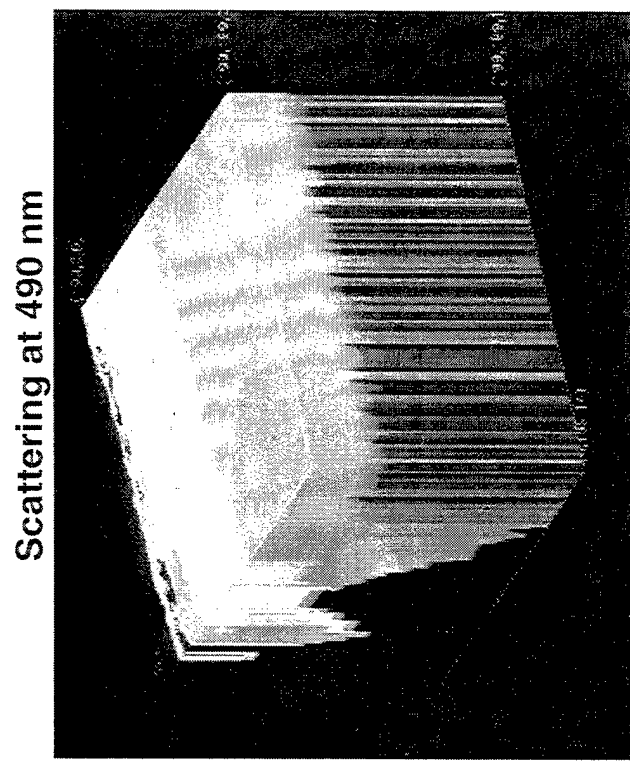
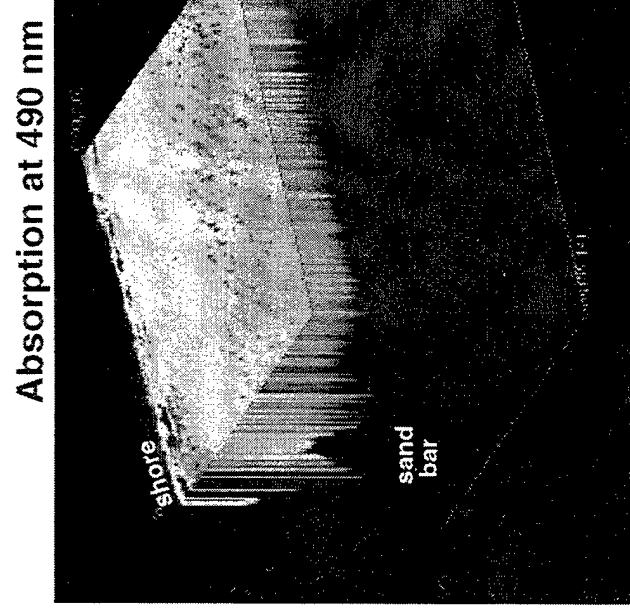


Fig. 52



Single Scattering Albedo at 490 nm

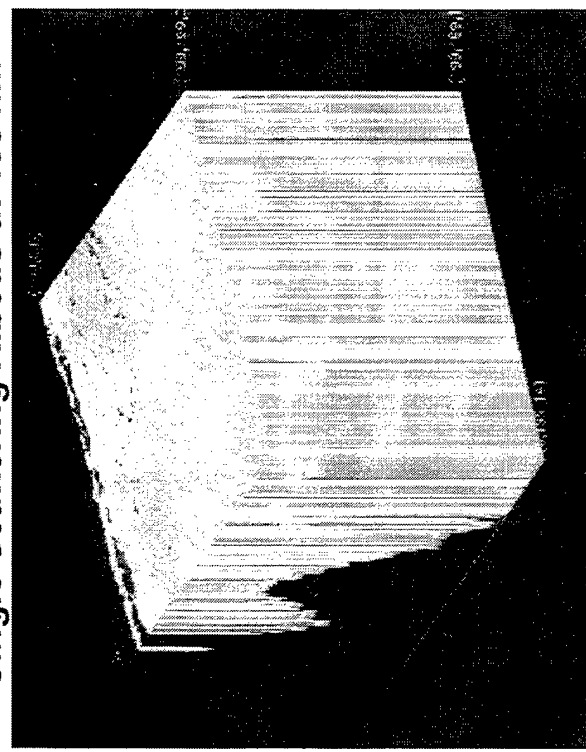
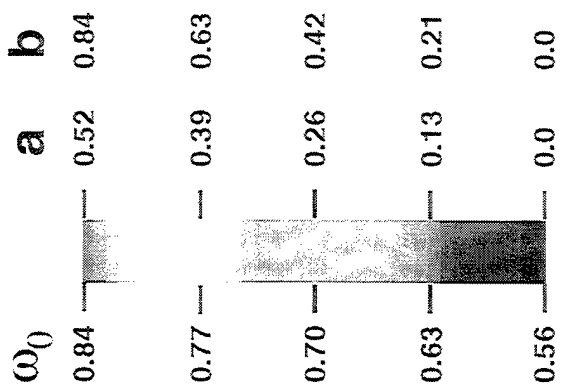
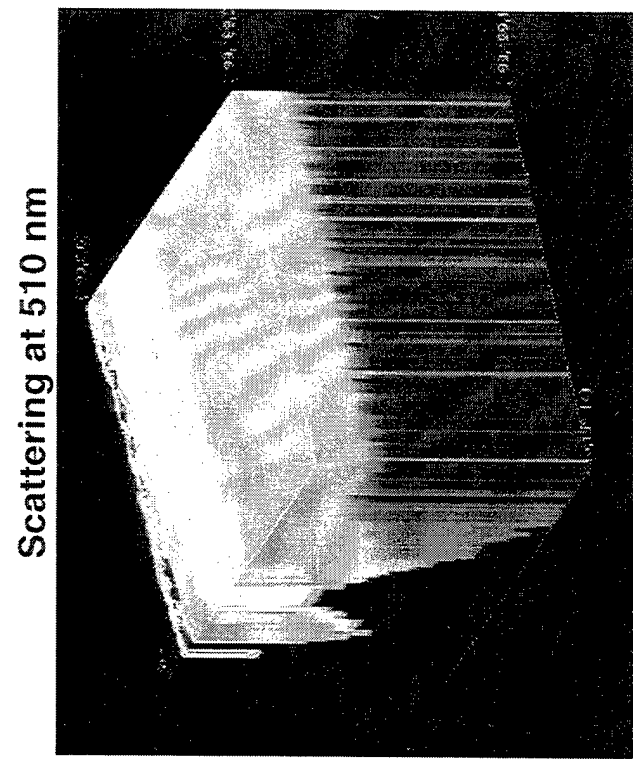
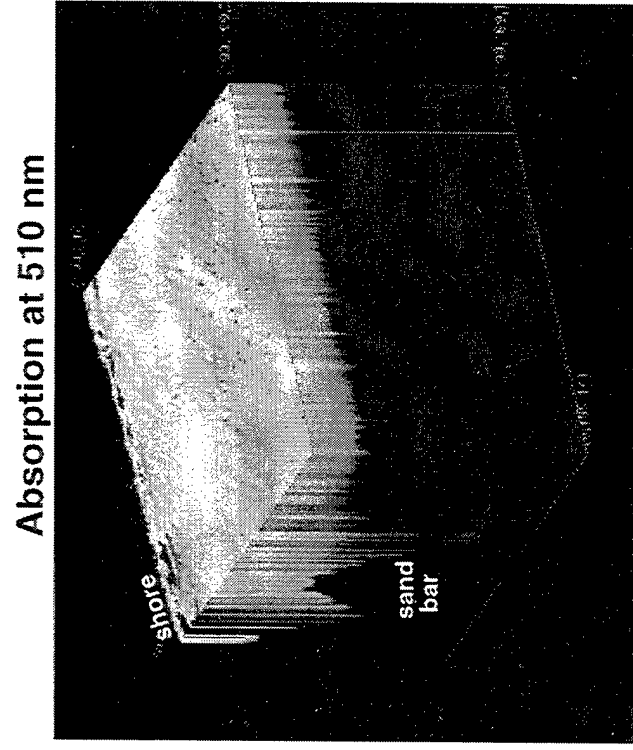


Fig. 53



Single Scattering Albedo at 510 nm

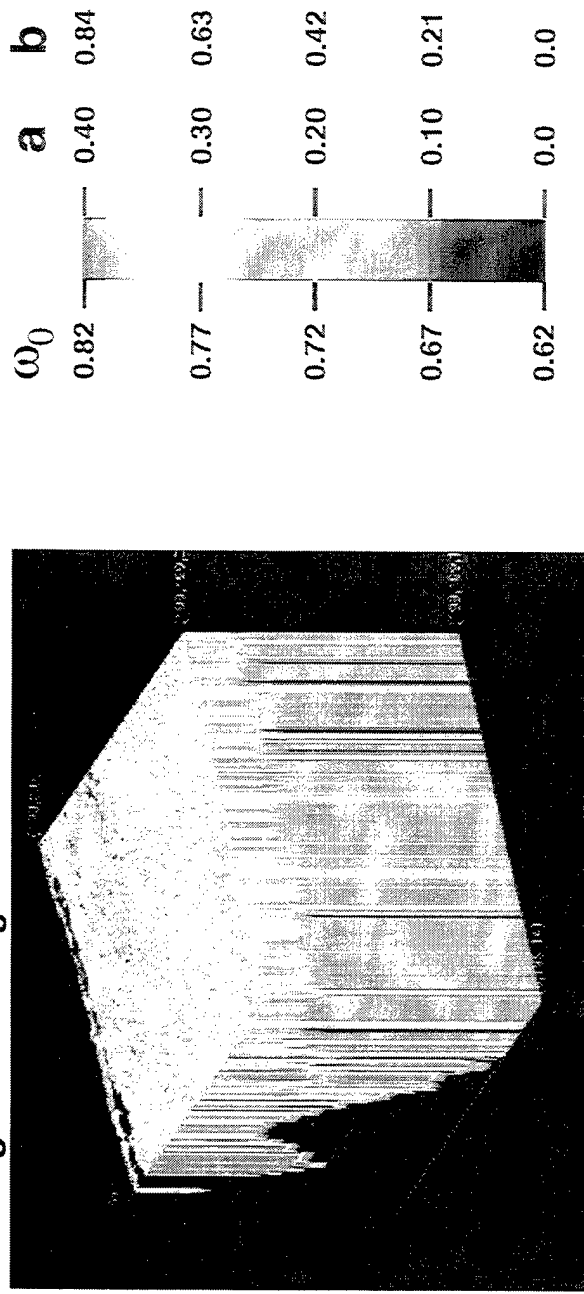


Fig. 54

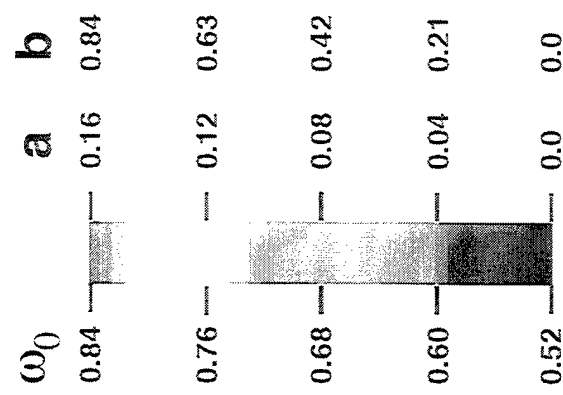
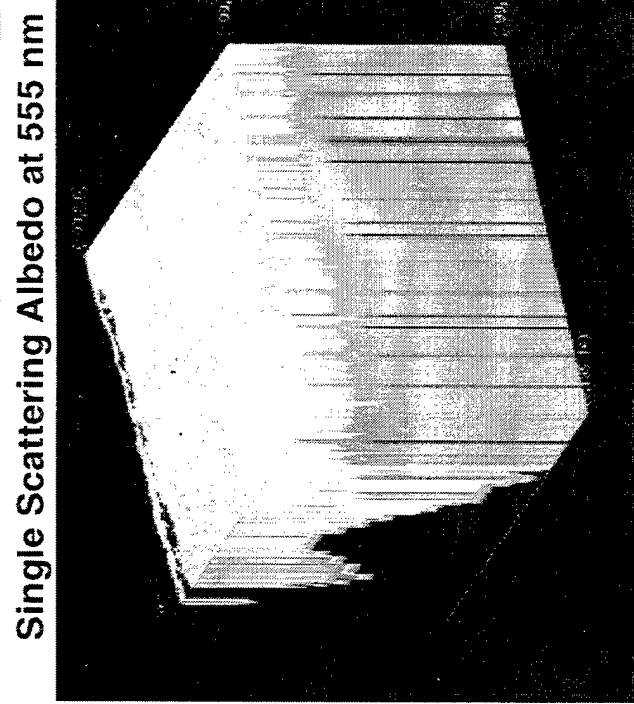
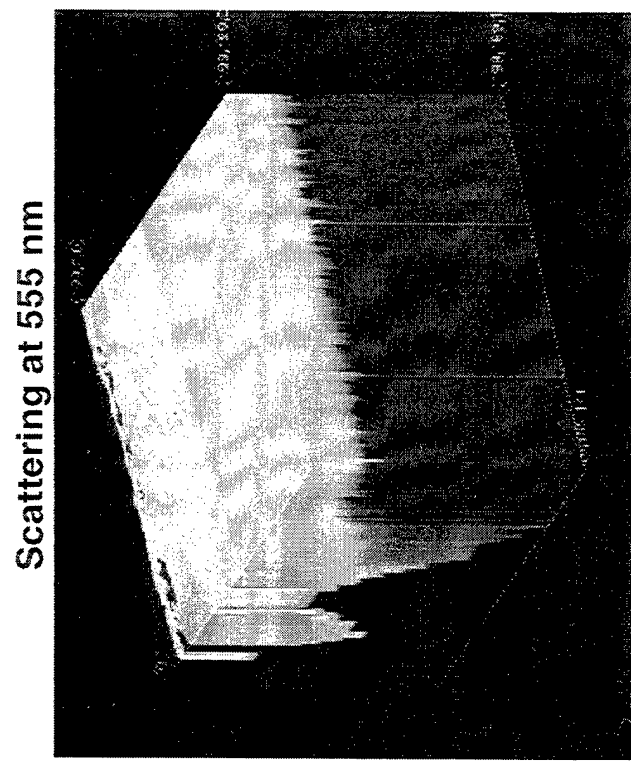
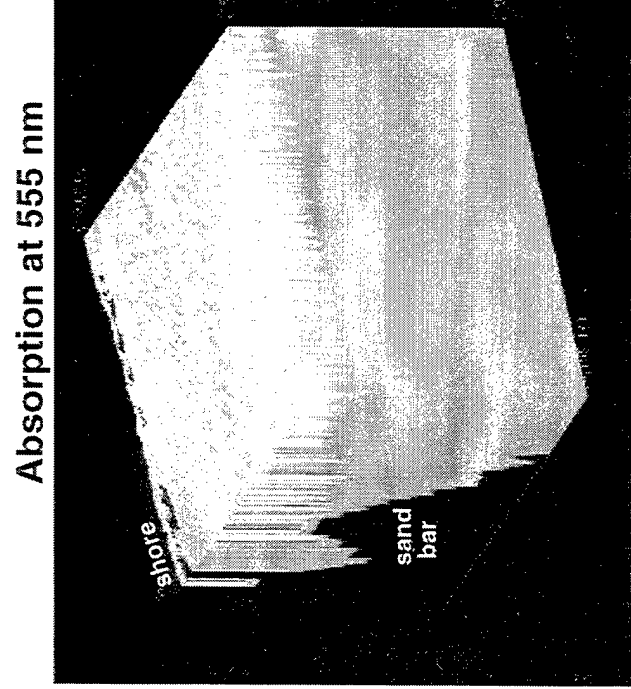
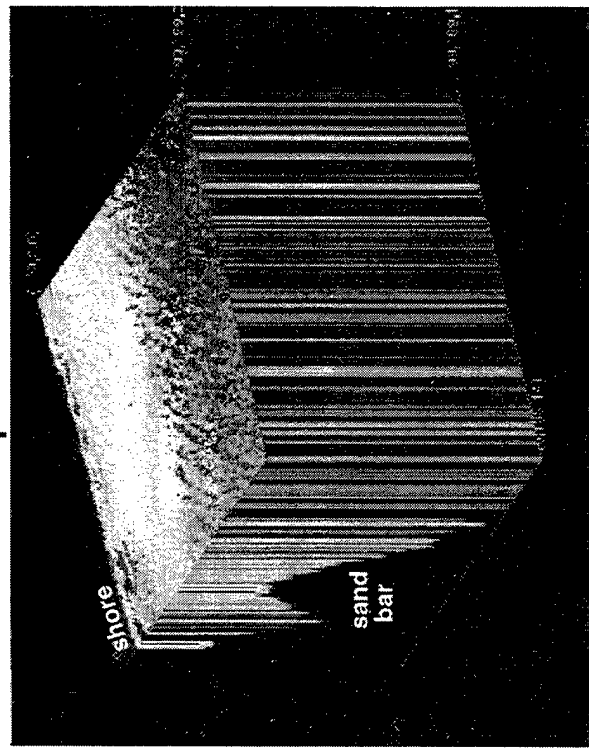
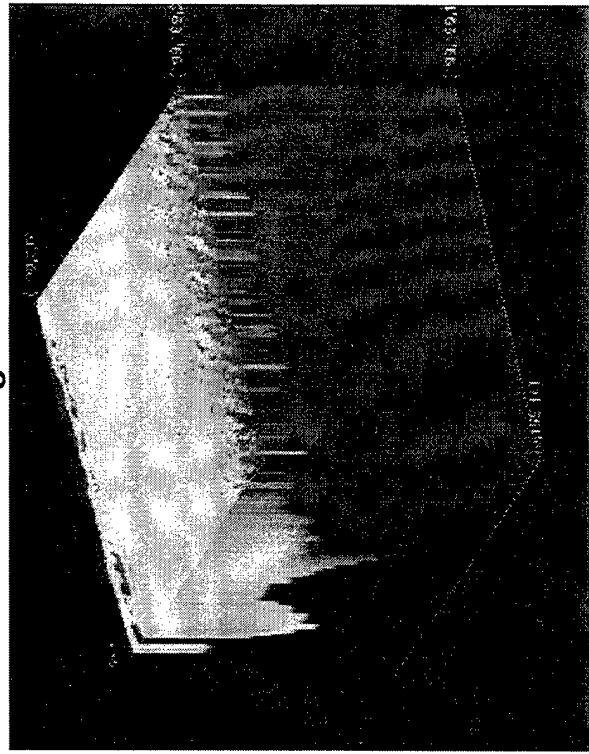


Fig. 55

Absorption at 670 nm



Scattering at 670 nm



Single Scattering Albedo at 670 nm

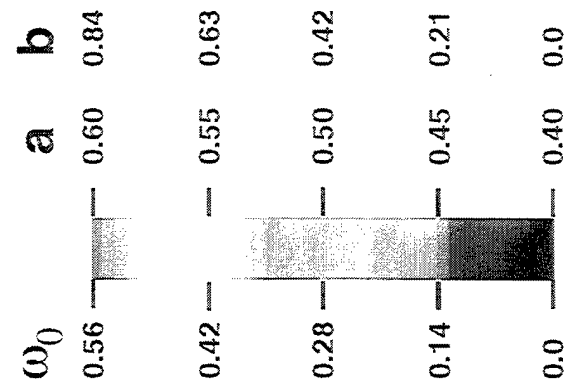
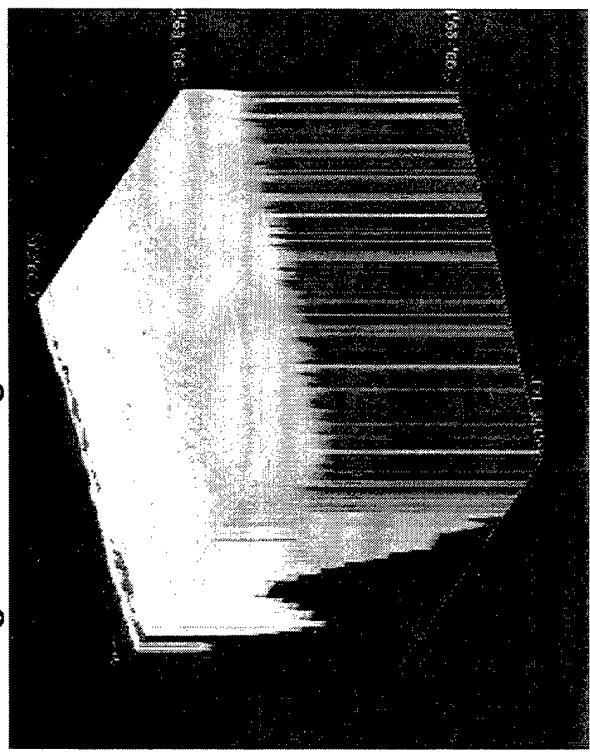


Fig. 56